

pubs.acs.org/ac Review

# Sensors Based Upon Nanowires, Nanotubes, and Nanoribbons: 2016–2020

Joshua M. Ziegler, Ilektra Andoni, Eric J. Choi, Lu Fang, Heriberto Flores-Zuleta, Nicholas J. Humphrey, Dong-Hwan Kim, Jihoon Shin, Hyunho Youn, and Reginald M. Penner\*



Cite This: Anal. Chem. 2021, 93, 124-166



ACCESS	Metrics & More		Article Recommendations	
CONTENTS			Semiconductor Nanowires	139
CADDONI NIANIOTI IDEC	AND LAVEDED MATERIALS	125	Introduction and Background	139
	S AND LAYERED MATERIALS	125	Synthesis and Sensor Fabrication	139
Introduction and E		125	Surface Modification of the Nanowire	140
Carbon Nanotuk		125	Transduction Mechanisms	141
Layered Materia		125	FETs	141
	abrication of Sensors Based		Electrochemical	141
	ayered Material NRs	127	Chemiresistors	141
Synthetic Metho		127	Recent Research	141
	INTs into Sensors	127	FET Biosensors	141
Synthesis of Gra		127	FET Chemical Sensors	143
	S <sub>2</sub> Nanowires/Ribbons	128	pH Sensing	144
•	lack Phosphorus Nanowires/		Chemiresistors	144
Ribbons		128	Electrochemical	146
Transduction Mech	hanisms in CNTs and Layered		Metal Oxides	146
Material NRs		128	Introduction and Background	146
Chemiresistive		128	Synthesis and Fabrication Methods	146
Field-Effect Tran	ısistors (FETs)	128	Hydrothermal and Solvothermal Methods	146
Amperometric		128	Electrochemical Methods	140
Recent Research		129		147
CNTs		129	Chemical Vapor Deposition	147
Layered Materia	ıls	131	Other MO <sub>x</sub> NW Syntheses Transduction in Metal Oxide NWs	148
Opportunities and		132	Chemiresistive	148
CNTs for Practic	_	132		
Layered Materia	ils	132	Electrochemical	148
Metal Nanowires		132	Field-Effect Transistors (FETs)	149
Introduction and E	3ackground	132	Recent Research	149
Synthesis and Fab		132	Chemiresistive	149
Template Synth		132	Electrochemical	153
	Solvothermal, and Vapor-		FETs	154
Phase Methods	Joil Carlettian, and Tapan	133	Outlook on Metal Oxide NW Sensors	156
	Patterned NW Electrodepo-	133	Conducting Polymer NWs and NFs	156
sition (LPNE)	Tutterned Hir Electioneps	133	Synthesis of 1D Structures with Conductin	
	Lithography (EBL) and Nano-	133	Polymers	156
imprint Lithogra		133	Electrochemical Methods	156
	hanisms in Metal Nanowires	133	Soft Lithography	156
Chemiresistors	idilisilis ili ivictai Nalioviics	133	Direct Writing Techniques	157
Thermochemica	d	134		
Optical	1	134		
Electrochemical		134	Special Issue: Fundamental and Applied Reviews in	analytical.
			Analytical Chemistry 2021	Energy y
Piezoresistive/Pi		135		2021
• •	Transduction Schemes	135	Published: November 26, 2020	From which and Applied Remove in Charleton Charleton
Recent Research		135		
Hydrogen Senso	urs	135	·	<b>♦50000</b>



Biosensors

136

Mechanisms of Transduction in CP NWs and NFs	157
Chemiresistors	157
OFETs and FET-Based Sensors	157
Electrochemical Methods	157
Recent Research	158
Gas Sensing	158
Biological Sensing	160
Concluding Remarks	160
Author Information	160
Corresponding Author	160
Authors	160
Notes	161
Biographies	161
Acknowledgments	161
References	161

A n emerging subfield of chemical and bioanalytical analysis involving the development of sensors based upon one-dimensional (1D) conductors was supercharged in 2000 by Dai and co-workers<sup>1</sup> who pioneered the use of carbon nanotubes (CNTs). New methods for preparing nanowires (NWs) of silicon and palladium, discovered in 2000, debuted in sensors just one year later, in 2001.<sup>2,3</sup> Nanoribbons (NRs), in contrast, were not discovered and investigated in sensors until relatively recently.<sup>4</sup>

Prior to 2000, the area of 1D sensing depended mainly on conductors patterned onto substrates using electron beam lithography, focused ion beam deposition, and other methods. In this period, NW fabrication relied on expensive tools that have low throughput. Access to these tools was also limited. In the period since 1992, publications focusing on the development of sensors based upon these 1D materials have grown at an average rate of  $\approx 25\%/\text{year}$  to more than 25,000 citations/year (Figure 1). An inflection in this graph at 2000 marks the

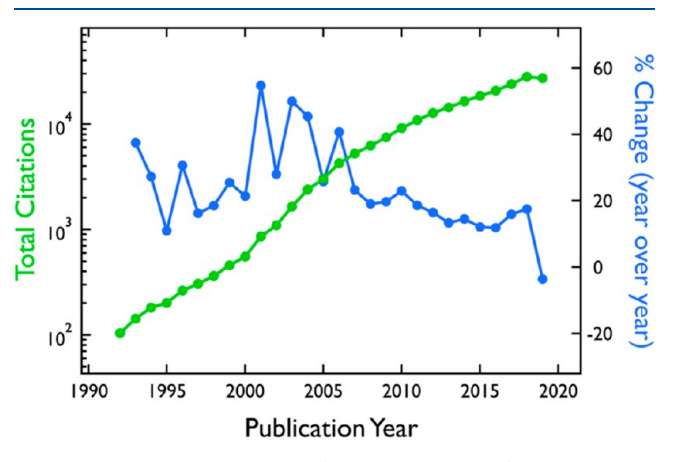


**Figure 1.** Total annual citations (green, note log axis) and change in total citations (blue) from 1992 to 2020 based upon a Google Scholar search on "sensor and nanotube or NW or nanoribbon" (Sept. 3, 2020).

introduction of CNTs and NWs prepared by high throughput gas and solution-phase processes. The trajectory of this plot to the present day provides a clear indication that scientists continue to find innovative applications in chemical sensing and biosensing for these systems.

In this Review, we focus attention on the developments in this field over the past five years, beginning in 2016. Even in this brief five-year period, more than 20,000 articles have appeared on this subject, but this Review must be limited to just 250 references. Considerable effort has been devoted to the identification of the most impactful science in this area; however, we have surely missed many excellent contributions, and we apologize to these authors for omitting their work.

The 1D materials that are foundational for this literature have not changed substantially over this period, consisting of semiconducting NWs, carbon single-walled nanotubes (SWNTs), metal NWs, and nanofibers (NFs) composed of conductive polymers and metal oxides. An exception are NRs derived from 2D materials, which are a new building block for sensors, but efforts in this direction have been impeded by the absence of robust, high throughput methods for synthesizing 1D NRs from 2D nanosheets of materials such as  $MoS_2$  and MXenes.  $^{5-7}$ 

While the basic 1D building blocks are unchanged, innovation has come in the form of new techniques for modifying these materials. This has resulted in the emergence of hybrid systems, particularly hierarchical materials in which materials are appended to carbon nanotubes or silicon NWs, for example, with the goal of increasing sensitivity and selectivity. Electrospinning coupled with thermal processing methods has emerged as a versatile and high throughput synthesis tool that provides the means for preparing metal oxide and porous carbon nanotubes with complex multilayered architectures that can also be decorated with a variety of catalyst particles to tune selectivity. The application of a diversity of 1D materials derived from electrospun precursors for gas sensing, in particular, is one of the most prominent new trends during this review period.

This Review is organized according to the composition of the 1D transducers: carbon nanotubes, MoS<sub>2</sub> nanoribbons, etc. The nanoscopic sensor elements that form the basis of the devices reviewed in this article are not, with a few exceptions, commercially available. Processes for preparing these nanomaterials continue to be refined, and new nanomaterials are continuously being developed. A section title, Synthesis and Sensor Fabrication will summarize notable developments in the synthesis and fabrication methods employed for each type of material. Transduction Mechanisms also vary from material to material. We provide an overview of the physics and chemistry exploited for performing quantitative measurements of concentration; all with an emphasis on advances over the past five years. Finally, sections titled "Recent Research" provide snapshots of some of the most prominent discoveries and studies during this time frame.

## CARBON NANOTUBES AND LAYERED MATERIALS

Introduction and Background. Carbon Nanotubes (CNTs). Carbon nanotubes (CNTs) have been extensively studied in biosensors and gas sensors. Consequently, in the last two decades, a huge number of CNT-based bio/chemical sensors have been developed, particularly with semiconducting CNTs. Among those developments, low-dimensional structures like NWs or NRs offer an excellent surface area-to-volume ratio, which efficiently provides a reaction area for target analytes (Table 1). Although the exploration of CNT-based bio/chemical sensor is nothing new, due to the aforementioned characteristics, it is still a fascinating interfacial material between a target analyte and an electrode.

Layered Materials. Graphene, 9,10 layered transition metal dichalcogenides, 11 and black phosphorus 12,13 belong to a

Table 1. CNT and Layered NW/NR Sensors<sup>a</sup>

sensor	synthetic method	mechanism	category	analyte	LOD and Range	$ au_{ m res}/ au_{ m rec}$	ref
BP	AAO template	CR	gas	NO <sub>2</sub>	10-400 ppm	~10 s/~6 s @ 10 ppm	40
graphene NRs	CNT unzipping	CR	gas	$NO_2$	125 ppb, 0.125-5 ppm	~6 s @ 0.125 ppm	41
graphene NRs	bottom-up chemical synthesis	CR	gas	EtOH	50-500 ppm	~240 s @ 500 ppm	38
graphene NRs	bottom-up chemical synthesis	CR	gas	MeOH	50-500 ppm	~900 s @ 500 ppm	38
graphene NRs	CNT unzipping	CR	gas	$NO_2$	0.125 ppm, 0.125-5 ppm	244 s/756 s	36
$MoS_2$	CVD	CR	gas	NO <sub>2</sub>	4.6 ppb, 1–5 ppm	16 s/172 s @ 5 ppm	5
CNT	OTS masking	FET	bio	AQP4	1 ng/L, 1-10 <sup>6</sup> ng/L	$\sim$ 30 s @ 1 $\mu$ g/L	19
CNT	DEP	AM	bio	streptavidin	100 aM, 100-10 <sup>6</sup> aM	N/A	21
CNT	DEP	AM	bio	HER2 antibody	10 fM, 10–10 <sup>5</sup> fM	N/A	21
CNT	direct contact printing	CR	bio	H5N1 DNA sequence	SWCNT: 2 pM, 2-200 pM; MWCNT: 20 pM, 20-2000 pM	N/A	22
CNT	drop-coat (paper filter)	CR	bio	PSA	1.18 ng/mL, 0-1000 ng/mL	N/A	50
CNT	DEP	FET	bio	cortisol	50 nM, 50-1000 nM	~100 s @ 1 µM	23
CNT	DEP	FET	bio	NPY	500 pM, 500–10 <sup>6</sup> pM	~30 s @ 50 nM	23
CNT	DEP	FET	bio	DHEAS	10 nM, 10-1000 nM	~100 s @ 1 µM	23
CNT	OTS masking	FET	bio	Aspergillus niger	N/A	N/A	20
CNT	OTS masking	FET	bio	Aspergillus versicolor	N/A	N/A	20
CNT	OTS masking	FET	bio	Saccharomyces cerevisiae	N/A	N/A	20
CNT	drop-coat	CR	bio	DNA	10 aM, 10–10 <sup>6</sup> aM	N/A	47
CNT	immersed in the CNT solution	FET	bio	DNA	60 aM, 100–1000 aM	~15 s @ 800 aM	25
CNT	immersed in the CNT solution	FET	bio	microvesicle	6 particles/mL, $6-6 \times 10^6$ particles/mL	N/A	25
CNT	catalytic CVD	FET	gas	N <sub>2</sub> <sup>+</sup> ion	single ion	200 ms	34
CNT	drop-coat (paper filter)	AM	gas	НСНО	0.016 ppm, 0.05-6.7 ppm	>1000 s/>1000 s	51
CNT	DEP	CR	gas	$H_2$	10 ppm, 10 ppm - 4%	62 s/72 s @ 1000 ppm	32
CNT	DEP	CR	gas	$NO_2$	0.5-20 ppm	N/A	42
CNT	immersed in the CNT solution	CR	gas	$H_2$	0.89 ppm	7 s/89 s @ 311 ppm	45
CNT	drop-coat	CR	gas	$NH_3$	100 ppb, 1.5-20 ppm	N/A	44
CNT	drop-coat	CR	gas	N-nitrosodialkylamine	1 ppb, 0-1000 ppb	N/A	245
CNT	spray deposition	CR	gas	$NH_3$	10 ppm, 10-100 ppm	N/A	246
CNT	spray deposition	CR	gas	CO <sub>2</sub>	600 ppm, 600-7000 ppm	N/A	246
CNT	Spray deposition	CR	gas	CO	3 ppm, 3-27 ppm	N/A	246
CNT	spray deposition	CR	gas	EtOH	17 ppm, 17-70 ppm	N/A	246
CNT	DEP	CR	gas	THC	0.163 ng, 0.0018 $-$ 0.8262 $\mu \mathrm{g}$	1800 s	49
CNT	drop-coat	CR	gas	NH <sub>3</sub>	2 ppm, 2-40 ppm	N/A	43
CNT	drop-coat	CR	gas	NO <sub>2</sub>	2 ppm, 2-40 ppm	N/A	43
CNT	catalytic CVD	CR	gas	toluene	50 ppm, 50-500 ppm	10 s/11 s @ 500 ppm	33
CNT	spin-coat	FET	bio	DNA (cDNA from T47D cancer cell)	880 ng/L, $50-5 \times 10^6$ pM	N/A	24

"Abbreviations: LOD = limit of detection, BP = black phosphorus, NRs = nanoribbons, CNT = carbon nanotubes, AAO = anodic aluminum oxide, HT = hydrothermal synthesis, CVD = chemical vapor deposition, OTS = octadecyltrichlorosilane, DEP = dielectrophoresis, CR = chemiresistive, AM = amperometric, FET = field-effect transistor, AQP4 = aquaporin-4, HER2 = human epidermal growth factor receptor 2, PSA = prostate-specific antigen, NPY = neuropeptide Y, DHEAS = dehydroepiandrosterone sulfate, HCHO = formaldehyde, THC = tetrahydrocannabinol, N/A = information not available, and  $\tau_{res}/\tau_{rec}$  = reported or estimated response time/recovery time.

family of 2D materials in which the atoms are arranged in a layered, sheet-like structure. Individual layers can be exfoliated from the bulk and typically show interesting electrical properties that depart significantly from that of the bulk material.  $^9$ 

Graphene, the most intensively studied 2D material, is semi-metallic with a high carrier mobility (up to 200 000 cm $^2$  V $^{-1}$  s $^{-1}$  for a single layer) and excellent mechanical strength,

attributes that make it a promising candidate for many applications. Bedge defects in graphene have higher chemical reactivity and can impart unique electronic/spintronic properties that are observable when graphene is formed into nanoribbons. Graphene NRs narrower than 10 nm are particularly of interest as quantum confinement of the electrons opens a band gap, increasing the potential

applications of graphene in electronics and chemiresistive sensing, 9,14,15

Nanoribbons derived from the layered transition metal dichalcogenides (TMDCs), particularly MoS<sub>2</sub>, are increasingly of interest for sensing. While graphene is a true semimetal with no band gap, MoS<sub>2</sub> can be an n- or p-type semiconductor depending on the preparation method, allowing for applications to gas sensing, energy storage, electronics, and optics. As in the case of graphene, single- or few-layered MoS<sub>2</sub> ribbons have enormous surface area/volume ratios that enable their use for sensitive sensing. 11

Interest in black phosphorus (BP), called phosphorene in its single-layered form, was revived by multiple electronic property studies in 2014. It is just the second elemental 2D material and has a bandgap of 0.30 eV, intermediate between graphene (0 eV) and the TMDCs (1.5–2.5 eV). Gas sensors based upon BP are predicted to have excellent sensitivity, exceeding that of either graphene or 2D MoS<sub>2</sub>, which can be further improved by increasing the surface-to-volume ratio with nanostructuring. <sup>13</sup>

Synthesis and Fabrication of Sensors Based Upon CNTs and Layered Material NRs. Synthetic Methods for CNTs. The synthesis of CNTs is often accomplished using one of three methods. (i) Arc-discharge: In this method, the plasma of an inert gas is generated to evaporate the carbon atoms. 16 Then, the ejected carbon atoms are deposited onto a negative electrode to form CNTs. This is the leading method to produce CNTs with high-quality structures. (ii) Laser ablation: In this method, an intense laser ablates a carbon target and CNTs are formed on a cold substrate.<sup>17</sup> (iii) Chemical vapor deposition (CVD): Unlike the two previous methods, which require very high temperatures to grow singlewall CNTs (SWCNTs) (1200 °C), SWCNTs can be formed at relatively low temperatures (850-1000 °C) using the CVD method. By flowing hydrocarbon gas (e.g., acetylene, ethylene, or methane) into a processing chamber in the presence of metallic catalysts, CNTs can be grown on the metallic catalysts. 18 However, relative to other methods, the CVD method produces CNTs with relatively high defect contents that can be the source of inconsistency in CNT-based applications. In CNT synthesis, scaling-up production and obtaining semiconducting CNTs with high purity are important topics relevant for practical devices.

Integration of CNTs into Sensors. For use in sensors, CNTs can be configured as a conductive channel by patterning electrodes onto individual CNTs using electron beam lithography (EBL) coupled with evaporation and metal lift-off, or direct focused ion beam (FIB) metal deposition. CNTs can also be manipulated onto prepatterned electrical contacts using electric fields as in dielectrophoresis (DEP), or they can be grown on prepatterned catalyst particles positioned to determine the orientation of the CNTs to facilitate the formation of electrical contacts.

A new approach is the "self-assembly" of CNT sensor structures in which affinities between functionalities distributed on the sensor surface and complementary functionalities on CNTs drive attachment. In one recent example, octadecyltrichlorosilane (OTS) protects silicon and limits CNT adsorption onto only the unmodified regions of the patterned substrate. <sup>19,20</sup> In a second example, the sensor fabrication process is simplified through directed deposition by modifying both the CNTs and the substrate surface with ss-DNA. <sup>23</sup>

The deposition of a network of CNTs with improved homogeneity has also been reported using a spin-coat and dipcoat method.<sup>24,25</sup> For instance, CNTs suspended in a solvent containing an organic dispersant form a homogeneous network by spin-coating, 24 but an excess of residual surfactant is associated with some degradation of sensor performance.<sup>26</sup> Alternatively, research from Gu et al demonstrated by using conjugated molecules in organic solvents instead of surfactants, it is possible to avoid this problem. They described a new linear homopolymer, poly[9-(1-octylonoyl)-9H-carbazole-2,7diyl] (PCz), that has selectivity for large-diameter semiconducting SWCNTs (s-SWCNT). From dispersions of CNTs with varying diameters in toluene, PCz selectively solubilizes CNTs based upon diameter and, therefore, its electronic properties. From these "sorted" solutions, extremely high quality thin film transistors (TFTs) can be prepared by dipcoating of the CNTs onto prefabricated electrodes on SiO<sub>2</sub>/ silicon. The resulting s-SWCNT channel TFTs produced high carrier mobilities of 28-67.5 cm<sup>2</sup> V<sup>-1</sup> s<sup>-1</sup> and on-off current ratios of  $10^5 - 10^6$ .

DEP is a well-defined method, both theoretically 28,29 and experimentally, 30,31 for the integration of CNTs into sensor architectures. DEP can enable spatially precise deposition and CNTs can be aligned along applied electric field lines. In previous studies of CNT-based bio/chemical sensors, DEP has been used for highly selective deposition and the dense formation of CNTs between electrodes. One such example is the report from Li et al.<sup>32</sup> In their work, the linear CNT bundles (CNT "ropes") were formed along a lithographically patterned electrode. These CNT ropes, decorated with palladium NPs, formed the basis for hydrogen gas sensors.<sup>3</sup> In 2018, Xu et al.<sup>23</sup> presented a sensor for multipurpose analysis fabricated using DEP. To use the sensors for the detection of multiple biomarkers, three identical CNTaptamer systems were immobilized on separate electrode pairs on the same substrate by inducing a more locally controlled electric field. The proposed multi-purpose sensor also can be regenerated by a simple wash in an 8 M urea solution due to the strong immobilization of the CNTs by DEP. Li et al.<sup>21</sup> described how the alignment of CNTs can be controlled by sequential application of DC and AC voltage. During the DC-DEP process, the CNTs aligned vertically along the DC field lines on top of the electrodes. Once AC voltage is applied, the CNTs rapidly aligned to the horizontal

The alignment of CNTs within sensors can be achieved by direct growth onto the sensor substrate. In the presence of metallic catalysts on the substrate, CNTs can grow with a predetermined orientation from the catalyst nanoparticles (NPs). For instance, to make vertically aligned  $H_2$  receptors, CNTs can be grown on a graphene substrate decorated with iron NPs, via CVD at 700  $^{\circ}\text{C}$  using  $C_2H_2$  as the carbon source.  $^{33}$  CVD can also be used in the horizontal growth of CNTs to bridge the electrodes on the sensor substrate. Suspended CNTs have been obtained using this approach with Fe–Mo catalyst islands.  $^{34}$ 

Synthesis of Graphene NRs. The fabrication of graphene NRs is usually accomplished by CNT unzipping, first demonstrated independently by the research groups of Hongjie Dai<sup>15</sup> and James Tour in 2009.<sup>35</sup> Dai and co-workers<sup>15</sup> showed that multi-walled CNTs (MWCNTs) can be immobilized in poly(methyl methacrylate) and unzipped physically by plasma etching the exposed CNT.<sup>15</sup> Tour and co-workers<sup>35</sup> exploited

the oxidation of alkenes by permanganate in sulfuric acid to produce "holes" in CNTs that act as the starting point for sequential unzipping.<sup>35</sup> More recently, it has been shown that MWCNTs can be unzipped in a two-step electrochemical—sonochemical method that preserves the crystallinity of the graphene unlike previous methods.<sup>36</sup>

Other common fabrication methods used for graphene NR sensors include bottom-up chemical synthesis and CVD. 9,37,38 Bottom-up chemical synthesis relies upon multistep organic syntheses that start with alkyne, alkene, or halogenated precursors that are assembled into a polymer that serves as the synthetic precursors to graphene nanoribbons. 9,37,38 CVD bottom-up synthesis relies on graphene formation induced by the thermal decomposition of the organic polymers. Ompared to top-down synthetic methods, bottom-up synthetic methods offer greater uniformity and control over the graphene NR edges.

Typically, graphene NRs are drop-cast or dried onto the sensing substrate. An emerging method of graphene NR sensor fabrication is through the use of interfacial self-assembly, which allows for a more organized graphene NR sensing film. <sup>36,38</sup> Graphene NR dispersions are mixed with water, and hydrophobic graphene NRs assemble laterally at the liquid—air interface to form graphene NR films. These films can be transferred first to a deionized water surface and then onto the substrate of interest. <sup>36,38</sup>

Synthesis of  $MoS_2$  Nanowires/Ribbons.  $MoS_2$  NW networks for  $NO_2$  sensing have been recently synthesized via CVD with  $MoO_3$  and sulfur precursors evaporated under turbulent gas flow to allow for kinetic growth of  $MoS_2$  on the substrate. In spite of the existence of methods such as these for synthesizing  $MoS_2$  NWs and NRs, relatively few papers report the application of these nanomaterials in sensors.

Synthesis of Black Phosphorus Nanowires/Ribbons. Recently, BP NWs have been synthesized using anodic aluminum oxide membranes as a template. Fabricated templates are mixed with red phosphorus (RP) and subjected to a series of steps altering the temperature and pressure. This process transforms RP into liquid white phosphorus (WP), which fills the nanopores in the template. WP trapped inside the template is then transformed into BP, and the template is partially etched to reveal BP NWs. However, as in the case of TMDCs nanoribbons, BP has not yet significantly impacted sensor science. To date, only one sensing study has been performed using black phosphorus (BP) NWs to our knowledge.

**Transduction Mechanisms in CNTs and Layered Material NRs.** Chemiresistive. Chemiresistive transduction for the detection of gases, most commonly, is caused by charge transfer from the target molecule to or from the sensing element. In the case of carbon-based, <sup>41</sup> MoS<sub>2</sub><sup>5</sup> and BP sensors, <sup>42</sup> exposure to NO<sub>2</sub>, an oxidizing gas, for example, induces the oxidation of the semiconducting channel material by the injection of holes. This increased p-doping of the channel causes an increase in its electrical conductivity. <sup>36,40–42</sup> Reducing gases like ethanol, methanol, and NH<sub>3</sub> are hole acceptors that decrease the hole concentration upon adsorption and increase the resistance in these same systems. <sup>38,40,43,44</sup> It is also possible for gas molecules to interact *indirectly* via molecules or particles functionalized onto the surface of a carbon or semiconductor channel with a similar effect but altered kinetics for the electron transfer process. <sup>45</sup>

In general, increasing the surface area-to-volume ratio increases the chemiresistive response. NRs of layered materials have particularly active edge sites that can be further enhanced with functionalization. Additionally, at room temperature, active sites can be occupied by oxygen and water leading to attenuation of the response to the analyte of interest. In this case, operating the sensor at an elevated temperature can increase the availability of active sites as oxygen and humidity are desorbed. Temperature elevation may also cause slight changes to the organization of the nanostructures and increase diffusion of certain analytes, resulting in an increased signal.

As in gas sensing, the detection of molecules and biomolecules in liquids can also occur via charge transfer from analyte molecules. Charges biomolecules, such as DNA, can donate electrons and decrease the charge carrier concentration in p-type semiconductors causing an increase in resistance.<sup>47</sup> Alternatively, chemiresistive signal transduction in CNT mats can be due to changes in intertube electron hopping or dipole interactions.<sup>48–50</sup>

Field-Effect Transistors (FETs). In a FET, the conductivity of a semiconducting channel located between the source and drain electrodes is used to sensitively detect a charged target analyte. Signal transduction in this case is caused by a Coulombic interaction between the immobilized charge on the channel and mobile electrons or holes within it. For example, the immobilization of negatively charged DNA reduces the concentration of the majority of the electrons in an n-type silicon nanowire, increasing its resistance. Transistors are three terminal devices, but charged analyte molecules comprise the gate signal in many two terminal FET devices. However, a third gate electrode is sometimes used to modify the response of the FET by capacitively depleting or enhancing the concentration of the majority of the carriers in the semi-conducting channel.

CNT-FETs are of particular interest due to the small size and large surface-to-volume ratio of CNTs, which makes the conductance very susceptible to electrical change upon interactions between the sensing material and the target analyte.  $^{19,23,34}$  CNT-FETs typically present p-type characteristics: the application of a positive gate voltage  $(V_g)$  depletes holes, decreasing the source-drain current  $(I_{\rm SD})$ . The detection of an analyte molecule is tracked by measuring  $I_{\rm SD}$ .

In their application as biosensors, CNTs are functionalized with receptors that can be antibodies, aptamers, peptides, and other biorecognition elements.  $^{19,23,25,47}$  Generally,  $I_{\rm SD}$  will decrease as the concentration of analyte is increased due to either charge transfer depletion of holes or scattering effects caused by the analyte interaction with the sensing material. Recently, Liang et al. fabricated a floating gate FET by utilizing a  $Y_2O_3$  insulating layer between the CNT film and the target probe to observe chemical gating induced holes upon DNA binding; thus, an increase in  $I_{\rm SD}$  was observed with analyte binding. With this floating gate configuration, the sensitivity and response of the biosensor are increased since interfering complex effects can be avoided.

Amperometric. For sensors with amperometric transduction, a constant potential is applied across the sensor and charge transfer between the analyte and the sensing layer causes a change in current proportional to the concentration of analyte. Recently, Li et al. monitored current as a function of CNTs bridging the gap between two functionalized electrodes. Only CNTs bound to the target analyte remained intact while unbound CNTs were washed away, leading to a

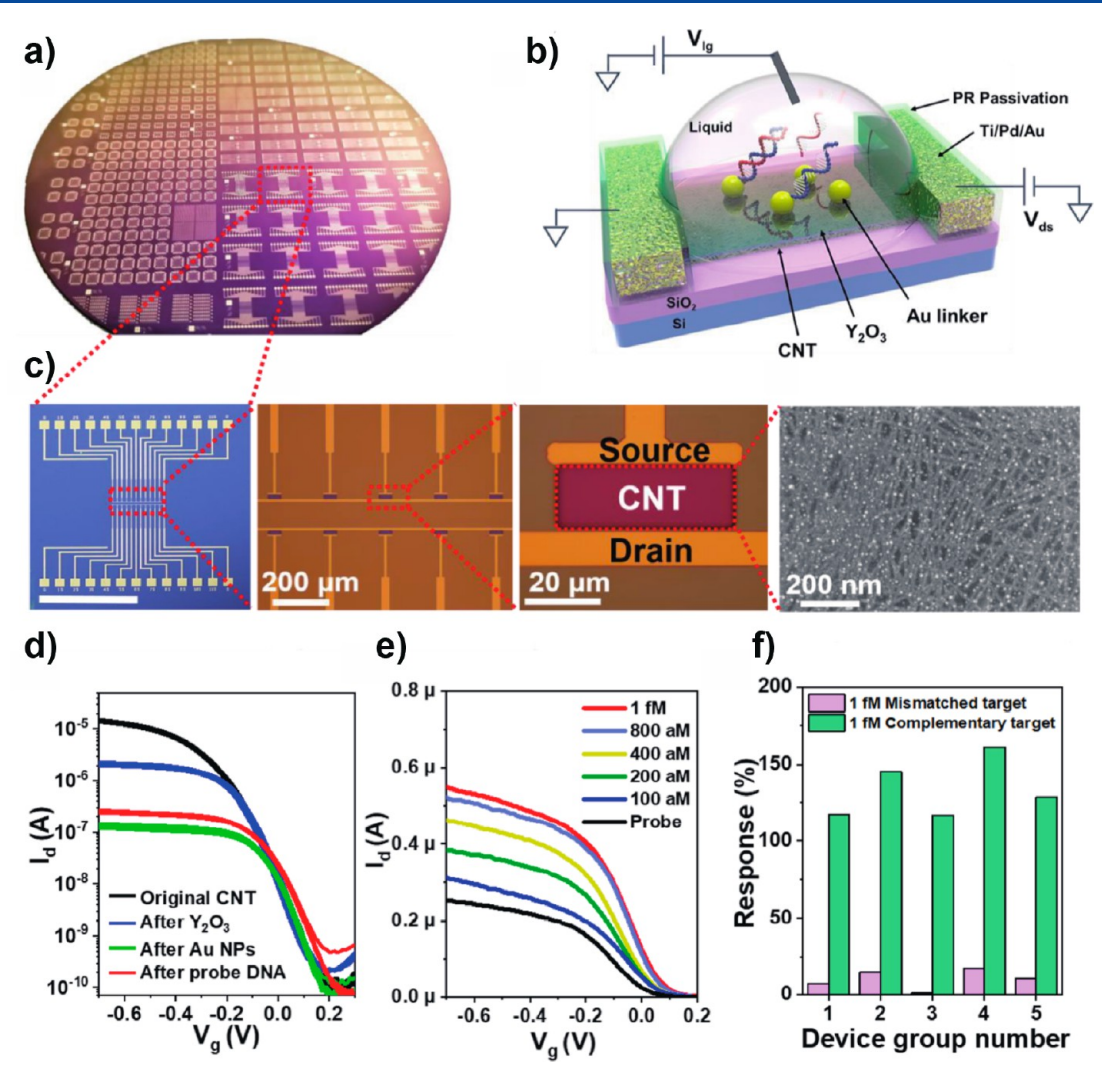


Figure 2. CNT-based FET biosensor arrays in wafer-scale. (a) Photograph of a CNT device array. (b) Schematic diagram of a CNT-based FET biosensor. (c) From left to right, further magnified optical/SEM images. A die for biosensor array, the core channel regions of the biosensor array, a single FET sensor, and a SEM image of the Y<sub>2</sub>O<sub>3</sub>/CNT film. (d) Transfer curve evolution of the biosensors for the decorating process. (e) Transfer curve evolution of the biosensor after injection of target DNA (ranging from 100 aM to 1 fM). (f) Selectivity test for mismatched and complementary DNA at 1 fM. Reproduced from Liang, Y.; Xiao, M.; Wu, D.; Lin, Y.; Liu, L.; He, J.; Zhang, G.; Peng, L.-M.; Zhang, Z. Wafer-Scale Uniform Carbon Nanotube Transistors for Ultrasensitive and Label-Free Detection of Disease Biomarkers. ACS Nano 2020, 14 (7), 8866–8874 (ref 25). Copyright 2020 American Chemical Society.

current from these bridging CNTs that was proportional to the amount of target analyte.<sup>21</sup>

Recent Research. CNTs. The application of CNTs in sensors is made more difficult by the variability of CNT properties due, in part, to the coexistence of metallic and semiconducting CNTs in most synthesis processes, but progress toward high purity CNTs with precisely defined electronic properties has been reported. CNTs that have 95% semiconducting character have been achieved using a CVD growth method.<sup>52</sup> Wet chemical approaches exploiting selective surfactants have demonstrated even better results coupled with greater process simplicity and scalability,<sup>53</sup> but contamination of the resulting refined CNTs by residual surfactant degrades their electronic properties. An important advance has involved the use of conjugated molecules in organic solvents instead of surfactants to select and solubilize semiconducting CNTs from mixtures. A higher purity of 99.9% has been achieved using this approach, culminating in the

realization of excellent electronic properties for TFTs including mobilities of 300 cm $^2$  V $^{-1}$  s $^{-1}$  and on—off ratios of  $10^8$ .

Using such ultrahigh purity CNTs, Liang et al. <sup>25</sup> described CNT-based FET biosensor arrays on a 4-in. wafer based on employing conjugated molecules. In their study, the CNTs are uniformly formed in wafer-scale and an ultrathin dielectric  $Y_2O_3$  film is deposited on the CNT film channel. AuNPs are decorated onto the  $Y_2O_3$  film and provide binding sites for thiolated DNA. The  $Y_2O_3$  film minimizes damage and limits DNA coverage by allowing signal transduction to the "buried" CNTs without direct attachment of the ss-DNA. A boosted sensor response for target DNA hybridization results in a LOD of 100 aM (Figure 2).

Signal amplification strategies have also been applied to increase sensitivity. One of the representative signal amplification methods for gas detection is decoration with metallic nanoparticles on CNTs. The decoration of CNTs with Pd NPs confers a strong response to  $\rm H_2$  gas. In 2017, Li et al.  $^{32}$  described the Pd NP decorated CNT-based sensor and

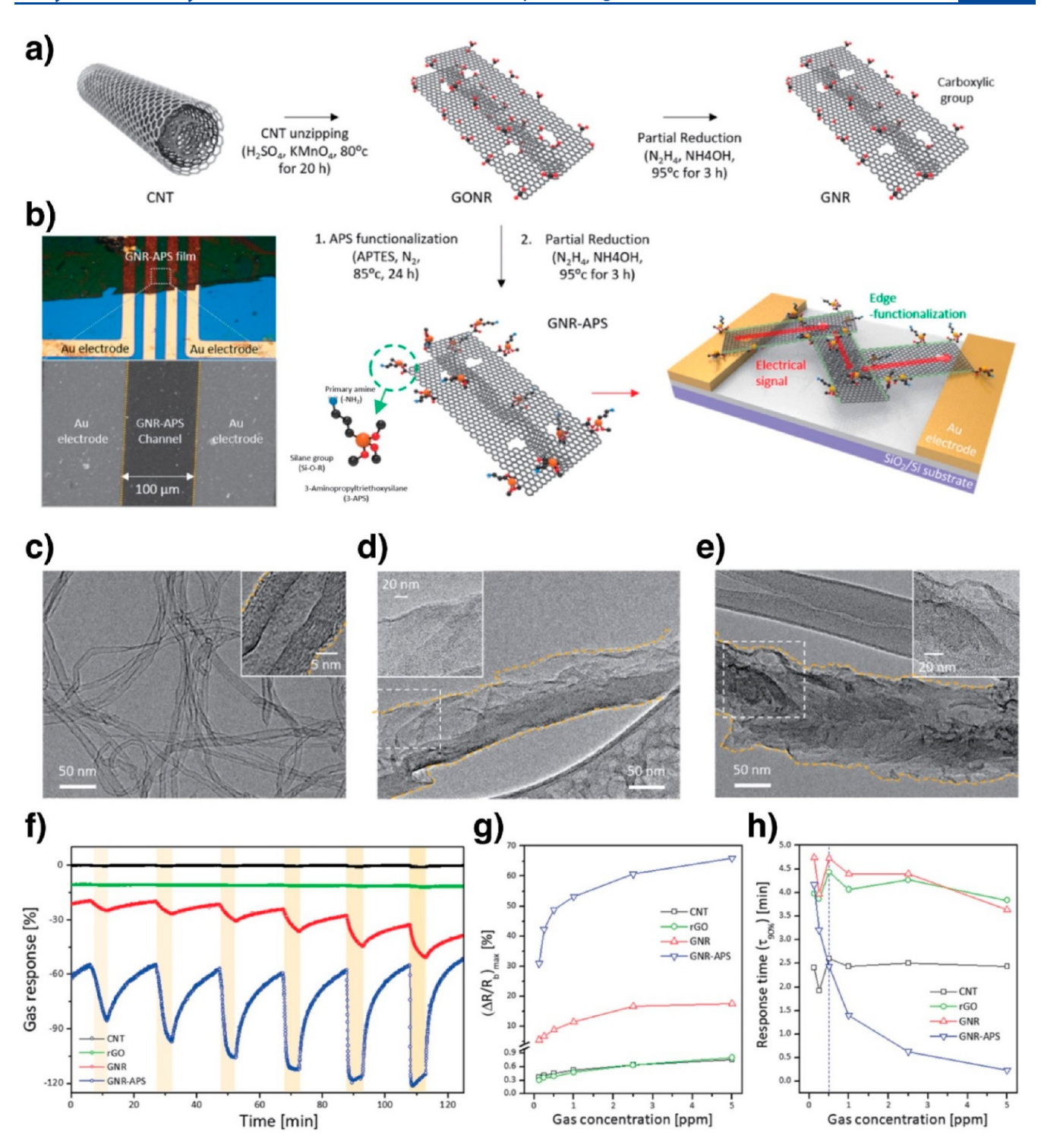


Figure 3. Graphene NR-APS-based NO<sub>2</sub> sensor. (a) Schematic of the synthesis of graphene NR and graphene NR functionalized with aminopropylsilane (GNR-APS). (b) OM and SEM images of the graphene NR-APS sensor structure. Transmission electron microscopy (TEM) images of (c) CNTs, (d) a graphene NR, and (e) graphene NR-APS (magnified images of the white-dashed box regions are shown in the inset). (f) Real-time sensing performance of CNT, rGO, graphene NR, and graphene NR-APS sensors for various concentrations of NO<sub>2</sub> from 0.125 to 5 ppm. (g)  $(\Delta R/R_b)_{max}$  (%) and (h) response time  $(\tau_{90\%})$  of the sensors calculated and plotted for various concentrations of NO<sub>2</sub>. Reproduced from Cho, K. M.; Cho, S.-Y. Y.; Chong, S.; Koh, H.-J. J.; Kim, D. W.; Kim, J.; Jung, H.-T. T. Edge-Functionalized Graphene NR Chemical Sensor: Comparison with Carbon Nanotube and Graphene. ACS Appl. Mater. Interfaces 2018, 10 (49), 42905–42914 (ref 41). Copyright 2018 American Chemical Society.

established the effect of Pd nanoparticle diameter on the sensor sensitivity and response time. The proposed sensor achieved a surprisingly low detection limit of 10 ppm by the

chemiresistive sensing technique. Using an analogous strategy, Seekaew et al.  $^{33}$  reported the use of TiO $_2$  NP-decorated CNTs

Table 2. Metal NW-Based Sensors<sup>a</sup>

sensor	synthetic method	mechanism	category	target	LOD and range <sup>b</sup>	$t_{\rm res}/t_{\rm rec}^{}$	ref
Pd@Ag hollow NW	LPNE/GRR	CR	gas	$H_2$	900-100 ppm (100 ppm)	120 s/102 s	70
PAN@Pd yarn	ES	CR	gas	$H_2$	4-0.0001% (1 ppm)	12 s/124 s	74
half-pipe Pd NT	ES	CR	gas	$H_2$	1.6-0.6% (314 ppm)	11 s	93
Pt NW PtO <sub>x</sub> NW	EBL	CR	gas	$H_2$	1000-0.5 ppm (100 ppm)	25 s/108 s	92
Te NW with Pt catalyst	ST	TC	gas	$H_2$	3-0.005% (50 ppm)	6 s/5.1 s	97
Pd NW with ZIF-8 sieve	LPNE	CR	gas	$H_2$	1-0.02% (600 ppm)	30 s/8 s	94
Au NW array	electroless plating	EC	bio	$H_2O_2$	$10-0.0005 \text{ mM} (0.5 \mu\text{M})$	4 s	85
branched Ag NW	spray-coating, ED	optical (SERS) EC	bio	$4-ATP H_2O_2$	$0.25-300 \ \mu M \ (10^{-16} \ M)$	1 h	73
CoS <sub>2</sub> NW with Au NP	HT	optical (chemiluminescence)	bio	$H_2O_2$	$100-1 \ \mu M \ (0.3 \ \mu M)$	2 min	247
Co <sub>3</sub> N NW array	HT	EC (CV)	bio	glucose H <sub>2</sub> O <sub>2</sub>	2.5-0.0001 mM (50 nM) [glucose]	5 s	105
Pt@In <sub>2</sub> O <sub>3</sub>	ES	CR	gas	acetone	2000-50 ppb (10 ppb)	14/16 s	96
CuAuPd NW	solution	EC (CV, EIS)	bio	protein (Sema3E)	10-0.0001 ng mL <sup>-1</sup> (1.5 fg mL <sup>-1</sup> )	2 h	77
Au NW with DNAzyme	CVT	optical (SERS)	liquid	$UO_{2}^{2+}$	$10^{-7} - 10^{-12} \text{ M (1 pM)}$	60 s	98
Au NW vesicles	OA	optical (SERS and colorimetry)	bio	bacteria (VP)	10 <sup>8</sup> -10 CFU/mL (10 CFU/mL)	20 min	72
PtNi jagged NW	ST	EC	bio	caffeic acid	$0.75-600~\mu M~(0.5~\mu M)$		106
Au NT	galvanostatic deposition	EC	bio	glucose	16.4-0.005 mM (2.1 μM)	5 s	82
Cu <sub>3</sub> P NW	HT	EC	bio	glucose	$1-0.005 \text{ mM} (0.32 \mu\text{M})$	5 s	248
Ag NW with Si/graphene FET	PL	EC (enzymatic CV)	bio	glucose	$10^{-3} - 10^1 \text{ mM } (0.4 \ \mu\text{M})$		249
Ni/Au multilayer NW	ED	EC	bio	glucose	$2-0.00025 \text{ mM} (0.1 \mu\text{M})$	<5 s	81
Au/NiO <sub>1-x</sub> NW array	ED	photo-EC	bio	glucose	15-0.005 mM (0.001 mM)		84
MWCNT/Ni-Co NW	CVD	EC (CV)	bio	glucose	$10-0.005 \text{ mM} (1.2 \ \mu\text{M})$	5 s	250
vertical Pt NW/AuNP array	ED	EC (enzymatic CV)	bio	glucose	$2.5-0.015 \text{ mM} (11.2 \ \mu\text{M})$	10 s	79
Ag NW with M13 bacteriophage	commercial	optical (SERS)	bio	pesticide	20-2000 ng/cm <sup>2</sup>	5 s	99
AuPt NW network with PDA coating	HT	EC	bio	pesticide	1000-0.5 ng/L (0.185 ng/L)		76
G/Au NW	HT	EC (CV)	bio	tulobuterol	7.6–0.076 $\mu$ mol L <sup>-1</sup> (0.0136 $\mu$ mol L <sup>-1</sup> )	7 min	89
Au NW	OA	CR	bio	dopamine	$10^{-2} - 10^{-8} \text{ M } (10^{-8} \text{ M})$		251
Ni NW	ED	EC (CV)	bio	formaldehyde	$20-0.01 \text{ mM } (0.8 \ \mu\text{M})$	10 s	83
Cu(OH) <sub>2</sub> @Cu MOF NW	topotactic fabrication	EC (SWV)	bio	PSA antibody	100 fg/mL-20 ng/mL (4.39 fg/mL)	35 min	68
Pt@Pd NW with DNA probe	HT	EC (DPV)	bio	bacterial DNA (MP)	20-0.0001 nM (0.033 pM)	120 min	87
capped Au NW array	NIL	optical (SERS)	bio	cancer DNA	$(4.1 \times 10^{-5} \text{ RIU})$	5 min	252
Au NW	OA	CR	bio	DNA	1-0.001 nM (1 pM)		253
nanogap-rich Au NW array	VT	optical (SERS)	bio	cancer cells	$10^4$ -0.2 cells mL <sup>-1</sup> (0.2 cells mL <sup>-1</sup> )	125 s	100
Au NW	NIL	EC (SWV)	bio	CRP	220-5 fg/mL (2.25 fg/mL)	30 min	75
Ag NW	commercial	PR	physical	strain	80-0% strain (0.2%)		102
Au NW	nanoskiving	PR	physical	strain	0.07-0.0015% strain (0.0015%)	<1 s	101
Ag NW	stamp patterning	PC	physical	strain	0-30% strain (0.05%)	<1 s	104
Ag/Au NW network	HT	PR	physical	strain	0-70% strain (0.05%)	<1 s	103
mushroom Au NW	ED	PR, EC	physical bio	strain glucose	0-20% strain (5%)	<1 s	71

<sup>&</sup>quot;Abbreviations: NW = nanowire, NT = nanotube, NP = nanoparticle, LOD = limit of detection,  $t_{\rm res}$  = response time,  $t_{\rm rec}$  = recovery time, 4-ATP = 4-aminothiophenol, CR = chemiresistive, CRP = C-reactive protein, CV = cyclic voltammetry, CVT = chemical vapor transport, EBL = electron beam lithography, ED = electrodeposition, EIS = electrochemical impedance spectroscopy, ES = electrospinning, FET = field-effect transistor, G = graphene, GRR = galvanic replacement reaction, HT = hydrothermal, LPNE = lithographically patterned nanowire electrodeposition, MOF = metal—organic framework, MP = Mycoplasma pneumonia, MWCNT = multiwalled carbon nanotube, NIL = nanoimprint lithography, OA = oriented attachment, PAN = polyacrylonitrile, PC = piezocapacitative, PDA = polydopamine, PL = photolithography, PR = piezoresistive, PSA = prostate-specific antigen, SERS = surface-enhanced Raman spectroscopy, SWV = square-wave voltammetry, TC = thermochemical, VP = Vibro parahemolyticus, and VT = vapor transport.  $^b$ Values for response/recovery times, limits of detection, and operating ranges are as defined by the authors.

for the detection of toluene vapor at room temperature. These sensors produced a limit-of-detection for toluene of 50 ppm.

Layered Materials. Graphene NRs have been actively investigated in this period, but in applications aimed at

sensing, films of graphene NRs rather than single or aligned graphene NR arrays have been the focus. In 2017, Mehdi Pour et al.<sup>38</sup> synthesized laterally extended chevron graphene NRs with a lower band gap and better conductivity than chevron graphene NRs. Fabrication of the devices makes use of the interfacial self-assembly approach in which the graphene NRs self-assemble in an edge-geometry, which results in films with laterally aligned graphene NRs. This allows for accessible interplane spacings for the intercalation of MeOH and EtOH gas molecules, increasing the electrical conductivity and gas sensing capabilities.<sup>38</sup>

A baseline graphene NR response for a target molecule can be tuned by chemical functionalization of the graphene edges. Cho et al. explored the differences in sensing between plain CNTs and graphene versus functionalized CNTs and graphene. Functionalization of the graphene NRs with aminopropylsilane (APS) provides extra binding sites for gas molecules in addition to the ribbon surface, resulting in an enhanced sensitivity as compared to traditional and nonfunctionalized carbon nanomaterial sensors (Figure 3). Overall, compared to graphene NRs, these APS edge functionalized graphene NRs were 7 times more sensitive and 15 times faster. More impressively, the graphene NR-APS sensors were 30 and 93 times more sensitive compared to CNTs, and rGO, respectively. <sup>41</sup>

The common unzipping methods used to synthesize graphene NRs can involve the use of aggressive reagents and processes resulting in damage to the graphene, degrading the performance of these materials as sensing elements. Lee et al. 46 used a gentle, two-step electrochemical—sonochemical unzipping method of nitrogen doped CNTs to retain the crystallographic integrity of graphene NRs. Most notably, these NWs exhibited an improved signal-to-noise ratio as expected. 46

In 2018, Kumar et al.<sup>5</sup> studied NO<sub>2</sub> gas sensing with a CVD-grown MoS<sub>2</sub> NW network. The adsorption of NO<sub>2</sub> to MoS<sub>2</sub> edge sites is both selective and strong, resulting in a 16 s response time and a much slower 172 s recovery time, both of which are superior to other MoS<sub>2</sub> gas sensors. This is theorized to be due to the high electrical conductivity of the NWs and the diffusion of gas molecules through the NW network.<sup>5</sup>

Black phosphorus NWs have been used as sensors recently with incredible selectivity toward NO<sub>2</sub>. Compared to bulk BP sensors, the BP NWs sense NO<sub>2</sub> twice as fast with four times the signal amplitude, performance that is attributed to the high surface area and enhanced number of defect sites available for NO<sub>2</sub> adsorption. Additionally, the BP NW sensor shows excellent stability and durability in ambient conditions unlike 0D and 2D BP, both of which degrade due to surface damage. On the selection of the surface damage.

**Opportunities and Challenges.** CNTs for Practical Devices. In spite of much progress,  $^{23-25,27,32,33,345}$  a number of challenges exist. In the area of gas sensing, although Li et al. al. demonstrated an improved response (62 s) and recovery time (72 s) for  $H_2$  achieved by decreasing the diameter of Pd NPs dispersed onto CNTs, sensors capable of even faster, real-time response to  $H_2$  are still required.

Layered Materials. Several synthetic methods for nanowires/ribbons of layered materials have been reported, but in many cases, these systems have not yet been tested in sensors. Single graphene NRs, MoS<sub>2</sub> NRs, and BP NRs devices have been fabricated using top-down lithographic or nanosculpting methods that involve masking and patterning 2D nanosheets

and/or etching away material using reactive ion etching (RIE), scanning tunneling microscopy (STM), or other strong electron or ion beams.  $^{54-60}$  Several methods have been previously studied to synthesize  $\rm MoS_2$  nanowires.  $\rm MoO_x$  or Mo NWs can be sulfurized at temperatures of 700 °C or higher to produce  $\rm MoS_2$ . More recently, the use of self-assembled block copolymer templates have been explored for the fabrication of sub-20 nm  $\rm MoS_2$  NW arrays, but these have yet to be used for sensing.  $^{63,64}$  The application of exfoliated 2D materials reconstituted as NWs as sensing elements has been impeded by the excessive cost and processing effort required to prepare such NWs, with the result that the performance of these systems for sensing have hardly been tested.

A family of emerging 2D layered materials, the MXenes, discovered by Hantanasirisakul and Gogotsi in 2018,65 are 2D materials composed of transition metal (M) carbides, carbonitrides, and nitrides (X) with OH, O, and/or F surface terminations. The combination of the MX backbone and surface terminations makes these materials both conductive and hydrophilic. Endless M and X combinations with over 30 already experimentally realized allows for highly customizable properties. Changes in the interlayer spacing of MXenes results in changes in conductivity, which makes them strong candidates for pressure and strain sensors. The conductivity of MXenes is also highly sensitive to molecular adsorption, allowing for chemical, gas, and biomolecule sensing. 65 Yarns and fibers containing MXenes have been studied for strain sensors, and films containing MXenes have been studied for chemical and gas sensing; however, the realization of MXene or MXene containing NW/NRs has yet to be achieved. 6,7,60

#### METAL NANOWIRES

Introduction and Background. Metal NWs have been explored as sensing elements because they possess sensitivity for various analytes (e.g., H<sub>2</sub>), are straightforward to synthesize, and are mechanically robust. They can be composed of single metals (Ag, Au, Co, Ni, Pb, Pt), bimetallic composites (core-shell or alloys), or even trimetallic alloys. 67-70 To fabricate metal or metal alloy NWs, either a top-down or a bottom-up synthesis method can be used. Common mechanisms of signal transduction include chemiresistance, electrochemical, optical, piezoresistive/piezocapacitative or a combination of two or three of these mechanisms. 71-74 Since 2016, many metal alloys or bimetallic NWs have shown great promise for their electrochemical or chemiresistive properties. 71,75-77 In addition, dual-signal sensors that utilize signal from two or more sources have been at the forefront of NW-based sensor technology (Table 2).<sup>72,78</sup> In this section, we will discuss how these innovative wires are synthesized, the way these NWs generate signal, and several prominent examples of sensors based on these designs.

Synthesis and Fabrication. *Template Synthesis*. Template synthesis coupled with electrodeposition is a convenient and efficient method for synthesizing ensembles of metal NWs with excellent diameter uniformity and high number density on many conductive substrates. Templates for electrodeposition of metal NWs can be classified into two categories: soft templates use polycarbonate and surface stabilizing molecules, and hard templates are composed of anodic aluminum oxide (AAO), carbon nanotubes (CNTs), and mesoporous oxides (MOs). Anodic alumina templates have been widely used for making metallic NWs composed of Pt, Au, Cu, Ni, Pd, and Ag due to the tunable pore size and thermal durability of this

method.<sup>79</sup> The template-assisted electrodeposition method has some limitations such as the significant complexity associated with processes for assembling of soft or hard templates<sup>80</sup> and the difficulty of template removal for some systems. To overcome these drawbacks, a recent focus has been on the simplification of template synthesis procedures.<sup>81–83</sup>

Wang et al.<sup>84</sup> demonstrated a convenient way of synthesizing the  $Au_x - NiO_{1-x}$  (0 < x < 1) hybrid NW arrays using an to "electrodeposition method for the detection of glucose. The authors prepared Au<sub>x</sub>-NiO<sub>1-x</sub> hybrid NW arrays through the incorporation of gold nanoparticles into a NiO<sub>1-x</sub> NW matrix by using template-assisted electrodeposition with an oxidization reaction of Au-NiAu nanowires. Qin et al.81 fabricated Ni/ Au bimetallic NWs by a facile template-assisted pulse electrodeposition method for an electrochemical glucose sensor. Trafela et al.<sup>83</sup> used a low-cost electrodeposition method to fabricate a vertically aligned Ni NW modified with an active redox pair of Ni(OH)2 /NiOOH, which is wellknown for catalytic HCHO oxidation properties in alkaline media, for detecting formaldehyde. Ni(OH)2 and NiOOH were oxidized on the surface of the Ni NWs through cyclic voltammetry. Tian et al.<sup>82</sup> demonstrated an Au nanotubular structure that was fabricated uniformly and densely from Au NWs by a simple electrodeposition method in an alkaline

Electroless plating (EP) is a solution-based deposition method for the synthesis of a metal thin layer onto a substrate. EP reactions for plating of NWs can be generate by taking advantage of the catalytic reactive property of metal nanowires. The continuous growth of the metal film can be easily controlled by changing the deposition time.<sup>85</sup> The synthesis method for a vertically aligned Pt NW array (PtNWA) plated with gold nanoparticles was developed by Li et al. 79 for electrochemical biosensors. Electrodeposition was used for fabricating the vertical Pt NW array with an anodic aluminum oxide (AAO) template. After, Au nanoparticles were coated onto the surface of Pt NWs by using the electroless plating method. Au nanoparticles were then functionalized with glucose oxidase. By using a vertical array, the NWs could contain more Au nanoparticles than a conventional 2D planar structure. Muench et al.85 developed a novel template-free electroless plating protocol for the fabrication of gold nanowires. Gold deposition proceeds through the nucleation of new particles on a pre-existing nanostructure; thus, polycrystalline NWs with a high aspect ratio can be obtained. This method can create various shapes and configurations of three-dimensional NW structures on the substrate with different seed types.

Hydrothermal, Solvothermal, and Vapor-Phase Methods. Synthesis methods of metal nickel such as cobalt and nickel have been widely researched using template-free and self-assembly methods in solution from the vapor-phase, solvothermal, or hydrothermal methods. 67,69,86

Liu et al. <sup>87</sup> fabricated Pt@Pd NWs that can mimic enzymatic reactions in gene-detecting biosensors by a one-pot solution synthesis. They prepared Pt@Pd NWs modified with thionine, horse radish peroxidase, and complementary DNA probes with excellent binding affinity to *Mycoplasma pneumonia* DNA. Pt@Pd NWs also have unique peroxidase-like properties for the reduction of H<sub>2</sub>O<sub>2</sub>, which can enhance electrochemical signal of biosensors. Li et al. <sup>88</sup> later presented a method called "precursor solution-aging" for assembling Pt/PtTe NWs that can be used for catalyzing the oxygen reduction reaction.

Single crystalline metal NWs composed of Co, Ni, NiCo, CoFe, and NiFe have been synthesized by Scott et al.<sup>69</sup> using a novel method. In this method, NWs are grown by the reduction of metal nitride precursors that can be gas-phase, solution-phase, or a mixture of gas and solution-phase precursors. Metallic NWs can also be combined with nonmetallic compounds such as CNTs, graphene, or lipid nanotubes.

Huang et al. <sup>89</sup> synthesized graphene/Au NW composites by an electrostatic interaction and applied the process to glassy carbon electrodes for the electrochemical detection of tulobuterol. These NWs were fabricated by water-dispersed graphene from the reaction of graphene oxide in alkaline conditions. Oleylamine was used as a stabilizer and one-dimensional growth template, and triisopropylsilane was used as a reducing agent. A creative and fascinating method to synthesize gold NWs on a lipid nanotube template is demonstrated by Jajcevic et al. <sup>90</sup> Streptavidin-functionalized gold nanoparticles were introduced to a biotinylated lipid template.

Lithographically Patterned NW Electrodeposition (LPNE). Lithographically patterned NW electrodeposition (LPNE)<sup>70,91</sup> is a general tool for preparing nanowires by electrodeposition. In contrast to the more common template synthesis schemes, in which nanowires are electrodeposited into nanoporous templates such as filtration membranes with the long axis of the nanowire oriented perpendicular to the plane of the membrane, the nanowires in an LPNE process are patterned horizontally onto the surface of a dielectric such as glass. The nickel or gold electrode required for the electrodeposition process is removed by etching in the last step of the LPNE process. Photolithography is used to prepare the LPNE template, allowing for the positioning and patterning of nanowires on a surface, but the critical width and height dimensions of the nanowires themselves are not subject to diffraction limitations, a distinct advantage of this fabrication method. While LPNE has been used to prepare nanowires composed of a wide variety of materials, in the context of sensing, it has primarily been used to pattern metal nanowires for applications in H2 gas sensing.

Electron Beam Lithography (EBL) and Nanoimprint Lithography (NIL). Electron beam lithography (EBL), or the direct-writing method, does not need a premade patterned mask for fabricating nanowires. EBL can also be applied for fabricating stamps for nanoimprint lithography (NIL). These methods can provide an extremely high resolution to the NW array but also require expensive equipment and a time-consuming process. EBL forms the basis for the preparation of Pt NW arrays on  $\mathrm{Si/SiO_2}$  by Prajapati et al. 92 who used these systems for the detection of hydrogen gas. Joule heating of these NWs in an oxygen-rich environment enabled a  $\mathrm{PtO_x}$  surface layer to be formed on these Pt nanowires.

**Transduction Mechanisms in Metal Nanowires.** *Chemiresistors.* The simplest metal NW sensors are chemiresistors. That is, the electrical resistance of these NWs increases upon exposure to a target analyte. The simplest example of this are hydrogen sensors based upon palladium nanowires. In this case, a resistance change is produced by the dissociative chemisorption of hydrogen on the Pd surface. Hydrogen atoms diffuse into the Pd, forming a resistive palladium hydride  $(PdH_x)$ . Since 2016, there have been several innovative improvements in the system. NWs accelerate the response of these sensors due to their amplified

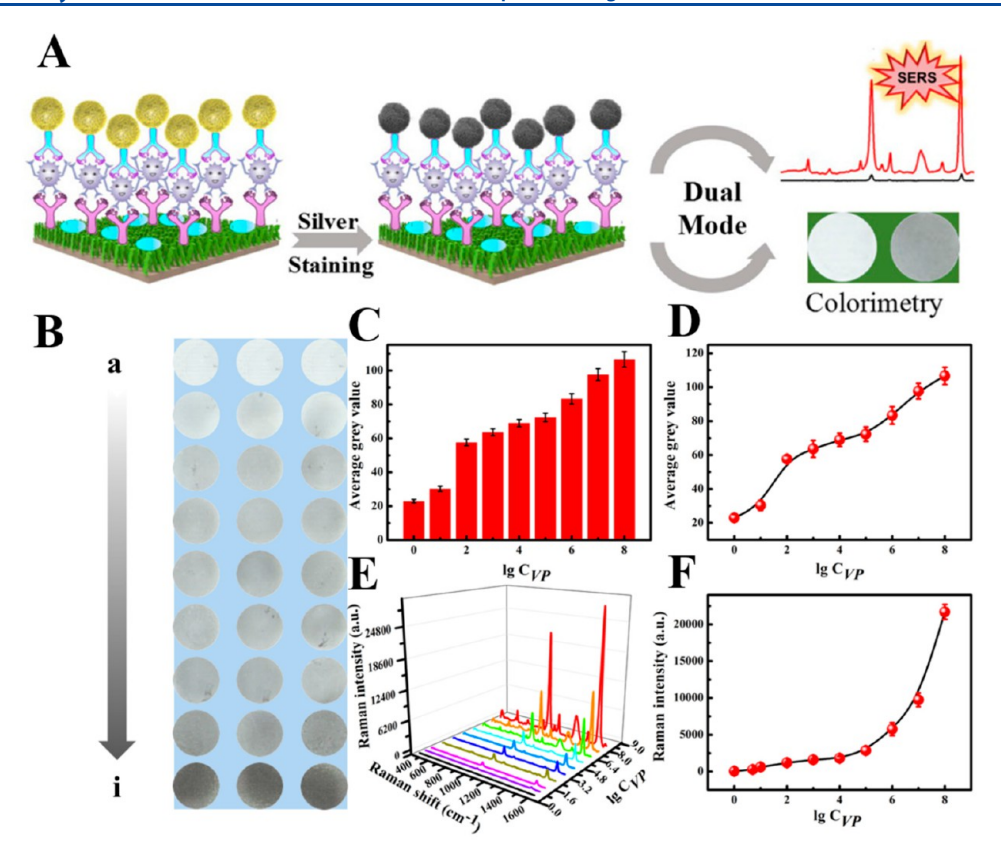


Figure 4. Dual mode immunosensor for *Vibrio parahemolyticus* (VP) detection based on gold NW vesicles.<sup>72</sup> (A) Schematic illustration of the operating principle. First, VP are immobilized on specific antibodies (not shown). Gold NWs form a vesicle with a detection antibody, which is immobilized onto the trapped VP bacteria. The gold NWs undergo gold label silver staining (GLSS), leading to a change perceptible by SERS, colorimetry, and the naked eye. By utilizing two detection methods, the false positives and negatives are minimized, and accuracy is enhanced. (B) Spot images from a–i corresponding to 0, 10, 10<sup>2</sup>, 10<sup>3</sup>, 10<sup>4</sup>, 10<sup>5</sup>, 10<sup>6</sup>, 10<sup>7</sup>, and 10<sup>8</sup> colony-forming units (CFU) mL<sup>-1</sup>. (C, D) Average gray value logarithm intensity and calibration curve of different VP concentrations from B. (E, F) Raman intensity and calibration curve of different VP concentrations from (B). Reproduced from Guo, Z.; Jia, Y.; Song, X.; Lu, J.; Lu, X.; Liu, B.; Han, J.; Huang, Y.; Zhang, J.; Chen, T. Giant Gold NW Vesicle-Based Colorimetric and SERS Dual-Mode Immunosensor for Ultrasensitive Detection of Vibrio Parahemolyticus. *Anal. Chem.* 2018, 90 (10), 6124–6130 (ref 72). Copyright 2018 American Chemical Society.

surface area to volume ratio because the rate-determining step of the sensor response is the adsorption of  $H_2$ .

Whereas Pd NWs exploit the increased bulk resistivity of PdH<sub>x</sub> relative to Pd, chemiresistive NW sensors can also utilize a surface-scattering mechanism in which the "reflectivity" of the interface to electrons is altered by the adsorption of a target analyte. Increases in carrier reflectivity, usually called specularity, increase the conductance of a metal nanowire; conversely, decreases in specularity increase its resistance. In air, the surfaces of platinum NWs are covered with chemisorbed water and hydroxyl. Exposure to hydrogen gas promotes the reaction of these oxygen-containing species to form water that desorbs from the surface and is replaced by a hydride termination on the platinum that has a higher specularity, resulting in a lower resistance for the nanowire.

Chemisorbed water and OH<sup>-</sup> on platinum NWs can also interfere with the reaction of target analytes with the surface of a platinum nanowire. Liu et al. <sup>96</sup> covered In<sub>2</sub>O<sub>3</sub>-functionalized Pt NWs in a hexagonal mesoporous silica, SBA-15, as a molecular desiccant. SBA-15 removes water by hydrolyzing its siloxane bonds, preventing water molecules from interacting with the NW surface and enhancing the response time in real breath samples. Molecular sieves are an innovative way to overcome issues with interfering molecules and can be applied to a wide range of chemiresistors.

Thermochemical. Thermochemical mechanisms have been another innovative mechanism for nanostructured gas sensors. While film-based sensors were first described in 2001 for hydrogen detection, they have only recently adapted to metal NW-based sensing elements. <sup>97</sup> Usually, these devices consist of two components: a catalyst to react with the analyte gas and produce/absorb heat and a thermoelectric NW to convert a temperature difference into a voltage signal. The temperature change generated by the catalyst can be related to the Seebeck coefficient of the thermoelectric NW by eq 1: <sup>97</sup>

$$\Delta V = \alpha \Delta T \tag{1}$$

where  $\Delta V$  is the voltage difference across the nanowire,  $\alpha$  is the Seebeck coefficient of the nanowire, and  $\Delta T$  is the temperature change. Since the signal  $\Delta V$  is dependent on a temperature change  $(\Delta T)$ , thermochemical devices are only functional for analyte gases that can undergo a large enthalpy change. Using a tellurium NW as a thermocouple, Hwang et al.  $^{97}$  were able to detect the enthalpy change from hydrogen degradation by platinum nanoparticles. This sensor operates at a low power, is resistant to humidity, and is faster than previously developed thermochemical hydrogen sensors.

Optical. Photon scattering from NWs has also been exploited to transduce the adsorption of analyte molecules onto nanowires. To fabricate optical sensors, arrays of NWs

(typically gold or silver) are functionalized with a biorecognition agent, which can vary from large viruses to molecules of nucleic acids. <sup>72,98,99</sup> While random arrays are typically easier to fabricate, plasmonic NW arrays with selective spacing and alignment can benefit from the enhanced signal. The selectivity of optical sensors relies on the selectivity of the biorecognition agent, as the metal NWs do not typically react with analytes. This array of functionalized NWs is then analyzed using techniques such as surface-enhanced Raman scattering (SERS), resonance Rayleigh scattering (RRS), or colorimetry.

Within this category, SERS is most commonly used for the interrogation of NW sensors. Eom et al. 100 developed a telomerase biosensor for cancer detection by using nanogap gold NWs functionalized with a telomerase-selective fragment of DNA (Figure 4). Telomerase, up-regulated in some cancers, causes the elongation of these primer strands, which can then be transduced by SERS. Using a similar principle, Gwak et al.98 utilized a DNAzyme that is highly selective for UO<sub>2</sub><sup>2+</sup> in water samples. Aqueous UO<sub>2</sub><sup>2+</sup> causes site-specific cleavage of this DNAzyme at a rate much higher than other metal ions and allows detection by SERS. Both sensors exhibit extreme selectivity due to their nucleic acid-based indicators and benefit from the LSPR signal enhancement generated by patterned NW arrays. With immobilized M13 bacteriophages on a silver NW network, Koh et al. 99 were able to determine the pesticide concentration in fruit samples by using SERS. In this case, the random orientation of the silver NWs generates stacking of hot spots in a high density. By using a genetically modified M13 bacteriophage with chemical-selective proteins, this platform can be easily modified by changing the phage's surface peptide

*Electrochemical*. Metal NWs are often used as electrodes for redox-active analytes in electrochemical sensors. The large surface area to volume ratio of NWs makes them excellent at transferring charge to and from analytes. As indicated above, in this Review, we do not discuss sensors that exploit NWs simply to enhance the interfacial surface area of the electrodes.

Piezoresistive/Piezocapacitive. Sensors based upon changes in the strain accompanying the adsorption of molecules to NWs exploit either of the two mechanisms. Piezoresistive NWs directly convert mechanical strain into a change of resistance. Jibril et al. were able to develop a single NW strain sensor from a sub-10 nm gold nanowire. The signal in this system was derived from differences in electron scattering between unbent and bent nanowires. 101 In addition to single NWs, networks of NWs can be used as piezoresistors. In these cases, the number of NW contacts determines the overall conductance of the device. By simply dipping a polyurethane sponge in a conductive cellulose/silver NW solution, Zhang et al.<sup>102</sup> were able to develop a piezoresistor capable of detecting a strain from 0.2% to 80% with an incredibly reproducible response pattern and a gauge factor (or sensitivity, defined as  $(\Delta R/R_0)$ /strain) of 26.07. Changes in resistivity for these NW ensembles were attributed to changes in the number of connections between silver NWs in the ensemble of the nanowires. Ho et al. 103 combined gold and silver NWs to produce a tunable strain sensor. With an increase in the ratio of softer gold NWs relative to harder silver NWs, the detection of higher strain values is enabled. These transparent sensors were able to detect strain as low as 0.05% and as high as 70%, with a maximum gauge factor of 236 at low strain.

Piezocapacitive sensors leverage a capacitance measurement to detect the strain generated within the dielectric of a capacitor by analyte molecules partitioning into this dielectric layer. <sup>104</sup> In these devices, the electrodes of the capacitor can be comprised by nanowires. For example, Kim et al. <sup>104</sup> used interdigitated patterns of electrodes made up of randomly oriented silver nanowires. Each finger of the electrode creates an electric field with its neighbor through charging, and the device operates as a series of parallel capacitators. Stretching the electrode in the x-direction results in an increase in the electrode distance, which in turn affects the capacitance of each finger and allows the detection of up to 30% strain.

Multiple Signal Transduction Schemes. By combining two or more of these transduction mechanisms, devices can either detect two different analytes or obtain two estimates for the concentration of a single analyte. As shown in Figure 4, Guo et al.<sup>72</sup> developed a sensor that uses optical colorimetry in addition to SERS to mitigate false positives and false negatives. In this system, vesicles of gold NWs are attached to an antibody for immunodetection of Vibrio parahemolyticus bacteria. By subjecting the attached gold NW vesicle to goldlabel silver staining, the nucleated silver crystals that form on the gold NW vesicle become the main source of signal in both colorimetry and SERS. Zhai et al.<sup>71</sup> were able to develop a dual-purpose array of mushroom-shaped gold nanowires; in addition to enzymatic detection of glucose, the device was able to simultaneously detect the strain through chronoamperometry. Changes in signal can come from two sources: immobilized glucose oxidase can oxidize glucose and undergo direct electron transfer with the gold NW substrate, and the strain can induce cracks on the vertical NW surface to increase resistance. The use of clever combinations of these different signaling mechanisms could provide future NW devices with more flexibility and accuracy.

Recent Research. Hydrogen Sensors. Since 2001, palladium NWs have been developed for the detection of hydrogen gas.<sup>2</sup> Even though this was more than 20 years ago, a number of innovations related to hydrogen sensing have been described. By using a half-pipe or hollow-nanowire design, Kim et al. 14 optimized the surface area of a chemiresistive palladium NW to enhance the response time of hydrogen sensors. <sup>70,93</sup> In these experiments, a yarn of palladium or platinum-functionalized palladium was woven to create a mechanically flexible version of this sensing platform. The macropores created by winding fibers together and the abundance of palladium nanograins and nanogaps in the material also facilitate a faster lattice expansion in the palladium, resulting in a hydrogen sensor with an increased response and recovery time. At 4%, the platinum-functionalized palladium yarn had a response time of 12 s, a recovery time of 48 s, and a 9.5% resistance change. Koo et al.<sup>94</sup> developed a hydrogen sensor with a selective metal-organic framework (MOF), ZIF-8. The hundred-fold improvement to response and recovery times (7 and 10 s, respectively) in this work can be attributed to improvements to adsorption and desorption kinetics due to the removal of larger surface-adhering molecules such as oxygen. With a vast and growing library of MOFs, future chemiresistors can be improved by using a selective coating as a molecular

Jang et al. 70 reported a facile approach for synthesizing hollow Pd-Ag alloy nanowires. After the fabrication of silver NWs by using LPNE, a galvanic replacement reaction was carried out to form palladium nanowires. This reaction causes

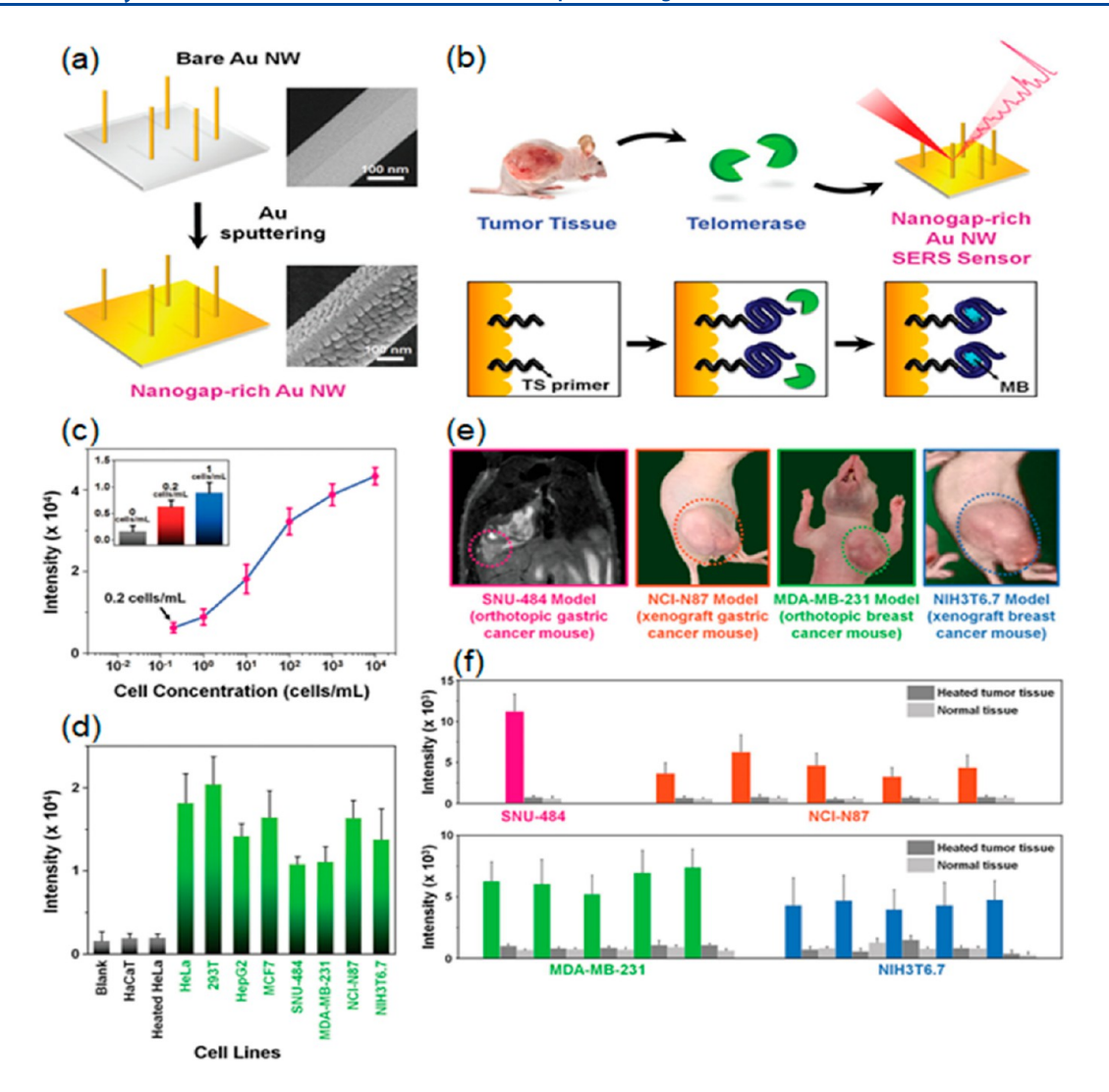


Figure 5. (a) Schematic illustration of procedures for making a nanogap-rich Au NW SERS sensor. Vertical Au NWs are fabricated by vapor transport. (b) Sensing mechanism of the sensor for detecting telomerase activity. Thiolated TS primer is functionalized onto the sensor; then, TS primer is elongated by telomerase, and then, a G-quadruplex structure is formed. MB is combined with the G-quadruplex, and this can amplify SERS signals of the sensor. (c) The intensity of the MB 1620 cm<sup>-1</sup> band is expressed as a function of cell concentration. (d) The intensity of the MB 1620 cm<sup>-1</sup> band in different cell lines. All samples were at a concentration of 10 cells mL<sup>-1</sup>. (e) Images of mice bearing 4 types of tumors. The area of the tumor is marked with dotted circles. (f) The intensity of the MB 1620 cm<sup>-1</sup> band at tumor tissues, heated tumor tissues, and normal tissues obtained from 16 tumor-bearing mouse models. The dark gray and light gray bars show telomerase activities of the heated tumor tissues and normal tissues, respectively. Reproduced with permission from Eom, G.; Kim, H.; Hwang, A.; Son, H.-Y.; Choi, Y.; Moon, J.; Kim, D.; Lee, M.; Lim, E.-K.; Jeong, J.; et al. Nanogap-Rich Au NW SERS Sensor for Ultrasensitive Telomerase Activity Detection: Application to Gastric and Breast Cancer Tissues Diagnosis. Adv. Funct. Mater. 2017, 27 (37), 1701832 (ref 100). Copyright 2018 Wiley.

a hollowing out of the inside and micro/macropore formation, increasing the exposed surface and enhancing the response speed (from 400 to 120 s), recovery time (from 1000 to 102 s), and sensitivity (300% increase) when compared to traditional Pd nanowires.

Hwang et al. <sup>97</sup> developed a thermochemical hydrogen sensor that utilizes tellurium NWs as a thermoelectric layer. The NW array is coupled with a Pt nanoparticle-functionalized graphene layer that generates heat from hydrogen oxidation. Nanomaterial-based thermochemical sensors have only been developed for hydrogen, but other combustible gases could be detected using the NW-thermocouple framework. This sensor can operate at 75% relative humidity, an elusive target in most sensors, and has a rapid response time of 6 s.

Biosensors. Wu et al. 76 have fabricated polydopamine-coated AuPt (AuPt-PDA) hydrogels in the presence of

dopamine, successfully by a one-pot procedure in aqueous solution. The gelation kinetics was dramatically accelerated, and the 3D porous NW structure of the hydrogels could be synthesized within 2 h. These AuPt-PDA hydrogels can be used for the detection of paraoxon-ethyl using differential pulse voltammetry (DPV), a type of electrochemical transduction. The sensor showed a massive dynamic range of 0.5 to 1000 ng  $\rm L^{-1}$  and a limit of detection (LOD) of 0.185 ng  $\rm L^{-1}$ .

While enzymatic sensors have been around since 1962, the integration into NWs has provided an increased sensitivity in these devices. The immobilization of enzymes onto the metal NW is a challenge, and nonenzymatic detection is usually more practical. By using NWs consisting of alternating Ni/Au layers, Qin et al. Were able to construct a nonenzymatic glucose sensor capable of glucose oxidation at different layers of the nanowire. The combination of the two

Table 3. Semiconductor NW-Based Sensors<sup>a</sup>

		6					9		0	0		£,		9	8	9				ics.	3									2	6		<u>.</u>	7	<u>.</u>		9	4	7
ref	113	129	108	137	135		% 136	111	130			n 123		ıt 126	138	146	144		143											132	139		140		A 127			114	117
analysis time	18 s (UV illumination) 518 s (dark)	60 s (est. <sup>b</sup> for 1 fg/mL)	1 min (est. for 1 nM)	10 s (est. for 30 pM)	80 s (est. for 4 mM	glucose in blood)	10 s (est. for 1 fM in 20% serum)	10 s	25-30 min	N/A	28 s (est. $t_{90}^{c}$ at 400 ng/mL)	4 min (est. for 1285 ppm	ethanol)	$\sim 90/125$ s for $t_{\rm res}/t_{\rm rec}^{\ d}$ at 120 ppm	N/A	N/A	4 s		30 min											90 min	0.1 h		N/A	10 s	100 s (est. for 1 nM PSA	ın plasma)	~5 min	3 s/148 s $(t_{res}/t_{rec}$ for 50 ppm NO <sub>2</sub> )	N/A
range (LOD)	0.5–360 ppb (0.5 ppb under UV illumination, 4.5 ppb in dark)	0.5 fg/mL-10 ng/mL (0.5 fg/mL)	$1 \text{ nM} - 1 \mu \text{M} (100 \text{ pM})$	<20 fM->200 pM (30 aM after 55 cycles of amplification)	0.1-10 mM	100 nM-1 mM	1 fM $-1$ pM (0.72 fM in PBS/1.1 fM in 20% serum)	10 ppb=10 ppm (10 ppb)	$25 \text{ fM} = 25 \text{ nM} (\sim 80 \text{ fM in } 0.01 \times \text{PBS})$	1 pg/mL-1 µg/mL (1 pg/mL)	33–1000 ng/mL (10 ng/mL ~200 pM in 2 mM PBS)	26–2030 ppm (26 ppm)	40–2800 ppm (40 ppm)	30–120 ppm (20 ppm)	$5-100  \mu \mathrm{g/mL}$	$1 \text{ nM} - 1 \mu \text{M} \text{ (1 nM)}$	pH 3-11	50.9 mV/pH	100–870 ppb (1 ppb)	2.6–21 ppb (3 ppb)	0.98-7.9 ppb (3 ppb)	8-65 ppb (120 ppb)	50-420 ppb (1000 ppb)	2-15 ppb (20 ppb)	460–3680 ppb (10 000 ppb)	0.29–2.36 ppb (20 ppb)	170–1360 ppb (4000 ppb)	34–273 ppb (330 ppb)	300–2420 ppb (25 000 ppb)	0.2-280 ng/mL (0.14 ng/mL)	$(1  \mu \mathrm{g/mL})$	$100 \text{ ng/mL} - 10 \mu\text{g/mL} (100 \text{ ng/mL})$	5-200 pg/mL (5 pg/mL)	$5 \mu M - 10 \text{ mM } (1 \mu M)$	10 pM $-1~\mu M$ (10 pM in 100 mM PBS)	(100 pM in plasma)	$0.1 \text{ pg/mL} - 10 \mu\text{g/mL} (0.1 \text{ pg/mL})$	1–50 ppm (36 ppb)	1–50 ppm (0.14 ppm)
analyte	$NO_2$	CYFRA21-1	TNT	IL-2	glucose	$H_2O_2$	FSP	ethanol	KRT-19	PSA	TROY	ethanol	acetone	$\mathrm{CH}_4$	FimH	$K^{+}$	$\mathrm{H}^{\scriptscriptstyle\downarrow}$		2-propenenitrile	furfural	6-methyl-5-heptene-2-one	pentane	heptane	decane	2-methylpentane	2-ethyl-1-hexanol	propanal	pentanal	acetone	IFN- $\gamma$	CRP	cTnI	$_{ m cTnI}$	NADH	PSA		amyloid $eta$	$NO_2$	$\mathrm{NH}_3$
category	gas	bio	liquid	bio	bio		bio	gas	bio	bio	bio	gas		gas	bio	bio	liquid		gas											bio	bio		bio	liquid	bio		bio	gas	gas
mechanism category	CR	FET	FET	FET	FET		FET	FET	FET	FET	FET	FET		S	FET	FET	FET		FET											EC	FET		FET	PEC	FET		FET	S	CR
synthetic method	CVD	top-down CMOS process	top-down CMOS process	top-down CMOS process	VLS		top-down CMOS process	STA	ton-down CMOS process	top-down CMOS process	top-down CMOS process	CMOS process		MACE and sol-gel	top-down CMOS process	VLS	top-down CMOS process	(Bosch process)	VLS											VLS	top-down CMOS process		top-down CMOS process	PA-MBE	top-down CMOS process		top-down CMOS process	ST	top-down CMOS process
material	GaN	antibody-functionalized Si	MOP-functionalized Si	Al <sub>2</sub> O <sub>3</sub> -coated Si	functionalized Si		functionalized Si	InAs	antibody-functionalized Si	aptamer-functionalized Si	antibody-functionalized Si	Si EFN		TiO <sub>2</sub> -coated Si	functionalized Si NR	aptamer-functionalized Si	Al <sub>2</sub> O <sub>3</sub> -coated Si		functionalized Si											aptamer-functionalized Si	antibody-functionalized Si		antibody-functionalized Si	InGaN/GaN	antibody-functionalized Si NR		aptamer-functionalized Si	PbS	Au NP-decorated Si

Table 3. continued

material	synthetic method	mechanism	category	analyte	range (LOD)	analysis time	ref
antibody-functionalized Si	top-down CMOS process	FET	bio	cTnI CRP	10 pg/mL-1 $\mu$ g/mL (10 pg/mL) 0.1 pg/mL-100 ng/mL (0.1 pg/mL)	5 min	118
Al <sub>2</sub> O <sub>3</sub> - and GluOx- functionalized Si	VLS	FET	liquid	pH ionic strength (PBS) glucose	pH 4–8 10 μM–10 mM 0.5–1 mM	N/A	142
antibody-functionalized Au NP. CVD decorated GaN	CVD	EC	bio	$\alpha$ -fetoprotein	0.01-100 ng/mL (3 pg/mL)	120 min	125
antibody-functionalized InP	CBE	FET	bio	IBPM8-1 protein biomarker for 90–500 fM (6 fM) Chagas disease	90-500 fM (6 fM)	26 ± 3 min	110
				specific DNA sequences	15-130 fM (1 fM)	$28 \pm 2 \text{ min}$	
antibody-functionalized Si	VLS	FET	bio	CA15-3 IgG	0-535 pM (55 pM)	<5 min	134
tip-to-tip heterojunction Si	MACE	CR	gas	$NO_2$	50 ppb-16 ppm (3 ppb (n-n junction); 18 ppb (p-n junction); 150 ppb (p-p junction))	$300 \text{ s/}1000 \text{ s} (t_{\text{res}}/t_{\text{rec}} \text{ at room temp})$	133
functionalized Si	top-down CMOS process	FET	liquid	$Hg^{2+}$	1 ppt-5 ppm (1 ppt)	50 s (est. for 10 ppb)	109
antibody-functionalized Si	top-down CMOS process	FET	bio	ferritin	50 pg/mL-500 ng/mL (50 pg/mL)	20 s (est. for 50 pg/mL)	1115
Si	top-down CMOS process	FET	liquid	$\mathrm{H}^{\scriptscriptstyle{\downarrow}}$	pH 1–12	3 s (est. for pH 4)	119
functionalized Si	top-down CMOS process	FET	liquid	$ m MB^+$ $ m Na^+$	55 mV/pH 100 μM−10 mM (1 μM) 100 μM−100 mM (~60 μM)	60 s (est. for 1 μM) 40 s (est. for 100 μM)	145
Si EFN	CMOS process	FET	gas	<i>n</i> -alcohols and <i>n</i> -alkanes	N/A	N/A	124

cytokeratin-19, PBS = phosphate-buffered saline, PSA = prostate-specific antigen, EFÑ = electrostatically formed nanowire, MACE = metal-assisted chemical etching, PEC = photoelectrochemical, IFN- $\gamma$  = interferon- $\gamma$ , CRP = C-reactive protein, cTnI = cardiac troponin I, PA-MBE = plasma-assisted molecular beam epitaxy, NADH = nicotinamide dinucleotide, NP = nanoparticle, GluOx = glucose oxidase, CBE = chemical beam epitaxy, DNA = DNA, MB<sup>+</sup> = methylene blue cation, NR = nanoparticle, and N/A = not available. <sup>b</sup>Est. means values were estimated using published signal vs time data. Ego is the time it takes for the signal to reach 90% of its value at saturation. The saturation at the response time and recovery time, respectively, as defined by the reference authors.

<sup>a</sup>Abbreviations: CVD = chemical vapor deposition, CR = chemiresistor, CMOS = complementary metal-oxide-semiconductor, EC = electrochemical, FET = field-effect transistor, HT = hydrothermal,

ST = solvothermal, CYFRA21-1 = cytokeratin 19 fragment, MOP = metal-organic polyhedra, TNT = 2,4,6-trinitrotoluene, IL-2 = cytokine interleukin-2, FSP = follicle stimulating protein, KRT-19

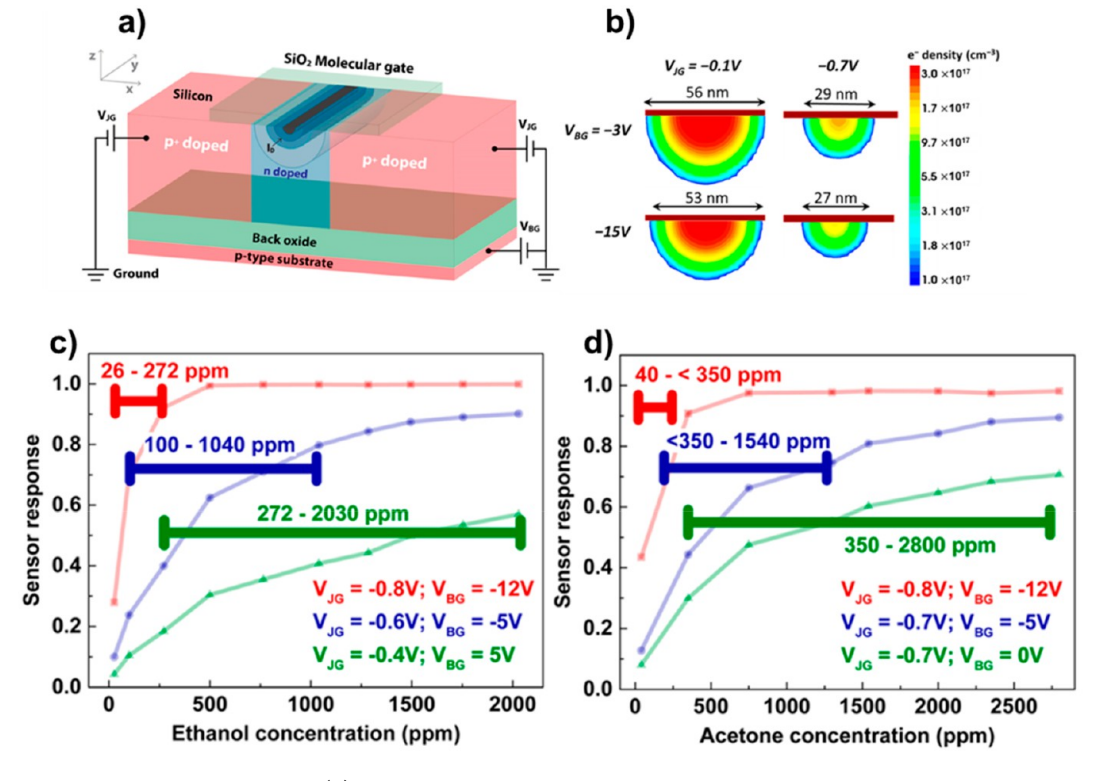


Figure 6. (a) Schematic representation of EFN. (b) Simulated cross section of the EFN electron density distribution showing the impact of varying  $V_{\rm JG}$  and  $V_{\rm BG}$  on the EFN size and shape. The corresponding effective diameter  $(D_{\rm eff})$  extracted from the fwhm of the electron density distribution of the EFN is also indicated. (c, d) Dynamic range tunability for ethanol (c) and acetone (d) achieved by varying  $V_{\rm JG}$  and  $V_{\rm BG}$ . Reproduced from Swaminathan, N.; Henning, A.; Vaknin, Y.; Shimanovich, K.; Godkin, A.; Shalev, G.; Rosenwaks, Y. Dynamic Range Enhancement Using the Electrostatically Formed Nanowire Sensor. ACS Sensors 2016, 1 (6), 688–695 (ref 123). Copyright 2016 American Chemical Society.

metals creates a synergistic effect in glucose catalysis and a resulting higher signal. This work sparked the development of several other multilayered devices for electrochemical glucose sensing, and the novelty of bimetallic NWs has applications in many future sensor designs. Jagged PtNi NWs, fabricated by Wang et al. in 2019,  $^{106}$  were used to detect caffeic acid using cyclic voltammetry; this shape exhibited a higher affinity for the acid and provided a higher stability than unmodified NWs due to the increase in Pt active sites. This unique shape provided stability, retaining 87% of their signal after 4000 cycles, with a low LOD of 0.5  $\mu\rm M$ . Future electrochemical sensors can benefit from similar innovations in the nanowire's structure

Eom et al. 100 developed a nanogap-rich gold NW sensor based on SERS for the detection of telomerase activity in cancer cells and tissues (Figure 5). The Raman signal can be dramatically amplified by introducing nanoparticles within the nanogap. Telomerase activity was investigated by analyzing the Raman signal after the elongation of the telomeric substrate (TS) primer, folding into the G-quadruplex structure, and inserting Raman dyes. This sensor platform is able to differentiate telomerase activity between normal tissue and various cancerous tissues, including breast tumors and gastric tumors, in mice.

## **■ SEMICONDUCTOR NANOWIRES**

**Introduction and Background.** A wide array of materials are being used for semiconducting NW sensors, and several different mechanisms are employed. The most common sensor material is the Si NW, which is frequently combined with a

surface modification to add a chemical or biorecognition layer to confer sensitivity and selectivity for a particular analyte molecule or class of molecules. 107–109 In addition to silicon, III–V materials, including InP, InAs, GaN, and InGaN, and IV–VI materials, including metal chalcogenides like PbS, have also been used (Table 3). 110–114 Semiconductors are attractive materials for sensors because their conductivity is inherently highly sensitive to changes in the electronic environment at the surface. Particularly for 1D nanostructures, the adsorption of charged analyte species can effectively limit the conduction pathway, the resulting change in conductance leading to high sensitivity.

Semiconductor NWs often exploit a field effect that relies on Coulombic interactions between a charged analyte species bound by receptors at the NW surface and the majority of charge carriers within the NW. Positively charged analytes, for example, reduce the hole concentration within a p-type NW, reducing the measured conductance of the nanowire, in analogy to a FET. Typically, silane linkers are employed to tether analyte-specific recognition elements to the NW surface. <sup>107,115</sup>

**Synthesis and Sensor Fabrication.** Lieber and coworkers<sup>3</sup> were the first to introduce the Si NW FET chemical sensor and biosensor in 2001. In this initial report, the Si NWs were grown using the bottom-up vapor—liquid—solid (VLS) method. In the VLS method, metal nanoparticle clusters (often Au) are used as seeds for the growth of Si nanowires. VLS is still often employed; however, in recent years, top-down CMOS compatible Si NW fabrication processes have been appearing with increasing frequency. <sup>109,1 f6–120</sup>

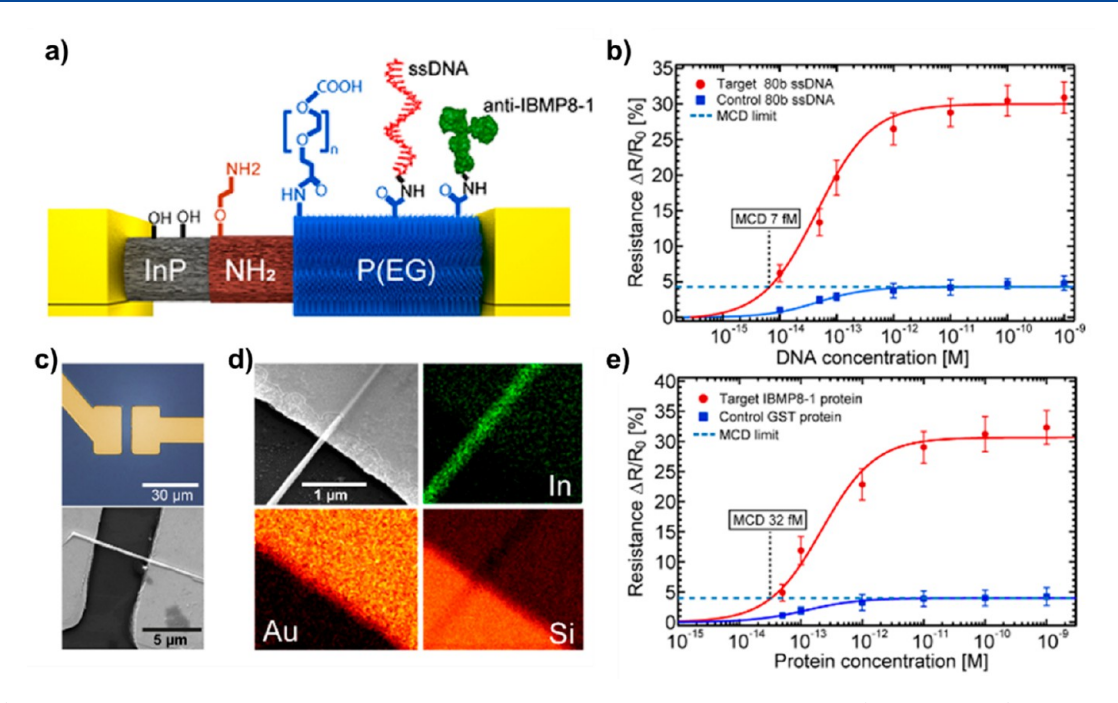


Figure 7. (a) Schematic representation of a cross-sectional single InP NW with ethanolamine and poly(ethylene glycol) functionalizations with ssDNA and anti-IBMP8-1. (c) Optical microscope image (top) of a single electrode pair and FESEM image (bottom) of an electrode pair with an aligned single InP nanowire. (d) EDS elemental mapping images of different components with an attached nanowire. (b, e) Specific *T. cruzi* recombinant antigen IBMP8-1 (red) or nonspecific glutathione S-transferase (GST) target (blue). Reproduced from Janissen, R.; Sahoo, P. K.; Santos, C. A.; Da Silva, A. M.; Von Zuben, A. A. G.; Souto, D. E. P.; Costa, A. D. T.; Celedon, P.; Zanchin, N. I. T.; Almeida, D. B.; Oliveira, D. S.; Kubota, L. T.; Cesar, C. L.; Souza, A. P. D.; Cotta, M. A. InP Nanowire Biosensor with Tailored Biofunctionalization: Ultrasensitive and Highly Selective Disease Biomarker Detection. *Nano Lett.* 2017, 17 (10), 5938–5949 (ref 110). Copyright 2017 American Chemical Society.

One of these involves patterning a silicon-on-insulator (SOI) wafer using optical or electron beam lithography. Either a dry etch by reactive-ion etching or a wet etch with tetramethylammonium hydroxide is used to form Si NW nanostructures. The NW structures are then doped, most often by ion implantation followed by annealing, and then contacts are evaporated to produce the nonfunctionalized device. 120,121

One exciting new gas sensor fabrication approach introduced by Rosenwaks and co-workers<sup>122</sup> in 2013 has been to use conventional CMOS processes to produce a multiple gated FET that can then be controllably biased to create an electrostatically formed NW,<sup>123</sup> as shown in Figure 6. The EFN is a conductive channel with a size that is adjustable by varying the bias on the surrounding gate electrodes. Varying the size of the conductive channel adjusts the interaction of the conductive channel with the molecular gate and can confer selectivity and tunable sensitivity to the EFN. The EFN has also been demonstrated to be capable of discriminating between different functional groups (alkanes and alcohols<sup>124</sup> in addition to acetone) and molecular weight species.

Other synthesis methods for semiconductor NW sensors show a great diversity in fabrication strategies. Some methods are very similar to those seen for Si NWs such as a bottom-up VLS process being used by Lynall et al. to grow InAs NWs for ethanol gas detection. 111 Chemical vapor deposition (CVD) is often employed for the production of GaN nanowires. 113,125 Molecular beam epitaxy (MBE) and chemical beam epitaxy (CBE) have been employed to produce InGaN on GaN nanowires and InP nanowires, 110 respectively. Metalassisted chemical etching (MACE), also known as MacEtch, is a top-down NW fabrication process that allows for NW arrays to be cheaply and easily fabricated. MACE works by the

enhancement of anisotropic etching at the edge of metal nanoparticles.  $^{126}\,$ 

Surface Modification of the Nanowire. Regardless of the synthetic method followed for the fabrication of the NW sensors, in most cases, the surface modification employed on the NW has been demonstrated to be essential to the sensing performance of the device. For Si NW FET sensors, the surface functionalization method first employed by Lieber and coworkers<sup>3</sup> was biotinylation of the surface for the sensing of streptavidin and antibiotin monoclonal antibodies. This relatively simple functionalization has since been supplanted by a process in which a silanization species, commonly 3aminopropyltriethoxysilane (APTES) though different functionalized silanes are sometimes used, is functionalized onto the Si NW surface. 107,115,121 This process typically takes advantage of the thin layer of native oxide at the surface and is followed by a reaction with the chemical or biorecognition moiety to graft the recognition element to the nanowire.

For biosensors, glutaraldehyde is often used after an initial aminosilane treatment to generate a covalently attached aldehyde-terminated surface layer, which is subsequently exposed to antibody solution and incubated for varying times to covalently attach antibodies. Typically, the device will then be washed with buffer and exposed to an ethanolamine solution, which serves to passivate the remaining aldehyde functional groups on the surface and prevents nonspecific adsorption of proteins to the NW surface.

A recent functionalization strategy, introduced by Gao et al. <sup>107</sup> in 2015, to overcome the problem of Debye screening is to coat the NW with a layer of poly(ethylene glycol) (PEG). Grafting the porous and protein-permeable PEG layer to the surface changes the local dielectric constant at the NW surface.

The change in dielectric constant leads to a dramatic reduction in screening in the sensing area of the FET. This approach, in combination with standard biorecognition elements, allows for a high sensitivity analyte measurement in undiluted PBS and undiluted serum. <sup>107</sup>

A related strategy was employed by Janissen et al. 110 in the modification of InP NWs for the detection of single-stranded DNA and the protein IBMP8-1 (Figure 7). In this report, the authors employed ethanolamine (EA) to directly modify the hydroxyl-terminated InP NW surface, as shown in Figure 7a. They deviated from the often-employed silane base layer because they observed more uniform surface coatings when functionalizing with EA than with APTES, as determined by fluorescence microscopy. The EA layer was used to anchor PEG with antibodies or complementary DNA.

**Transduction Mechanisms.** *FETs.* As already indicated, a transduction mechanism based upon charge gating has been demonstrated to be highly effective and versatile for a number of analyte species.  $^{120,121}$  However, some fundamental challenges must be overcome for accurate in vivo or in vitro measurements. One challenge is nonspecific signal produced by off-target adsorption of proteins and other species particularly in complex media like blood and serum.  $^{127}$  A second challenge is that the distance between a bound target molecule and the NW surface can approach, or exceed, the Debye screening length,  $\lambda_{\rm D}$ , of the solution. For a symmetric, monovalent salt:  $^{128}$ 

$$\lambda_{\rm D} = \left[ \left( \varepsilon \varepsilon_0 RT \right) / \left( 2000 F^2 C_0 \right) \right]^{1/2} \tag{2}$$

where  $\varepsilon$  is the dielectric constant,  $\varepsilon_0$  is the permittivity of free space, R is the gas constant, T is the temperature, F is the Faraday, and  $C_0$  is the electrolyte concentration (M). Equation 2 predicts  $\lambda_D$  of less than 1 Å in physiological buffer with a salt concentration of 150 mM. In such solutions, the sensitivity of a biosensor based upon a semiconducting NW is strongly degraded. 107 Commonly, the performance of these systems has been reported in dilute salt solutions with concentrations <2 mM. 129,130 To mitigate this problem, desalting is often employed in serum and blood samples, and dilute buffers with concentrations <2 mM are used when a physiological matrix is not investigated. These measures serve to greatly increase the screening length, for example, a hundredfold dilution of 160 mM phosphate buffered saline (PBS) changes the Debye screening length from 0.7 to 7.3 nm. <sup>131</sup> A problem with these desalted and dilute solutions however is they can lead to protein instability, and they add timeconsuming processing steps to the analysis. A number of innovative solutions to this problem have been demonstrated and are described below.

*Electrochemical.* While FET mode sensing is the most frequently observed transduction scheme used for semiconductor NWs, amperometric or chemiresistive electrochemical transduction schemes are also employed. Amperometric transduction can bypass some of the weaknesses of field-effect transduction as it is not as sensitive to the ionic strength of the sensing medium, relying on the electrocatalytic reaction with the analyte to generate the signal response. 112

Chemiresistors. On occasion, semiconducting NWs function as chemiresistors instead of FETs. Chemiresistive transduction is most often observed when semiconductor NWs are employed as gas sensors, where the de/adsorption of the target analyte is accompanied by a conductivity change in

the NW due to the reducing/oxidizing nature of the analyte–nanowire interaction. That is, the adsorption of the analyte species triggers a resistance change that can be correlated with the charge state of the analyte or the identity of the majority carriers in the nanowire. The direction of the resistance change in this case depends upon the particular material and the adsorbing gas. Metal oxide NWs frequently operate in this mode, but we discuss these in a separate section below.

Recent Research. FET Biosensors. As indicated above, FET sensors rely upon the electrostatic gating effect induced upon the binding of charged analyte species to a recognition layer attached to the surface of the nanowire. The amplitude of the resistance change induced by analyte binding depends upon the ionic strength of the sensing matrix due to the increased charge screening at higher ionic strength (eq 2). Several strategies have been employed to mitigate this deficiency and allow for sensing to be performed in salty solutions. These strategies are preconcentration and dilution, <sup>130</sup> surface modification with a PEG layer, <sup>107,110</sup> and the use of dissociating antibody—antigen pairs to monitor concentration after changing from the physiological solution to a dilute buffer solution.

The preconcentration and dilution strategy is slow and undesirable because it suffers from the amount of sample processing and equipment that is needed to perform the preconcentration step, and the biomarkers in the sample are often sensitive to the ionic strength of the solution. The use of the PEG layer is convenient for eliminating the dilution and preconcentration steps; however, this strategy has not yet been widely adopted.

Another strategy that has been employed by Krivitsky et al. <sup>134</sup> is to allow the antigen—antibody complexes to form in the physiological solution while monitoring the device signal and waiting for an equilibrium to be established and then rinsing away the physiological solution and using dilute buffer to sense the dissociation of the antigen—antibody complex. This strategy has been proven successful for the detection of CA15-3 IgG protein with a detection limit of 55 pM and is inherently selective due to the selectivity of the antibody. <sup>134</sup>

Krivitsky et al. 135 recently reported a 9,10-dihydroxyanthracene/9,10-anthraquinone (DHA/AQ)-decorated Si NW FET for the nonenzymatic detection of  $H_2O_2$  in biofluids. The FET relies on a hot electron injection from the Si NW to the surface-functionalized redox probe to provide the signal when H<sub>2</sub>O<sub>2</sub> is present. DHA is readily oxidized to AQ in the presence of H<sub>2</sub>O<sub>2</sub> and is easily reduced back to DHA by the Si NW FET. For a given source-drain voltage, the conductance of the NW is modulated by the amount of H2O2 in the solution. The advantage of this hot electron injection mechanism is that it works in high ionic strength solutions (155 mM PBS) and it can be readily combined with appropriate enzymes in biofluids to sense biomolecules. 135 The sensor is sensing generated H<sub>2</sub>O<sub>2</sub>, so the enzyme action must result in the production of H2O2. In this work, the authors sense glucose with the aid of glucose oxidase and demonstrate glucose sensing in unprocessed blood. 135

Gao et al.<sup>129</sup> used anti-CYFRA21-1 functionalized Si NWs to detect CYFRA21-1 in desalted serum and 0.01× PBS buffer. Band-to-band tunneling (BTBT) is the transduction mechanism suggested by the authors; this mechanism shows an enhanced signal current for the NW morphology over traditional CMOS FETs. The antibody functionalized Si NW

FET is an ambipolar device capable of sensing in the p+ and n + modes. When the CYFRA21-1 binds, a gating effect is induced and the BTBT barrier is modulated, which results in a change in the tunneling current. The detection limit was defined as 3-times the signal of the noise at 0.5 fg/mL. The change in the current varies according to the mode of operation, and the use of dual-mode operation helps to discriminate against false positives. <sup>129</sup> This device suffers from the drawbacks of Si NW FETs that do not directly address the problem of ionic strength sensitivity.

Rani et al.<sup>120</sup> used a prostate-specific antigen (PSA)-specific aptamer to sense PSA in dilute serum and buffer. The Si NWs were fabricated using nanoimprint lithography and standard photolithography processes. The high specificity of the anti-PSA aptamer allows for a detection limit as low as 1 pg/mL.<sup>120</sup> This work is another example of the high specificity and resilience to nonspecific binding that is characteristic of aptamer-modified Si NW FETs.

Tran et al.<sup>130</sup> used a typical antibody-functionalization method to decorate anticytokeratin-19 (KRT-19) antibodies onto a Si NW FET. The device showed response and processing times that suggest it could be used for the intraoperative detection of disseminated tumor cells during surgery; however, it was still necessary to employ a dilution step before analysis to ensure the Si NW FET could sense the binding event between the antibody and the KRT-19. A low detection limit of 80 fM in 0.01× PBS and relatively fast analysis time demonstrated that antibody-functionalized Si NW FETs are clinically feasible tools.<sup>130</sup>

Lee et al. <sup>136</sup> used a boronic acid-functionalized Si NW FET to detect the sialic acid moieties at the surface of a follicle stimulating hormone, a biomarker for menopause. The sialic acid moieties decorating the surface of FSH contain negative charges, which result in an electrostatic interaction with the positively charged functionalized-Si NW FET. This electrostatic interaction leads to an increase in current through the Si NW FET, and the current is shown to be selective for FSH compared to common interfering hormones. <sup>136</sup> No direct mention is made of the effect of ionic strength on the sensor performance; however, the device is shown to detect FSH with a limit of detection of 1.1 fM in 20% serum/80% PBS. <sup>136</sup>

Ma et al. <sup>127</sup> employed a dual-gated Si NR FET functionalized with anti-PSA antibodies and PEG for the detection of PSA in high ionic strength (100 mM) PBS and unprocessed human plasma. A top-down process was used in the preparation of the Si NR FET followed by the PEG functionalization process introduced by Gao et al. <sup>107</sup> The use of the PEG functionalization permitted the detection of PSA in plasma at concentrations as low as 100 pM. <sup>127</sup>

Maedler et al.<sup>121</sup> decorated Si NW FETs with antibody fragments that are antigen binding for the detection of the melanoma biomarker TROY, a member of the tumor necrosis factor receptor superfamily. By using antibody fragments with only the antigen-binding regions present, the separation between the NW surface and the binding event is minimized. In this case, it was still necessary for dilute (2 mM) PBS to be employed as the sensing medium, and the detection limit was found to be 10 ng/mL. The device showed selectivity for TROY over bovine serum albumin (BSA), and even at high concentrations of BSA, the signal from TROY could be deconvoluted from the BSA signal using a kinetic analysis. <sup>121</sup>

Mu et al.<sup>137</sup> reported a novel strategy for the detection of ultralow concentrations of cytokine interleukin-2 (IL-2) using

Al<sub>2</sub>O<sub>3</sub>-coated Si NW FET sensors. The strategy uses the Si NW FET to observe pH changes occurring due to DNA amplification during polymerase chain reaction (PCR) and immuno-PCR. During PCR, protons are released with the attachment of each nucleotide to each nucleic acid strand. The pH changes allow for the determination of the initial protein concentration. In this work, the Si NW FET are only acting as pH sensors; PCR and DNA amplification is performed, and then, the resulting samples are tested for their pH. This strategy offers very low detection limits with the trade-off being the processing time needed for increasing the number of cycles of DNA amplification. With 55 cycles of amplification, a signal of 30 aM IL-2 was clearly detected, and an increase in the number of amplification cycles would allow for this detection limit to be further extended.<sup>137</sup>

Wipf et al. 138 used functionalized Au-coated Si NRs to monitor the kinetics of FimH-substrate binding. FimH is a protein associated with urinary tract infections that binds to carbohydrates. In this work, well-established gold surface-modification chemistry was used to prepare a mannose-functionalized gold-on-silicon NR surface that was capable of binding FimH in solution. The reduced pH response of gold relative to the native oxide surface of the silicon NR was found to provide a greater signal response for FimH binding. This effect is suggested to result from reduced interference due to protons on the gold-coated surface. 138

Li et al.<sup>139</sup> have recently reported a kinetic analysis of antibody-functionalized Si FET NWs used for the detection of cardiac reactive protein (CRP) and cardiac troponin I (CTnI). The measurements were performed in relatively dilute (10 mM) PBS at pH 7.4 and 8.4. For low concentrations, the device signal was observed to take a long time to stabilize for both proteins. Using a kinetic analysis allows the concentration to be determined before the steady state is reached by determining the reaction kinetic parameters. One key finding was that the reaction parameters are about 5× faster for CRP than for cTnI, suggesting that CRP may be a better target than cTnI when the measurement time is limited.<sup>139</sup>

Kutovyi et al. <sup>118</sup> have recently described a top-down process for the production of Si NW FETs, which were functionalized with anti-CRP antibodies and a dibenzocyclooctyne (DBCO)-linked cTnI aptamer. No mention is made of what steps were taken to combat Debye screening; however, the measurements were carried out in undiluted PBS. The authors investigated two NW geometries: one that was 100 nm wide and 200 nm long and another that was 100 nm wide and 1  $\mu$ m long. The authors observed that the concentration of signal saturation was 3 orders of magnitude greater for the long NW than the short nanowire, suggesting that the detection range can be tuned by adjusting the size of the nanowires. <sup>118</sup>

Kim et al. <sup>140</sup> prepared honeycomb Si NW FETs using a top-down process and functionalized them with cTnI monoclonal antibodies using the standard aminosilane-based protocol. The effect of sensing medium salt concentration on sensor performance was investigated, and the best results were obtained for dilute 0.01× PBS; however, the sensor still showed sensor responses at 0.1× PBS. There was no signal response observed for undiluted PBS, which is typical for devices produced before strategies to address the problem of screening were developed. A low limit of detection of 5 pg/mL and excellent selectivity provide other examples of the strength of antibody-modified Si NWs. <sup>140</sup>

**Analytical Chemistry** Review pubs.acs.org/ac

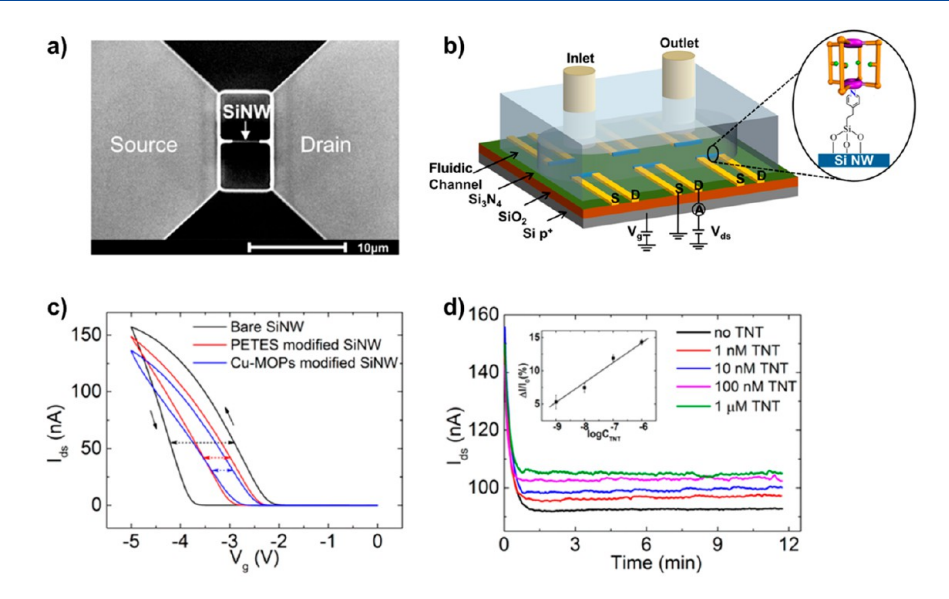


Figure 8. (a) SEM image of Si NW (horizontal line in the center). (b) Schematic representation of the SiNW chip, including a zoom-in schematic illustration of the SiNW surface modified by a pyridyl-silane and subsequently a Cu-MOP (not to scale). (c) I-V curves from a bare SiNW (black curve), a PETES-modified SiNW (red curve), and a Cu-MOP-modified SiNW (blue curve). (d) Current time traces (raw data) from a Cu-MOPmodified chip while flowing through ethanol solutions with different TNT concentrations; the inset shows the relative steady-state current change ( $\Delta I/I_0$ ) versus TNT concentration. Reproduced from Cao, A.; Zhu, W.; Shang, J.; Klootwijk, J. H.; Sudhölter, E. J. R.; Huskens, J.; De Smet, L. C. P. M. Metal-Organic Polyhedra-Coated Si Nanowires for the Sensitive Detection of Trace Explosives. Nano Lett. 2017, 17 (1), 1-7 (ref 108). Copyright 2017 American Chemical Society.

Yen et al. 115 prepared an antiferritin decorated polycrystalline horn-like Si NW FET sensor using a top-down process followed by a typical antibody modification scheme. Dilute PBS was used as the sensing medium to maximize the Debye length. An oxide-nitride-oxide (ONO) stacked sensing platform was deposited on the Si NW FET using a lowpressure CVD method to produce a sandwich structure with silicon nitride between layers of tetra-ethylorthosilicate. This ONO sensing platform was shown to have favorable capacitive coupling between the bottom gate and the oxide layer to which a super-Nernstian pH response of 133.47 mV/pH is attributed. 115

Vu et al. 141 recently demonstrated the utility of DNA aptamers for sensing with Si NWs in high ionic strength media without the use of a PEG-functionalization layer. In this report, R18, an aptamer sensitive to IgG, is decorated onto direct (6× histidine) and sandwich (amyloid  $\beta$  1–42) immunoassays and a dramatic signal enhancement is observed in high ionic strength buffer. This signal enhancement is attributed to the small size and highly charged nature of the aptamer, which allows it to fold closely to the FET surface. 141

Kutovyi et al. 116 recently described an aptamer-modified two-layer Si NW FET for the detection of amyloid  $\beta$ -40 (A $\beta$ -40). The sensing medium was undiluted PBS. The sensing mechanism is based on the single-trap mechanism, in which noise caused by a single trap in the two-layer random telegraph signal is highly sensitive to the surface potential of the FET and offers a signal enhancement over the standard molecular gating transduction mechanism. A single-stranded DNA aptamer specific to A $\beta$ -40 was decorated on the NW surface, and when the aptamer folds, the highly charged aptamer is brought closer to the sensing area. A detection limit as low as 0.1 pg/mL was observed.116

Schütt et al. 142 used a bottom-up VLS process to produce an array of Si NW FETs contacted by interdigitated electrodes that were used for the investigation of individual microdroplets

from emulsions. The standard FET detection scheme is employed. This novel device demonstrates that NWs confer the ability to probe individual microdroplets and determine chemical parameters like ionic strength, pH, or in the case of the enzymatically modified NWs, glucose concentration. The sensor can discriminate between oils used in microemulsions and the aqueous components, and the ideal microdroplet volume was identified. Too small of a droplet volume leads to interference from the nonaqueous phase and prevents accurate sensing. This work is exciting because it shows the potential of NW-based devices for large-scale sampling of microdroplets with individual sensor responses for each microdroplet.1

FET Chemical Sensors. For chemical sensors, strategies similar to those used for biosensors have been employed; however, in these cases, rather than using an antibody as the recognition element, chemical species that selectively bind or react with the target analyte are instead used.

Cao et al. 108 have reported the use of Cu metal-organic polyhedra (MOP), as seen in Figure 8, in ethanolic solutions for the detection of trinitrotoluene (TNT). In this case, a Si NW was modified by the Cu MOP, which is capable of selectively binding TNT. The size of the MOP ensures a 1:1 stoichiometry between the MOP and TNT. When the TNT is bound by the Cu MOP, the nitro-groups on the TNT withdraw electron density from the Cu and amino-linkers in the MOP. This change in electron density is sensed by the molecular gate of the FET.

Similarly Jin et al. 109 employed Si NWs functionalized with (3-mercaptopropyl) trimethoxysilane (MPTMS) for the detection of mercuric ion. The MPTMS functionalization is decorated with thiol groups which, in the presence of Hg<sup>2+</sup>, bind the metal ion and release a proton that is then sensed with the FET. The MPTMS was shown to have a strong preference for Hg<sup>2+</sup> over many other divalent cations. <sup>109</sup>
Lynall et al. <sup>111</sup> reported the bottom-up VLS synthesis of

InAs NWs for the detection of ethanol gas. A dramatic

sensitivity enhancement was observed at ultralow ethanol concentrations. This was attributed to the scattering contributions from spatial fluctuations in dipole potentials along the length of the NWs, which are enhanced due to the confinement of carriers to one spatial dimension and the resulting weakened screening effects. The reduction of the NW carrier density via the gate electrode was shown to increase the peak sensor responsivity and shift the dynamic range to lower concentrations. A detection limit of 10 ppb ethanol was achieved. <sup>111</sup>

Shehada et al. 143 reported a VLS process followed by silane functionalization to produce Si NW FET sensors for the detection of volatile organic compound biomarkers for lung cancer, gastric cancer, asthma, and chronic obstructive pulmonary disease. Artificial neural network analysis and discriminant function analysis were applied to breath samples from patients who were known to have the diseases, and "breathprints" were constructed for each disease. These sensors allow for the fast diagnosis of patients with relatively high accuracy (>80%). 143

pH Sensing. One common application for Si NW FET sensors is in pH sensing. The native oxide layer on the Si NW is sensitive to the pH of a contacting solution due to the reversible proton equilibria involving surface Si–O–H. A common strategy for biosensors is to take advantage of proton-coupled reactions to indirectly sense a target analyte. In these cases, protons are consumed or released because of the analyte–receptor interaction, and this change in pH is used to generate a signal response. Many groups have pursued the goal of achieving a perfect Nernstian response in the threshold voltage,  $V_{\rm th}$ , with the change in pH, and a diversity of strategies have been employed in Si NW synthesis and surface modification to achieve this goal.

Zhou et al. <sup>119</sup> used a CMOS processing compatible sidewall mask technology to produce Si NWs, which showed a  $V_{\rm th}$  of 55 mV/decade for solutions from pH 1 to 12. The sidewall mask technology to produce the Si NWs employs a simple low-cost method to produce a hard mask for Si NW etching. Briefly, conformal thin films were coated onto a thin mesa, and subsequently, the planar portions of the thin films were anisotropically etched away, leaving behind the standalone sidewall hard masks. The sidewall thicknesses are tunable by changing the thickness of the thin films without the need for additional lithographic processing requiring expensive lithography facilities. <sup>119</sup>

Kwon et al. <sup>144</sup> used a top-down procedure to produce a gate-all-around Si NW FET pH sensor. Bulk silicon was used as the substrate for Si NWs using a dry etching process called the Bosch process. The authors observed the most stable sensing response when the capacitance of the sensing layer was matched to the capacitance of the transducer. The fabricated extended-gate devices showed a  $V_{\rm th}$  response of 50.9 mV/pH in the range from pH 3 to 11, which is superior to the performance of commercially available planar FET transducers with the same sensing area. <sup>144</sup>

Chen et al. 145 prepared a NW FET for the sensing of Na<sup>+</sup> and the methylene blue cation (MB<sup>+</sup>). In this work, mixed-matrix membranes incorporating metal—organic supercontainer (MOSC) ionophores for Na<sup>+</sup> and MB<sup>+</sup> are decorated on Si NWs, and a multiplexer is employed for the analysis of river water. This work is novel because it demonstrates the simultaneous and selective detection of molecular ions and simple metal ions in a single solution. 145

Anand et al.  $^{146}$  used a bottom-up VLS process to fabricate multiple-parallel-connected (MPC) Si NW-FETs functionalized with DNA-aptamer for the detection of  $K^{+}$  in cortical neuron efflux. In MPC Si NW-FETs, many Si NWs are trapped between the source and drain electrodes, leading to a cumulative response with a resulting enhancement in signal. The authors functionalized the MPC Si NWs with a mixture of 3-aminopropyltrimethoxysilane (APTMS) and propyltrimethoxysilane (PTMS) in a 1:5 ratio to ensure that the density of aptamers on the surface would leave enough room for the aptamer to fold upon binding  $K^{+}$ . The aptamer-functionalized devices were able to monitor the release of  $K^{+}$  from living cortical neurons, and a detection limit of 1 nM  $K^{+}$  was determined.  $^{146}$ 

Chemiresistors. In chemiresistive semiconductor NWs, two processes can lead to a resistance change. In the first of these, an adsorbing molecule displaces an electron-withdrawing  ${\rm O_2}^-{}_{\rm ad}$ . Desorption of  ${\rm O_2}^-{}_{\rm ad}$  is accompanied by the ejection of the spare electron back into the semiconductor. A second possibility is that the adsorption of a reducing (or oxidizing) gas directly results in the injection of electrons (or withdrawal of electrons) into (away from) the semiconductor. <sup>113,117</sup> In the last five years, there has been interest in the detection of hazardous gases using semiconductor nanowire sensors, particularly in the detection of  ${\rm NO}_2$ .

Zhao et al. 113 fabricated GaN NWs using metal organic chemical vapor deposition (MOCVD) of trimethylgallium (TMGa) onto a GaN seed layer-coated sapphire substrate with the assistance of a NiAu catalyst positioned at either side of the 40-80 μm trench. A SiO<sub>2</sub> blocking layer deposited by plasmaenhanced CVD was employed in the trench to prevent the formation of parasitic bridging GaN, which would reduce the sensitivity of the device. Two related mechanisms are proposed for these NW sensors in the dark and under UV illumination. The dark mechanism is due to a change in the NW resistivity caused by NO2 adsorption onto the NW surface, which increases the depletion region already present due to adsorbed O<sub>2</sub>. In this case, the adsorbed O<sub>2</sub> - blocks much of the NW surface and attenuates and slows the sensor response. Under UV illumination, photon generated holes move to the NW surface and lead to the desorption of adsorbed O<sub>2</sub>, which frees up active sites for NO<sub>2</sub> adsorption. A detection limit of 0.5 ppb was observed under UV illumination, and a detection limit of 4.5 ppb was observed in the dark.<sup>113</sup>

Kan et al. 114 described a procedure to produce arrays of PbS NWs on paper using a solvothermal method to produce a colloidal dispersion, which is subsequently spray coated onto paper. The resulting sensors were found to show greater sensing performance and mechanical durability than colloidal quantum dot PbS, with each type of PbS sensor subjected to bending before having its sensing performance tested. This enhanced response was attributed to the superior mechanical properties of NWs resulting in the NWs better being able to accommodate the repeated stress. The sensors were used to sense NO2, and the mechanism is due to the conductivity change accompanying the competitive adsorption of NO2 in the presence of O2. The PbS NWs are p-type, so the replacement of adsorbed O2 with the stronger electronwithdrawing NO<sub>2</sub> leads to an increase in the p-doping and a decrease in the resistance of wires. The limit of detection was determined to be 36 ppb NO<sub>2</sub>. 114

Lin et al. 133 reported a process for the production of tip-tip structures of doped Si NWs for the detection of NO<sub>2</sub>. The

Table 4. Metal Oxide NW/NF/NR-Based Sensors<sup>a</sup>

material	synthetic method	mechanism	category	analyte	range and $(LOD)^b$	resp/rec time <sup>c</sup>	ref
$SnO_2$	CVD	CR	gas	Cl <sub>2</sub>	50-400 ppb (0.048 ppb)	15 s/25 s at 5 ppm	171
Pd/ZnO/ZnS	HT	CR	gas	$H_2S$	2-10 ppm	061 s/62 s at 10 ppm	254
$\begin{array}{c} \text{CuO/Cu}_2\text{O/} \\ \text{Ag} \end{array}$	nanolithographic	CR	gas	acetone	0.125-1000 ppm (125 ppb)	122 s/37 s at 1000 ppm	188
Pt/ZnO	VLS	CR	gas	toluene	0.1-50 ppm (0.3 ppb)	N/A	190
Pt/WO <sub>3</sub>	ES	CR	gas	$H_2S$	0.1-5 ppm (100 ppb)	N/A	189
Pt/PdO	LPNE	CR	gas	$H_2$	10-100 ppm and 0.1-0.2% (10 ppm)	166 s at 0.1%	91
SnO/ZnO	thermal evaporation	CR	gas	NO <sub>2</sub>	50-500 ppb (50 ppb)	110 s/287 s at 500 ppb	195
WO <sub>3</sub> /CuO	top-down lithographic approaches	CR	gas	ethanol	0.1-1000 ppm (0.094 ppb)	1 s/140 s at 1000 ppm	185
$NiO/Co_3O_4$	E-beam evaporator	CR	gas	$C_6H_6$	1-5 ppm (13.91 ppb)	N/A	194
Co <sub>3</sub> O <sub>4</sub> @ NiMoO <sub>4</sub>	HT	CR	gas	xylene	1-500 ppm (424 ppb)	13 s/25 s at 1 ppm	192
SnO <sub>2</sub> /ZnO	HT	CR	gas	N-butylamine	1-200 ppm	less than 30 s/55 s	191
Si/WO <sub>3</sub>	metal-assisted chemical etching	CR	gas	NO <sub>2</sub>	0.25-5 ppm	N/A	255
SnO <sub>2</sub> /ZnO	HT	CR	gas	ethanol	1-100 ppm (1 ppm)	3 s/38 s at 100 ppm	256
CeO <sub>2</sub> /WO <sub>3</sub>	HT	CR	gas	acetone	0.5-2.5 ppm (500 ppb)	34 s/68 s at 2.5 ppm	184
SnO <sub>2</sub> /NiO	VLS deposition	CR	gas	$H_2$	1-500 ppm (1 ppm)	2 s/11 s at 500 ppm	187
$GF-nTiO_2$	ES	PV and EIS	bio	EGFR2	1.0 fM $-0.1 \mu M$ (1.0 fM)	N/A	166
IrOx	ES	CV	bio	AFP	0.05-150 ng/mL (20 pg/mL)	N/A	217
MWCNT- ZnO	ES	CV	bio	carcinoma-125 antigen	0.001 UmL <sup>-1</sup> -1 kUmL <sup>-1</sup> (0.00113 UmL <sup>-1</sup> )	N/A	205
IrO <sub>2</sub> @NiO	ES	AM	bio	glucose	$0.5 \ \mu\text{M} - 2.5 \ \text{mM} \ (0.31 \ \mu\text{M})$	3.3 s	200
$\frac{\alpha\text{-MnO}_2}{\text{Co}_3\text{O}_4}$	HT	CV and AM	bio	glucose	60 μM-7 mM (0.03 μM)	less than 5 s	156
$Au-NiO_{1-x}$	ES	AM	bio	glucose	0.005-15 mM (0.001 mM)	N/A	84
ZnCo <sub>2</sub> O <sub>4</sub> / Co <sub>3</sub> O <sub>4</sub>	HT	AM	bio	$H_2O_2$	0.010-750 μM (1 nM)	4 s	197
Au-Cu@ CuxO	electroless deposition	AM	bio	l-Cys	1.25 μM−1.94 mM (1.25 μM)	10 s	198
$RuO_2$ $-TiO_2$	ES	AM	bio	L-AA	$10-1500 \ \mu M \ (1.8 \ \mu M)$	$4.5 \pm 4.2 \text{ s}$	219
Ag/CuO	cation-exchange reaction	CV	bio	DA	0.04-10 μM (7.0 nM)	N/A	206
a-MnO <sub>2</sub>	low-temperature sol—gel method	CV	bio	potassium ion	$2-90 \ \mu M \ (0.05 \ \mu M)$	N/A	220
$In_2O_3$	SMP	FET	bio	cTnI CK-MB	1-300 pg/mL (1 pg/mL) 0.1-3 ng/mL (0.1 ng/mL)	45 min	210
				BNP	10-90 pg/mL (10 pg/mL)		
$In_2O_3$	SMP	FET	bio	glucose	10 nM-1 mM (10 nM)	N/A	211
$In_2O_3$	SMP	FET	bio	serotonin	10 fM-1 μM (10 fM)	5 s	221
				DA	10 fM-1 μM (10 fM)		
Yb-doped $In_2O_3$	ES	FET	bio	ethanol	1-50 ppm (1 ppm)	N/A	165
NiO-ZnO	radio frequency magnetron sputtering	FET	bio	glucose	$0.001-10 \text{ mM} (26 \mu\text{M})$	N/A	257
$Al/\beta$ - $Bi_2O_3$	ES	FET	bio	serotonin	10 nM-1 μM (0.29 nM)	0.8 s	213
ZnO	sputter-deposited	FET	bio	phosphate	0.1-7.0 mM (50 nM)	N/A	258
	* *	_					

"Abbreviations: MWCNT = multiwall carbon nanotube, CVD = chemical vapor deposition, HT = hydrothermal synthesis, ST = solvothermal synthesis, VLS = vapor—liquid—solid, ES = electrospinning, LPNE = lithographically patterned nanowire electrodeposition, SMP = shadow mask patterning, CR = chemiresistive, PV = pulse voltammetry, EIS = electrochemical impedance spectroscopy, CV = cyclic voltammetry, AM = amperometry, FET = field-effect transistor, EGFR2 = epidermal growth factor receptor 2, AFP =  $\alpha$ -fetoprotein, cTnI = cardiac troponin I, CK-MB = creatine kinase MB, and BNP = B-type natriuretic peptide. <sup>b</sup>Reported detection range and limit of detection (LOD). <sup>c</sup>Reported response time/ recovery time (resp/rec). If only one number is given, it is the response time. "N/A" if information was not reported.

heterostructures were produced using the MACE process followed by a welding step in which two vertically aligned NW samples were pressed together while a current was applied. The sensing mechanism of the tip—tip device is dependent on the type of structure that is formed. For p—p homostructures, the adsorption of  $NO_2$  gas leads to an increase in the p-doping

and an accompanying increase in conductivity through the device. For n-n homostructures, the adsorption of  $NO_2$  leads to a depletion of charge carriers and an increase in device resistance. In p-n heterostructures, the effect of the adsorption of  $NO_2$  is dependent on the bias voltage applied to the heterojunction. The lowest limit of detection was observed for

the n-n tip-tip Si NW device with a limit of detection of 3 ppb  $NO_2$ . <sup>133</sup>

Si NWs have also been used for the detection of reducing gases. Kim et al. 117 recently described a top-down process for the production of Au nanoparticle-decorated Si NWs for the sensing of gas-phase NH<sub>3</sub>. Two NWs were compared. Both NWs were given an initial treatment in dilute hydrofluoric acid, but one of the NWs was subsequently immersed into a solution containing gold ions, resulting in the deposition of gold nanoparticles on the Si NW surface. The Au-decorated Si NW was found to have greater stability and reliability than the Si NW with its native oxide, which was attributed to the enhanced electron transfer from the Au to the Si NW during the adsorption of NH<sub>3</sub> gas. This adsorption leads to an increase in conductivity of the Au-decorated Si NW device, and a detection limit of 0.14 ppm was determined. 117

Liu et al. 126 fabricated TiO2-coated Si NW heterostructures for the gas-phase detection of CH<sub>4</sub>. The Si NW cores were produced by MACE using silver nanoparticles, and then, a TiO<sub>2</sub> shell was added using a sol gel process. There are two related mechanisms that the CH<sub>4</sub> sensing can have depending on the doping of the Si NW core. In each case, the authors suggest that room temperature sensing of CH4 is most likely occurring through a transient complex formed between adsorbed O2-ad and CH4. When this complex forms, it readily decomposes to form O2 gas and CH4 gas with an accompanying release of an electron into the TiO2. The TiO<sub>2</sub> shells are n-type, so for p-type Si NWs, the signal is a result of the released electrons increasing the thickness of the depletion layer and decreasing the conductivity of the device. For the n-type Si NWs, the release of the electron accompanying the desorption of the  $O_2^-$  complex results in an increase in conductivity for the device. The limit of detection was determined to be 20 ppm  ${\rm CH_4}$ .  $^{126}$ 

Electrochemical. Amperometric transduction carried out in a potentiostatic mode is frequently used for solution-phase measurements because capacitive noise, caused by a time-varying voltage, is eliminated, allowing more sensitive detection of current-based signal from analytes. Recently, there have been reports of the amperometric signal suppression that occurs when active sites on the sensor surface are blocked due to folding of a surface-decorated recognition layer, often an aptamer or antibody. Additionally, there is a photo-amperometric transduction mechanism that relies on the photocurrent generated when a photocatalyst is illuminated in the presence of substrate.

Riedel et al. 112 described a plasma-assisted MBE process for the fabrication of InGaN/GaN NWs for the photoamperometric detection of NADH. The photocurrent is a consequence of the photo-oxidation of NADH to NAD+ at the electrode surface, and the wavelength of the light used for excitation was carefully selected to avoid the decomposition of other biomolecules. An enhancement of the photoamperometric signal was observed for the InGaN/GaN NWs relative to bare GaN NWs. A dynamic range from 5  $\mu$ M to 10 mM was determined for NADH detection. 112

Liu et al. <sup>132</sup> reported a procedure for the production of aptamer-functionalized gold-coated Si NWs produced using the VLS method for the detection of interferon- $\gamma$  (IFN- $\gamma$ ). The gold layer was applied to the Si NWs to enable the attachment of aptamers using gold—thiol chemistry. The authors employed an aptamer that has been engineered to contain redox-active moieties, which are suppressed when the aptamer binds to the

IFN- $\gamma$ . The degree of current suppression is used to determine the concentration of the IFN- $\gamma$ . A NW decorated electrode shows higher signal suppression than that observed for a planar electrode. No other morphology of the nanostructure was investigated, so it is unclear how integral the NW morphology is to the observed signal enhancement beyond typical surface area enhancement. A detection limit of 0.14 ng/mL IFN- $\gamma$  was achieved. <sup>132</sup>

A related strategy was employed by Liu et al. 125 in the production of antibody-functionalized Au nanoparticle-decorated GaN NWs for the detection of  $\alpha$ -fetoprotein (AFP). A CVD method was employed to produce GaN NWs, which were subsequently oxidized with piranha solution to generate a hydroxyl-terminated surface. The NWs were then coated with poly(dopamine) (PDA) by dip-coating and then immersed into a colloidal gold solution. The anti-AFP antibodies were then decorated onto the GaN NWs to produce the functionalized sensing device. The signal is the change in the current at the peak potential during differential pulse voltammetry for the NW. As the target protein concentration increases, the binding event leads to less electroactive surface area for the charge transfer to occur, which leads to an attenuation of the current, which can alternatively be interpreted as an increase in the charge transfer resistance accompanying protein binding. The signal for transduction is the  $I/I_0$  where  $I_0$  is the current with no analyte present. A limit of detection of 3 pg/mL AFP was determined. 12.

The future of semiconductor NW FET sensors is exciting, with the introduction of new methods for the sensitive detection of important biomarkers in high ionic strength matrices like human serum, plasma, and whole blood. The use of a PEG functionalization for the sensing of analytes in unprocessed biofluids should allow the development of many new high-sensitivity and high-specificity biosensors. One direction the field is moving in is the development of point-of-care biosensors, which eliminate the need for long wait times and provide patients with timely results.

#### ■ METAL OXIDES

Introduction and Background. Metal oxide  $(MO_x)$  nanostructures are desirable materials for sensing applications because of their low-cost, facile synthesis methods, scalability, and robustness. Researchers have reported several NW synthetic routes ranging from simple hydrothermal, solvothermal, and vapor deposition reactions to more involved lithographic and electrochemical-based approaches (Table 4). For the purposes of this Review, we will highlight synthesis/fabrication routes that produced unique morphological or compositional NW characteristics.

**Synthesis and Fabrication Methods.** Hydrothermal and Solvothermal Methods. Ren et al. 147 took advantage of polymer self-assembly to create unique Si-doped multilayer-crossed tungsten oxide NW 3D arrays (MC-WO<sub>3</sub>-NWAs). Briefly, a solution of dissolved poly(ethylene oxide)-block-polystyrene (PEO-b-PS copolymers) in tetrahydrofuran (THF) was mixed with hydrated silicotungstic acid (H<sub>4</sub>SiW) in THF to form a colloidal solution. This colloidal solution was composed of spherical micelles of THF-swelled PS cores with H<sub>4</sub>SiW-PEO shells. After calcining in N<sub>2</sub> and air, a multilayer assembly was achieved where the NWs were ordered in one direction in each layer but also orthogonally crossed in adjacent layers. This led to a favorable ordered and interweaved lamellar array of Si-doped WO<sub>3</sub> nanowires. The

extension of this method to the synthesis of other  $MO_x$  NW arrays, including Si-doped  $MoO_3$ , P-doped  $WO_3$ , and P-doped  $MoO_3$  was also demonstrated in this work. 147

Yao et al. <sup>148</sup> were one of the early groups to coat MO<sub>x</sub> NWs with metal—organic frameworks (MOFs) and use them for sensing applications. They synthesized zinc oxide@zeolitic imidazolate framework CoZn core—shell NWs (ZnO@ZIF-CoZn) via a modified hydrothermal route. This work demonstrated a streamlined process for producing ZnO@ZIF-COZn NW arrays. These systems combined a ZnO NW with intrinsically high sensitivity to volatile organic compounds (VOCs) with additional selectivity imparted by the ZIF-CoZn. Drobek et al. <sup>149</sup> used a similar approach except that ZIF-8 was used as the shell for ZnO core nanowires. The coordination between the surface Zn<sup>2+</sup> of the oxide and the imidazolium anions in solution converted the surface layer of the ZnO into ZIF-8.

 $MO_x$  NW sensors exploiting other metal oxides have also been described including tin oxide (SnO\_2) nanowires,  $^{150}$  ZnO nanowires,  $^{151-154}$  cerium oxide nanodot-decorated WO\_3 nanowires,  $^{155}$  cobalt oxide nanoparticle decorated manganese oxide (Co\_3O\_4/MnO\_2) nanowires,  $^{156}$  and microstructured needle-like zinc cobalt oxide (ZnCo\_2O\_4) nanowires.  $^{157}$ 

Electrochemical Methods. Kim et al. 158 synthesized bimetallic PtM nanoparticles (where M = Pd, Rh, and Ni) dispersed on WO<sub>3</sub> nanofibers via an electrospinning method. The notable features of this work are the bimetal ion encapsulation using protein cages leading to facile bireduction of the metallic nanoparticles. The ability to achieve narrow size distributions is also noteworthy as it demonstrates a high degree of synthetic control over these decorated nanofibers. In previous work from the same group, Choi et al. 159 produced single metallic apoferritin Pd-encapsulated nanoparticles loaded on macroporous WO<sub>3</sub> nanotubes. A similar process was employed by Jeong et al. 160 for the creation of multichannel PtO<sub>2</sub>-loaded SnO<sub>2</sub> nanofibers.

Katwal et al. 161 demonstrated that ZnO nanotube—nanowire hybrid structures can be electrochemically fabricated using environmentally benign reagents. These structures were obtained by anodization of a Zn foil substrate at room temperature. The precise morphology obtained by this process was time dependent, progressing from needles to urchin-like needles, to nanorods, and then to nanotubes. Here, it is reported that the nanotubes are created through simultaneous growth and etching ultimately leading to an overall amorphous, hexagonal structure. These were annealed in O<sub>2</sub> producing wurtzite-phase ZnO nanostructures.

Penner and co-workers<sup>91</sup> created Pt-functionalized palladium oxide (PdO) NWs using lithographically patterned NW electrodeposition (LPNE). Lithographically patterned and etched Ni NW arrays acted as the working electrode to electrodeposit metallic Pd on its edges. Further chemical treatments removed the remaining photoresist and Ni leaving the Pd NW array behind. They were calcined to create PdO nanowires. Finally, these were functionalized with Pt by submerging them in an ethylene glycol and potassium hexachoroplatinate(IV) (K<sub>2</sub>PtCl<sub>6</sub>) solution. This work highlighted a method for controllably and reproducibly creating Pt-functionalized PdO NWs using LPNE.

Wang et al.  $^{162}$  systematically combined electrospinning with chemical bath deposition to create unique iridium oxide (IrO<sub>2</sub>) core NWs decorated with nickel oxide (NiO) nanoflakes. While the techniques themselves and their implementation

were straightforward, the morphology of the  $IrO_2@NiO$  core—shell NWs were unique enough to highlight.

Steinhauer et al.  $^{163}$  created copper oxide (CuO) NWs on microhot plate devices using thermal oxidation. Cu microstructures were thermally deposited on the microhot plates with  $\sim$ 2  $\mu$ m gaps between them and were biased with a constant voltage in air. They observed discrete current increases that they attributed to individual CuO NWs connecting the oxidized microstructures. The significance of this work is the high controllability over the number of individual CuO NWs bridging the microstructures that can be made during the fabrication process. It provides a framework for an emerging class of single NW sensors with controlled dimensionality and morphology.

Other  $MO_x$  NWs were created through these electrochemical methods such as strontium doped indium oxide (Sr-In<sub>2</sub>O<sub>3</sub>), <sup>164</sup> ytterbium-doped In<sub>2</sub>O<sub>3</sub> (Yb-In<sub>2</sub>O<sub>3</sub>), <sup>165</sup> carbondoped titanium oxide (C-TiO<sub>2</sub>) nanofibers, <sup>166</sup> mesoporous Pt-functionalized tin oxide SnO<sub>2</sub> nanotubes, <sup>167</sup> ZnO nanofibers, <sup>168</sup> and Pt-functionalized macroporous WO<sub>3</sub> nanofibers. <sup>169</sup>

Chemical Vapor Deposition. Hung et al. <sup>170</sup> used a simple chemical vapor deposition setup to create morphologically unique biaxial SnO–ZnO heterostructured nanowires. The heterostructures were spherically capped nanowires. They used a simple tube furnace setup with Sn and Zn powder sources in elevated temperatures but depressed pressures. They described the biaxial growth to occur through the reaction of Sn and Zn vapors leading to a Sn–Zn alloy on the glass substrate. The Zn is oxidized to ZnO when the alloyed droplets are oversaturated and the ZnO NW begins to grow, pushing the alloyed droplet upward away from the glass. SnO nuclei decorate along a preferred orientation of the growing ZnO and begin to epitaxially grow alongside it. This work highlights MO<sub>x</sub> alloyed epitaxial growth leading to unique spherically capped nanowires.

Van Dang et al.<sup>171</sup> showed that ZnO, SnO<sub>2</sub>, and WO<sub>3</sub> NWs could be synthesized with on-chip growth using chemical vapor deposition. Catalytic islands deposited on the silicon substrate (Au for ZnO and SnO<sub>2</sub> NW sensors while W was used for WO<sub>3</sub>). The respective Zn, Sn, and W precursors were loaded onto an alumina boat and then heated in a quartz tube furnace flown with Ar and O<sub>2</sub>. The notable aspect of this work is how varying varying MO<sub>x</sub> NWs are fabricated simply by swapping for a different transition metal precursor. Zhou et al.<sup>172</sup> made single ZnO NW sensors based on this method, but to achieve the single NW component, they dispersed the NW arrays in ethanol and drop-casted them onto their substrate. Similar chemical vapor deposition procedures were used to fabricate other SnO<sub>2</sub> nanowires<sup>173</sup> and Au-functionalized ZnO nanowires.<sup>174</sup>

Cao et al.  $^{175}$  created a DNA-ZnO NW sensor via a vapor—liquid—solid method. The DNA-ZnO NWs were prepared by creating the ZnO NW template. First, ZnO nanopowder and activated carbon powder were mixed thoroughly and placed on an alumina boat in the center of a tube furnace. A silicon (Si) substrate was positioned directly above with a 5 nm catalytic Au layer. The powder mixture was heated at 960 °C for 1 h with an Ar/O<sub>2</sub> carrier gas. What sets apart this work is that a single-stranded DNA (ss-DNA) was functionalized on the ZnO surface creating a label-free DNA Schottky-contacted MO<sub>x</sub> field-effect transistor (FET) through a simple drop-cast procedure. A small amount of the ss-DNA was dropped onto

the ZnO NW surface and heated slightly above room temperature for 1 h. This way, complementary DNA strands (c-DNA) are used as analytes of interest.

Other MO<sub>x</sub> NW Syntheses. Han et al. <sup>176</sup> prepared engineered M13 phage templated manganese oxide nanowires. They found that simply stirring engineered M13 phage (M13-E4) with a pH-controlled aqueous manganese acetate (MnAc<sub>2</sub>) solution could precipitate out M13-E4@MnO<sub>2</sub> nanowires. Du et al., <sup>177</sup> Meng et al., <sup>178</sup> and Zeng et al. <sup>179</sup> synthesized tin oxide (SnO<sub>2</sub>) NWs using pulsed laser deposition. The Sn source on a Au/Al<sub>2</sub>O<sub>3</sub> substrate was ablated with an ArF excimer laser. Controlling the metal and O<sub>2</sub> flux led to the creation of SnO<sub>2</sub> nanowires. Suh et al. <sup>180</sup> created nickel oxide-decorated cobalt oxide (NiO-Co<sub>2</sub>O<sub>4</sub>) nanorods using an electron-beam evaporator. They utilized a small range of different glancing angles at a constant rotation speed to uniformly and cyclically deposit Co<sub>2</sub>O<sub>4</sub> and Ni.

Cho et al. 181 used a unique sputtering technique based on ion bombardment combined with lithography steps for the formation of a variety of nanowires. They fabricated copper oxide (CuO), chromium oxide (Cr<sub>2</sub>O<sub>3</sub>), and nickel oxide (NiO) NW arrays. First, a poly(dimethylsiloxane) (PDMS) mold was used to create a polystyrene (PS) prepattern with width and height dimensions of 500 and 350 nm, respectively, on a SiO<sub>2</sub>/Si substrate. Next, varying patterns of a 30 nm layer of Cu, Cr, or Ni were deposited over the PS prepattern via electron beam evaporation. Argon ion (Ar<sup>+</sup>) bombardment was used etch and emit a large distribution of the metals to the side surfaces of the prepattern, which creates the polycrystalline MO<sub>x</sub> NW arrays. Oxygen reactive ion etching was used to remove the PS prepattern. Finally, the patterned metal NW arrays were annealed in a tube furnace at 450 °C for 3 h and allowed to self-cool back to room temperature resulting in the respective CuO, Cr2O3, and NiO NW arrays. Notable in this work are the high aspect ratios that were achieved using this Ar<sup>+</sup> bombardment sputtering process for MO<sub>x</sub> nanowires.

Transduction in Metal Oxide NWs. Chemiresistive. Metal oxide NWs are often configured as chemiresistors for applications in gas sensing. The sensing mechanism involves the change of resistance caused by the interactions between target gas molecules and preadsorbed oxygen on the surface of the sensing structure. 171,182 Most metal oxide NWs can be divided into p-type (CuO, NiO, Cr<sub>2</sub>O<sub>3</sub>, PdO, and Co<sub>3</sub>O<sub>4</sub>) and n-type (ZnO, SnO<sub>2</sub>, TiO<sub>2</sub>, Fe<sub>2</sub>O<sub>3</sub>, MoO<sub>3</sub>, and WO<sub>3</sub>) semiconductors according to their dominant charge carriers (holes for p-type and electrons for n-type). 182 When the sensor is exposed to air, O2 will adsorb onto the surface of the nanostructure and capture electrons from the material's conduction band (CB) to form  $O_2^-$  ( $T_{air} < 100$  °C),  $O^-$  (100 °C <  $T_{air} < 300$  °C), and  $O^{2-}$  ( $T_{air} > 300$  °C). <sup>183</sup> A depletion layer forms at the surface of an n-type metal oxide NW surface, depleting the concentration of electrons and increasing the NW resistance. 184 When the sensor is exposed to reducing gases (H2, CO, and H2S), the reaction between the reducing gas molecules and oxygen anions releases those electrons back into the CB, restoring the NW's resistance to its baseline value. 185 However, the exposure of n-type metal oxide NWs to oxidizing gases (CO<sub>2</sub>, NO<sub>2</sub>, and Cl<sub>2</sub>) increases the width of the depletion layer and further increases the sensor's resistance. 163

The performance of metal oxide NWs as sensors is correlated with the oxygen adsorption capacity of the material surface. The gas sensor's operating temperature, surface

area, and surface conditions combine to determine the oxygen coverage. The large surface area-to-volume ratio of 1D nanostructures introduces a large number of active surface sites for the adsorption of gas molecules, thus enhancing the surface effects. Van Dang et al. Compared the sensing properties of ZnO, WO3, and SnO2 NWs fabricated by CVD. They found that the maximum SnO2 NW response values were about 2 orders of magnitude higher than those of ZnO and WO3, a disparity they attributed to higher oxygen vacancy densities for SnO2 nanowires.

The functionalization of metal oxide NWs with other catalytic materials like noble metals and metal oxide nanoparticles has been a widely studied strategy to enhance gassensing performance. Heterojunctions will be formed on the contact surfaces of different materials, and due to the different Fermi levels of the nanomaterials, the electrons at higher energies flow across the interface to lower-energy states until they reach equilibrium. This creates a depletion region at the interface, which is also how composite nanomaterials become sensitized. The heterojunctions can be divided into metal—metal oxide and p—n-, p—p-, and n—n-type according to the type of material modified.

Noble metals like Pt, Pd, Ag, and Au are widely employed as sensitizers for MO<sub>x</sub> NWs because of their catalytic properties, expanding the gamut of molecules that can be detected. Sensitization by these metals can occur via electronic or chemical mechanisms. 91,188–190 Electronic sensitization causes electrons to be transferred from the MO<sub>r</sub> NW into the metal nanoparticles as Fermi levels equilibrate. The resulting depletion layer within the NW increases the through-nanowire resistance compared to the unmodified metal oxide nanowire. The redistribution of electron density between metal particles and the MO<sub>x</sub> nanowire, induced by the adsorption of electron donating or withdrawing analytes, can amplify the measured resistance change. 189 Chemical sensitization occurs when analyte molecules selectively adsorbed by metal particles are transferred to the MO<sub>x</sub> surface, a phenomenon known as "spillover". The spillover effect can also accelerate the chemical reaction between the chemisorbed oxygen species and dissociated analyte molecules to produce fast response and recovery times. 18

Metal oxide heteronanostructures consisting of two or more composites enhance sensor response and improve selectivity because they can modulate charge transfers by forming p-n, n-n, and p-p heterojunctions. 191,192 Over the past few years, various combinations of nanostructured metal oxides have been developed for high-performance gas sensors utilizing heterojunctions, such as WO<sub>3</sub>/CuO nanochannels, <sup>185</sup> Co<sub>3</sub>O<sub>4</sub>@ NiMoO<sub>4</sub> core-shell nanowires, 192 CeO<sub>2</sub> nanodot-decorated WO<sub>3</sub> nanowires, <sup>184</sup> SnO<sub>2</sub>/Au-doped In<sub>2</sub>O<sub>3</sub> nanofibers, <sup>193</sup> NiOdecorated Co<sub>3</sub>O<sub>4</sub> nanorods, <sup>194</sup> and biaxial SnO/ZnO nanowires. 195 The p-n heterojunctions operate the same way as metal-metal oxide heterojunctions by improving the electronic and chemical sensitization of the sensors. <sup>185,196</sup> For p-p and n-n heterojunctions, the equilibrium states are achieved when charge carriers flow from wide-band gap materials to narrow-band gap materials. 194 An additional depletion layer is generated at the heterojunction interfaces, leading to increased sensor responses when exposed to target gas molecules. 191

*Electrochemical.* The development of electrochemical biosensors for environmental monitoring, health care, and clinical diagnostics has recently become a hot topic due to their advantageous low cost, fast response, easy miniatur-

ization, and suitability for direct analyses.  $^{151,197-199}$  It is well-known that biosensor electrochemical performances can be modified by different compositions and morphologies of electrode nanomaterials.  $^{199}$  Among all the materials to modify electrodes, 1D nanostructured metal oxides like  $Cu_2O$ ,  $MnO_2$ ,  $Fe_2O_3$ ,  $Fe_3O_4$ , ZnO,  $TiO_2$ , and  $Co_2O_3$  have attracted much interest for electrochemical applications in sensors, supercapacitors, and batteries due to the controlled structure for distinct anisotropy, electron transfer, quantum size effect, and large surface area-to-volume ratio.  $^{166,177}$ 

Semiconducting metal oxide NWs usually play two roles in electrochemical sensors. The first role is to immobilize biomolecules in the fabrication of biosensors like immunosensors, enzyme sensors, and DNA sensors, which act as the electron transfer medium. The reaction of a small number of biomolecules produces a large electrical signal, which is easily measurable with electrochemical instruments due to the nanowire's high surface area-to-volume ratio. The second role is to act as electrocatalysts when catalyzing target molecules, such as glucose, dopamine,  $H_2O_2$ , ascorbic acid, dihydroxybenzene, and L-cysteine.  $I_{1,162,198,199,201-203}$ 

The direct immobilization of the biomolecules on the surface of semiconducting metal oxide NWs could be realized via weak intermolecular forces such as van der Waals, electrostatic, or physisorption interactions. However, the chemical functionalization of the metal oxide surface is usually conducted to get a more reliable covalent binding and help biomolecules retain a higher stable activity. Gold nanoparticles (Au NPs) are biocompatible and have high chemical affinity with thiol groups, thus enabling easy binding of thiol-terminated DNA and improving binding selectivity.<sup>204</sup> Carbon nanomaterials such as graphene and carbon nanotubes are also commonly used dopants in metal oxide NW biosensors. The carbon contents on graphene or carbon nanotubes are activated with -COOH functional groups via the EDC-NHS coupling mechanism. The amidation coupling reactions can cause the formation of amide bonds (C-N) between the -NH<sub>2</sub> groups of the biomolecules and activated -COOH groups of the composite materials, resulting in a higher stability and enhancing loading capacity for biomolecules.

Although electrochemical sensors based on metal oxide catalysis have been extensively studied in recent years, some problems including unsatisfactory selectivity and low sensitivity and stability due to surface pollution by the adsorbed nonspecific interferent still remain challenging and hinder their use in the bioenvironment. Additionally, the relatively large resistances of metal oxide semiconductors (MOS) also limits the efficiency of electron transfer along the nanowires. Researchers are looking for new metal oxide nanomaterials, making new nanostructures or modifying noble metals on the surface of semiconductors to improve their conductivity and catalytic efficiency. Efforts in this front are motivated by decreasing the working potential, reducing the influence of interfering substances, and improving the performance of the sensor. 162,176,198,203

Surface modification is a commonly used method to improve the catalytic performance of metal oxide NWs. Le et al. <sup>198</sup> found that Au nanoparticles on Cu@Cu<sub>x</sub>O NWs formed strong interactions between Au—Cu and produced synergistic effects. Au nanoparticles not only increase the electrode area and electroactive sites, but also accelerate charge transfer, thereby improving the sensing performance. Ag nanoparticles have also been shown to improve the electron transfer between

the analyte molecules and metal oxide NWs by catalyzing the reactions at a lower overpotential and reducing the influence of interfering substances on the sensor. Modification of another metal oxide nanostructure on the surface of a metal oxide NW is also an effective way to improve its catalytic performance. The electrocatalytic capability of  ${\rm Co_3O_4}$  NWs is reported to increase significantly when hybridized with  ${\rm ZnCo_2O_4}$  nanoflowers. Core—shell  ${\rm IrO_2@NiO}$  NWs also exhibited superior electrocatalytic activity over pure NiO nanoflowers and  ${\rm IrO_2}$  NWs, which is attributed to the metallike conductivity (resistance of ~50  $\mu\Omega$  cm<sup>-2</sup> in bulk) of  ${\rm IrO_2}^{200}$  MnO<sub>2</sub> is a transition metal oxide that has high redox activity but poor conductivity. When combined with  ${\rm Co_3O_4}$ ,  ${\rm Co_3O_4}$  provides a conducting network for MnO<sub>2</sub> yielding high electron conductivity and enhancing direct electron transfer with the target biomolecules.

Field-Effect Transistors (FETs). FET NW-based sensors have attracted attention in chemical and biological sensing due to their high sensitivity, capability for direct (label-free) signal transduction and point-of-care integration. Semiconducting metal oxides, especially  $\rm In_2O_3$ ,  $\rm ZnO$ ,  $\rm \beta\textsc{-Bi}_2O_3$  and ITO, have been widely studied as FET sensors. Recent work has focused on improving device performance and more scalable fabrication, such as the use of chemical lift-off lithography, shadow mask patterning, and photochemical activation with UV light.  $^{208-210}$ 

The back-gated FET is the most common FET architecture. It allows gate control of carrier densities without exposing the gate electrode to solutions and analytes, thereby minimizing interference from these sources. In most bioFET application scenarios where the analytes are detected in an aqueous environment, a liquid gate, usually an Ag/AgCl reference electrode, is used to apply a stable electrolyte bias to operate the biosensor. To make bioFET sensors more suitable for point-of-care or wearable applications, the development of a miniature reference electrode is necessary. A fully integrated on-chip gold side gate is reported to show good electrical performance compared with an external Ag/AgCl electrode in an aqueous electrolyte, which has great potential for wearable healthcare electronics.<sup>211</sup>

As already noted in connection with semiconductor NWs above, the effective sensing distance of FET biosensors in solution is characterized by the Debye length, which in physiological fluids is typically <1 nm. 212 Back gated FET NWs are reported to permit localized control of net charge and reduce the Debye screening effect, which improves the sensors sensitivity. 213 Sandwich enzyme-linked immunosorbent assays (ELISA) can be used in conjunction with NWs to bypass Debye screening length issues from ions in the fluid.<sup>210</sup> ELISA also amplifies signal by improving the signal-to-noise ratio, which is desirable when working with trace amounts of analyte. Related to Debye length limitations, a specific type of oligonucleotide stem-loop receptor selected for adaptive target recognition is immobilized on bioFET. 212 The designed positioning of recognition regions capable of adaptive conformational changes in the new aptamer allows the designed FET to overcome the Debye length limitations for small-molecule sensing.

**Recent Research.** Chemiresistive. Metal oxide NWs, configured as chemiresistors, have been extensively investigated as gas sensors. They have been employed in applications ranging from air pollution and safety monitoring to disease diagnostics and health supervision. The n-type metal

oxides materials such as ZnO, SnO<sub>2</sub>, TiO<sub>2</sub>, WO<sub>3</sub>, and In<sub>2</sub>O<sub>3</sub> have been primarily used in MOS-based gas sensors because of their high sensitivity and fast responses.<sup>214</sup>

Ren et al. <sup>147</sup> used multilayer crossed WO<sub>3</sub> NW arrays for selective acetone sensing. These NW arrays showed a fast and reversible gas sensing response with the response defined as  $R_{\rm air}/R_{\rm gas}$  for the reducing acetone vapor. The response and recovery times were 5 and 12 s, respectively, for a sensor in 50 ppm acetone. They also showed that these rapid response and recovery times were achievable even for exposures of up to 1400 s and for concentrations across the range from 1.0 to 400 ppm. The selectivity of this response was demonstrated by probing responses to ethanol, CO, NH<sub>3</sub>, methanol, H<sub>2</sub>S, and formaldehyde.

Song et al. <sup>150</sup> utilized SnO<sub>2</sub> nanorods on reduced graphene oxide (rGO) nanosheet for room temperature H<sub>2</sub>S gas sensing. These nanorods were sensitive to 50 ppm H<sub>2</sub>S even when tested against background gases containing the same concentration of NH<sub>3</sub>, SO<sub>2</sub>, NO<sub>2</sub>, and ethanol vapor (the responses were 33, 1.27, 1.47, 0.65, and 0.94, respectively) at 22 °C. Excellent linear and continuous response—recovery times were observed for these systems with response times of 2–13 s across a H<sub>2</sub>S concentration range of 10–100 ppm. A LOD of 43 ppb at 22 °C was estimated. It was hypothesized that the enhanced electron transfer at the SnO<sub>2</sub>—rGO interface promoted rGO as the electron acceptor from SnO<sub>2</sub>, contributing to this sensing performance.

Zhou et al. 172 examined the influence of crystal defects on an individual ZnO NW on acetone sensing. Optimal NW width and temperature were 110 nm and 350  $^{\circ}\text{C}$  in this study. The response to 5 ppm acetone was 42, where they defined the response as  $R_{\rm air}/R_{\rm gas}$ . The number and nature of the defects in ZnO NWs were assessed using photoluminescence. The optimum 110 nm width ZnO NWs exhibited the most donor levels, which is pivotal to the enhanced gas response as they contributed more electrons for the reduction between acetone and surface adsorbed oxygens. The ZnO NWs became negatively charged when exposed to air due to the surface oxygen species adsorbing onto their surfaces, thereby removing electrons from its conduction bands and shuttling them to the oxygen species. More adsorbed oxygen species result from more electron donors, as they increase the free electrons compared to the acceptors that consume those electrons in the ZnO. The exposure to air maximizes the donor levels while minimizing the acceptor levels so the ZnO can adsorb more oxygen species. The introduced acetone reacts with the adsorbed oxygens, thus returning those free electrons back to the ZnO conduction band, decreasing the nanowires' resistance. Here, they demonstrated the pivotal role that inherent structural defects play in gas sensor responses and concluded that the response is more dependent on this rather than on NW junctions.

Kwon et al.  $^{173}$  created surface defects on SnO<sub>2</sub> NWs using He<sup>2+</sup> beam irradiation and evaluated the influence of these defects on the NO<sub>2</sub> sensing properties of these nanowires. The sensor sensitivity toward NO<sub>2</sub> increased when the ion fluence was increased to  $1 \times 10^{16}$  ion/cm<sup>2</sup> for 2 ppm NO<sub>2</sub> and 150 °C. Response and recovery times were in the 200–300 s range for these systems. Selectivity to NO<sub>2</sub> was assessed relative to acetone, ethanol, H<sub>2</sub>, NH<sub>3</sub>, and SO<sub>2</sub>, but the ablated SnO<sub>2</sub> NWs remained significantly sensitive toward NO<sub>2</sub>. This study was the first at the time to report significant effects of He<sup>2+</sup> irradiation on a metal oxide nanowire's sensing capability. Its

conclusion is that the surface defects, especially Sn interstitials, created by the  ${\rm He^{2^+}}$  irradiation promoted  ${\rm NO_2}$  adsorption, which enhanced the sensor response.

Drobek et al. 149 showcased the selectivity of ZnO@ZIF-8 NWs toward hydrogen gas. The response defined as  $R_{\rm air}/R_{\rm gas}$  was present, albeit at a smaller response than just the ZnO NWs themselves. The responses at 300 °C toward 10, 30, and 50 ppm H<sub>2</sub> were 2.34, 2.47, and 2.62, respectively, for just ZnO, whereas for ZnO@ZIF-8, they were 1.17, 1.34, and 1.44. The exposure to two hydrocarbons that normally interfere with the H<sub>2</sub> response at ZnO,  $C_6H_6$ , and  $C_7H_8$  showed no measurable responses at ZnO@ZIF-8 sensors. It was concluded that the ZIF-8, which has pores just slightly larger than the kinetic diameter of H<sub>2</sub>, functions as a prefilter to block access to the ZnO NW of larger  $C_6H_6$  and  $C_7H_8$  while allowing H<sub>2</sub> to diffuse readily.

Chen et al. <sup>152</sup> utilized ZnO NWs for UV-assisted detection of formaldehyde (HCHO) in ambient air and temperature. UV light irradiation on the NWs in ambient air generated photoelectrons, which reacted with the adsorbed oxygen species to create reactive oxygen species. When it oxidized HCHO, the electrons were released back to ZnO, causing an increased photocurrent. Using this strategy, HCHO was detected across a concentration range of 1–200 ppm with responses that were 20 and 15 times higher than those of ZnO nanoparticles and nanorods, respectively. Responses down to 5 ppb HCHO were demonstrated.

Katwal et al.<sup>161</sup> utilized a ZnO hybrid nanotube/nanowire structure with a porous structure to detect acetophenone (AP), isopropyl alcohol (IP), heptanal (HA), and isopropyl myristate (IPM), all of which are biomarkers for breast cancer found in exhaled breath. Responses for 100 ppm of each AP, IP, and HA and 100 ppb IPM were demonstrated at 250 °C. Significant selectivity of these ZnO hybrid NWs was demonstrated versus either CO<sub>2</sub> and methane, two other constituents of exhaled breath.

p-type MOS gas sensing materials are less commonly investigated because they have been found to exhibit lower sensitivity and slower response and recovery times than n-type metal oxides. Cho et al. and a significant step toward overcoming the limitations of p-type metal oxide-based sensors for VOC detection. They fabricated ultrathin, polycrystalline p-type metal oxide NW arrays consisting of arrays of edgeoriented NRs with a thickness of  $\sim 14$  nm and height of 300 nm and having 5 nm grains using a novel secondary sputtering lithography technique. These diminutive NWs possessed extremely high surface area/volume ratios that resulted in high signal amplitudes ( $\Delta R/R_a=30$  to 1 ppm hexane using NiO NWs) and rapid responses ( $\approx 30$  s).

Surface functionalization is another efficient way to enhance gas-sensing performance aside from increasing specific surface area. Heterojunctions form on the interfaces of different materials causing electronic and chemical sensitization, which improve the performance of the sensor. Choi et al.  $^{188}$  decorated Ag nanoparticles on the surface of high-resolution  $\rm CuO/Cu_2O$  nanochannels. The gas response of the modified  $\rm CuO/Cu_2O/Ag$  sensor increases by a factor of 7.3 for VOC detection.

Similarly, Penner and co-workers  $^{91}$  prepared Pt nanoparticle-functionalized palladium oxide NW (Pt-PdO NW) arrays for  $\rm H_2$  detection. The spillover effect induced by decorated Pt NPs activated the dissociation and diffusion of  $\rm O_2$  and  $\rm H_2$  molecules. The Pt-PdO NWs showed an enhanced

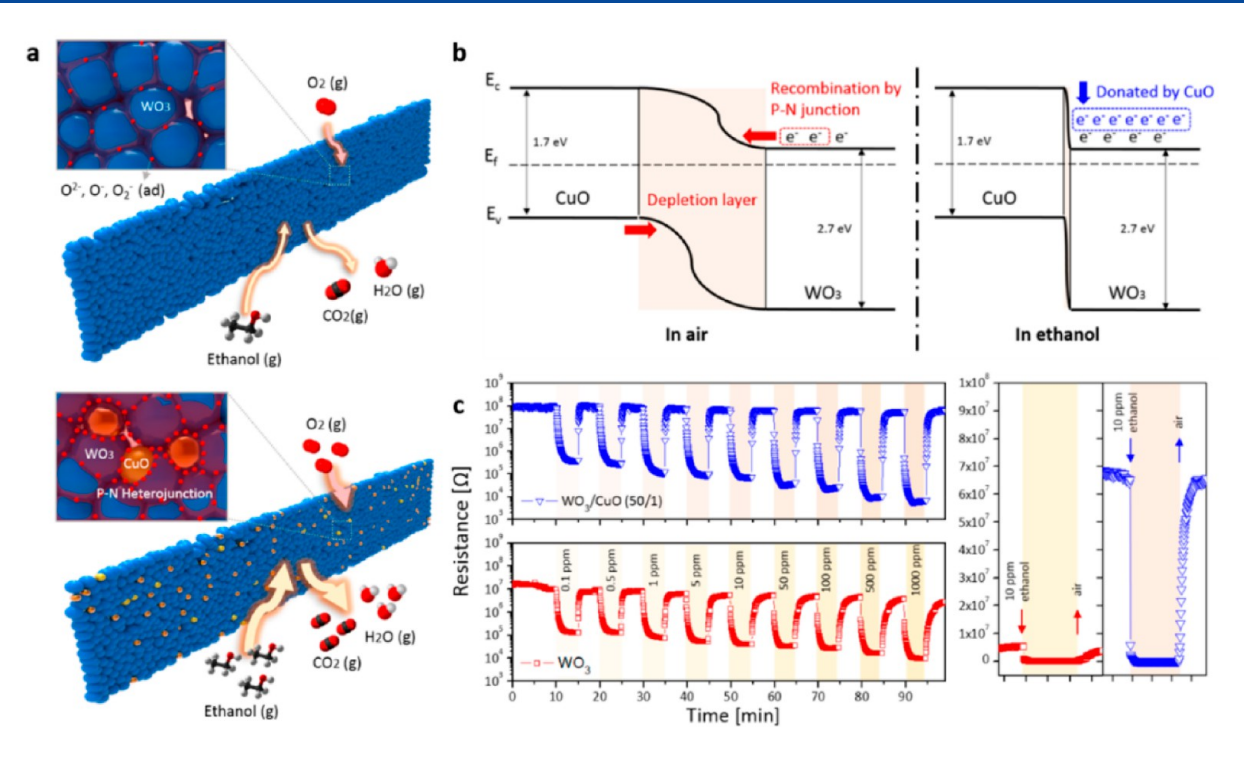


**Figure 9.** WO<sub>3</sub>/CuO heterojunction nanochannel for an ethanol sensor. (a) Schematic illustrations showing the ethanol-sensing mechanism of pristine WO<sub>3</sub> and WO<sub>3</sub>/CuO nanopatterns with a p—n heterojunction. (b) Band diagram of the ethanol-sensing mechanism showing depletion layer variation and electron flow. (c) Transient real-time resistance change in pristine WO<sub>3</sub> and WO<sub>3</sub>/CuO nanopattern sensors for ethanol levels ranging from 0.1 to 1000 ppm. Reproduced from Cho, S.-Y.; Jang, D.; Kang, H.; Koh, H.-J.; Choi, J.; Jung, H.-T. Ten Nanometer Scale WO<sub>3</sub>/CuO Heterojunction Nanochannel for an Ultrasensitive Chemical Sensor. *Anal. Chem.* **2019**, *91* (10), 6850–6858 (ref 185). Copyright 2019 American Chemical Society.

sensitivity and faster response for  $H_2$  relative to pristine PdO NWs. Choi et al. <sup>169</sup> developed a single-step synthetic method for producing Pt NP functionalized macroporous WO<sub>3</sub> NFs during electrospinning. Functionalized by Pt NPs, the asprepared Pt-WO<sub>3</sub> NFs exhibited dramatically improved  $H_2S$  sensing with a high response of 834.2  $\pm$  20.1 at 5 ppm in a humid ambient with substantial selectivity relative to interfering analytes.

Song et al. 164 used Sr-doped In<sub>2</sub>O<sub>3</sub> NWs for ethanol sensing in breath, a diagnostic for fatty liver disease. An ethanol sensing range from 0.1 to 1 ppm at 300 °C was possible with responses of 5 and 21, respectively, where the response was defined as  $R_{air}/R_{gas}$ . A detection limit of 25 ppb ethanol was estimated, well under 380 ppb, the reported value for endogenous ethanol in breath. The response and recovery times were reported to be under 1 min for both. Sr-doped multiphase In<sub>2</sub>O<sub>3</sub> NWs were found to be selective for ethanol in the presence of other VOCs as it displayed the highest response, 138, toward 50 ppm ethanol and a lower response, <10, to methanol, acetone, formaldehyde, toluene, xylene, and benzene at the same concentration at 300 °C. A Sr dopant enhanced the surface reaction between ethanol and adsorbed oxygen species due to more favorable dissociation between Sr and O, further decreasing the In2O3 NW conductivity. Density functional theory (DFT) calculations showed that Sr-doping induces a structural shift of the In2O3 from a cubic to a rhombohedral phase, leading to increased structural stability and thus enhanced ethanol sensitivity and response.

In addition to modifying the surface of  $MO_x$  NWs with noble metals, the use of another metal oxide as a modifier to form a heterojunction can also provide an effective strategy for

modifying the sensor response. Cho et al. <sup>185</sup> reported a 10 nm scale p—n heterojunction sensing channel between CuO p-type dopants and WO<sub>3</sub> n-type channels. The contact between each small grain of CuO and WO<sub>3</sub> induces the formation of numerous p—n heterojunction interfaces, which extends the depletion layers on the surface of each grain in the sensing channel (Figure 9a). The extended WO<sub>3</sub>/CuO's depletion layer thinned when exposed to ethanol. The electrons were donated back to the conduction band, resulting in a large change in resistivity (Figure 9b). The WO<sub>3</sub>/CuO nanochannel exhibited an ultrasensitive detection performance toward ethanol, 12 times higher than that of a pristine WO<sub>3</sub> nanochannel (Figure 9c). A limit of detection of 0.094 ppb was calculated, which is among the best ethanol-sensing performances for previously reported MOS NW-based sensors.

Hung et al. <sup>195</sup> reported biaxial p-SnO/n-ZnO heterostructured NWs (average length of 10  $\mu$ m) with spherical ball tips grown on glass substrates. All the biaxial NWs are characterized with an epitaxial relationship between SnO and ZnO. The as-prepared sensor exhibits a good performance to the NO<sub>2</sub> with a detection limit of 50 ppb at room temperature.

Choi et al.  $^{186}$  reported p-TeO $_2$ -branched n-SnO $_2$  nanowires. The generation of defects during the growth of TeO $_2$  branches caused by a lattice mismatch between TeO $_2$  and SnO $_2$  enhanced the sensitivity of the sensor. Moreover, the nano branches greatly increased the nanowires' surface area and provided more adsorption sites on the surface of the gas sensor. The TeO $_2$ /SnO $_2$  composite NWs exhibited enhanced NO $_2$  sensing metrics when compared with pristine SnO $_2$  nanowires.

Yao et al. 148 sensed acetone gas with n-type ZnO NWs covered in a thin layer of p-type ZIF-CoZn. The response, defined as  $R_{\text{air}}/R_{\text{analyte}} - 1$ , showed a good current response over a wide range of acetone concentrations, 0.24-100 ppm, and maintained a stable response, 27, toward acetone up to 90% relative humidity at 260 °C. The ZIF-CoZn selectivity is attributed to the MOF layer acting as a filtering membrane that allowed access to the ZnO NWs for acetone while blocking water. A limit of detection of 0.0019 ppm was reported, using a ZIF-CoZn thickness of 5 nm. The same thickness also exhibited the fastest response and recovery times of 0.72 and 1.02 min, respectively, for 100 ppm acetone. Co<sup>2+</sup> centers in the ZIF-CoZn catalytically activated the oxygen species toward acetone oxidation, a mechanism that improved the response and recovery performance of these systems relative to pure ZnO nanowires.

Wang et al. 154 used ZnO NW-incorporated black phosphorus (BP-ZnO) nanocomposites for trace NO<sub>2</sub> sensing. The BP-ZnO sensors showed an excellent steadystate dynamic response for the extremely low concentrations of 50, 75, 100, and 125 ppb NO<sub>2</sub> at room temperature. BP-ZnO showed reproducible and stable dynamic response curves upon cyclic introduction of 75 ppb NO<sub>2</sub>, albeit with some drift for up to 10 days. Interfering gases like NO, SO<sub>3</sub>, NH<sub>3</sub>, CO, HCHO, H<sub>2</sub>S, and H<sub>2</sub>O vapor at concentrations of 10 ppm and 40% relative humidity, respectively, were introduced alongside trace 75 ppb NO<sub>2</sub>. Strong NO<sub>2</sub> selectivity was observed despite the higher concentration of interfering gases, which was attributed to stronger binding energy between BP-ZnO and NO2. The enhanced sensing mechanism of BP-ZnO when compared to BP was attributed to the formation in the composite material of a large number of p-n heterojunctions able to contribute to the sensing response. Significantly, the performance of all these systems for the detection of NO2 was achieved at near-room temperature.

Kim et al. 158 used PtPd-, PtRh-, and PtNiO-WO3 nanofibers, prepared by electrospinning, to detect acetone and H2S as biomarkers for diabetes and halitosis, respectively, in exhaled breath. Nanofibers of PtPd- and PtRh-WO3 showed selectivity toward acetone in the presence of other interfering gases like H<sub>2</sub>S, methyl mercaptan, toluene, CO, H<sub>2</sub>, ethanol, and ammonia at 1 ppm. PtNiO-WO<sub>3</sub> nanofibers, on the other hand, were selective toward H<sub>2</sub>S in the presence of these gases. The PtPd-WO<sub>3</sub> nanofibers showed the highest acetone response of 97.5 for 1 ppm at 300 °C where response is defined as the resistances of the sensor in air and analyte gas  $(R_{\rm air}/R_{\rm gas})$  and displayed a LOD of ~1.07 ppb. The PtRh-WO<sub>3</sub> also showed the highest response, 104, toward acetone for the same concentration at 300 °C with a LOD below 0.3 ppb. The PtNiO-WO<sub>3</sub> nanofibers displayed the highest response, 340, for 1 ppm H<sub>2</sub>S at 300 °C with an excellent LOD reaching below 54 ppt. The response and recovery times for the PtPd-WO<sub>3</sub> nanofibers sensing 1 ppm acetone at 300 °C were 4.2 and 204 s, respectively, while those for the PtRh-WO<sub>3</sub> nanofibers sensing the same concentration of acetone at 350 °C were 3 and 176 s, respectively. The PtNiO-WO3 nanofibers displayed response and recovery times of 4.4 and 240 s for 1 ppm H<sub>2</sub>S at 300 °C.

Jeong et al. 160 showed an enhanced acetone response using PtO<sub>2</sub>-loaded SnO<sub>2</sub> "multichannel" nanofibers prepared using an electrospinning process. Multichannel in this context refers to fibers containing an ensemble of >10 independent 1D PtO<sub>2</sub> nanoparticle arrays. The highest obtained response was 194 for

5 ppm acetone at 400 °C, where the response is defined as  $R_{\rm air}/R_{\rm gas}$ . These systems were selective toward acetone even when tested against other interfering gases like ethanol, methane, CO, formaldehyde, NH<sub>3</sub>, toluene, and H<sub>2</sub>S with a response of 21.94 at 1 ppm acetone versus a response of <9.1 at 1 ppm of the interfering gases. This selectivity was attributed to the formation of ensembles of p—n heterojunctions between the p-type PtO<sub>2</sub> and n-type SnO<sub>2</sub> coupled with the unique multichannel architecture of these systems. The PtO<sub>2</sub> increases the resistance change when the surface oxygen species formed on the SnO<sub>2</sub> surface react with acetone because there are more oxygen species present. In tandem, the multichaneled structure also affords an enhanced surface area for oxygen adsorption—desorption sites and allowed for better acetone diffusion to these sites.

Bulemo et al. 167 detected H<sub>2</sub>S with Pt/PtO<sub>x</sub> nanoparticledecorated SnO<sub>2</sub> mesoporous nanotubes at high relative humidity to mimic exhaled breath. A response of 154.8 for 5 ppm H<sub>2</sub>S at 300 °C was obtained, where the response is defined as  $R_{\text{air}}/R_{\text{gas}}$ . The detection limit was 100 ppb  $H_2S$ . The Pt-SnO<sub>2</sub> mesoporous nanotubes were tested against interfering gases, including ethanol, H<sub>2</sub>, acetone, CO, NH<sub>3</sub>, C<sub>7</sub>H<sub>8</sub>, and  $C_5H_{12}$  also at 5 and 1 ppm at 300 °C, but these sensors produced responses an order of magnitude higher for H<sub>2</sub>S, demonstrating their high selectivity. While the response times, 58.1 and 99.5 s, and recovery times, 122.3 and 111.6 s, were relatively long for 5 and 1 ppm H<sub>2</sub>S, respectively, the high selectivity within the sub-ppm range is emphasized. This performance was attributed to the porous surface of these NWs, which was afforded by the high surface areas, coupled with the Pt nanoparticles, which are capable of dissociating oxygen into ionized oxygen species that can be adsorbed onto the SnO<sub>2</sub> surfaces.

Yuan et al. 155 utilized CeO<sub>2</sub> nanodot-decorated WO<sub>3</sub> (Ce-d-WO<sub>3</sub>) NWs for acetone sensing. The optimization of this system yielded a best response of 1.31 for 500 ppb acetone at 250 °C where response is defined as  $R_{air}/R_{gas}$ . This response also showed linearity with the acetone concentration from 500 ppb to 2.5 ppm. The response-recovery times for 2.5 ppm acetone were rapid, 34 and 68 s, respectively. The Ce-d-WO<sub>3</sub> NWs were tested against relative humidity showing responses of 1.28 and 1.24 at 0.5 ppm acetone for 20% and 80% relative humidity, respectively. This showcased a strong humidityresistant characteristic as well as high selectivity toward acetone. The sensor showed a response of 1.65 toward 2.5 ppm acetone with minute responses toward the same concentration of HCHO, toluene, NH<sub>3</sub>, H<sub>2</sub>S, NO<sub>2</sub>, and CH<sub>4</sub> acting as interfering gases. The heterojunction is indicated as the primary reason for the enhanced response followed by the increased oxygen adsorption sites. The small CeO2 nanodots increased the number of oxygen-trapped electrons in the electron accumulation layer and the hole accumulation layer at the interface between CeO<sub>2</sub>/WO<sub>3</sub> also increased the electrons that are returned upon acetone oxidation.

 $\rm SnO_2/Au$ -doped  $\rm In_2O_3$  core—shell nanofibers were used for acetone detection. The  $\rm SnO_2/Au$ -doped  $\rm In_2O_3$  core—shell NF sensor showed enhanced acetone gas sensing with a response of  $R_a/R_g = 20.8$  at  $280~\rm ^{\circ}C$ .  $\rm RuO_2$ -functionalized  $\rm WO_3$  nanofibers showed outstanding acetone sensing performance in a highly humid atmosphere, indicating a potential use in diabetes diagnosis from exhaled breath. Yuan et al.  $^{184}$  also reported n-CeO<sub>2</sub> nanodot-decorated n-WO<sub>3</sub> NWs, which exhibited a remarkable acetone-sensing performance with a

high response (S = 1.30 at 500 ppb), low detection limit (500 ppb), and superior selectivity.

Two different core-shell heterostructure nanofibers, In<sub>2</sub>O<sub>3</sub>-SnO<sub>2</sub> NFs and SnO<sub>2</sub>-In<sub>2</sub>O<sub>3</sub> NFs, were used to detect trimethylamine and compared between each other.<sup>216</sup> The In<sub>2</sub>O<sub>3</sub>-SnO<sub>2</sub> NFs displayed a higher response than the SnO<sub>2</sub>-In<sub>2</sub>O<sub>3</sub> NFs (7.11 and 1.75, respectively) with faster response and recovery times (3 and 32 s for the In<sub>2</sub>O<sub>3</sub>-SnO<sub>2</sub> NFs as opposed to 47 and 313 s for the SnO<sub>2</sub>-In<sub>2</sub>O<sub>3</sub> NFs). This remarkable difference is associated with the electron flow and the formation of the depletion layer on the heterostructure surface. The work function of In2O3 is higher than SnO2, so electrons will flow from In2O3 to SnO2, producing a depletion layer on the In<sub>2</sub>O<sub>3</sub> surface. For the In<sub>2</sub>O<sub>3</sub>-SnO<sub>2</sub> core-shell structure, there is one depleted layer in the shell and one depleted layer in the core while two depleted layers exist in the shell for the SnO<sub>2</sub>-In<sub>2</sub>O<sub>3</sub> core-shell structure. These depleted layers lead to the differences in gas sensing performance. This study highlights the importance of core-shell structure design to realize more sensitive MOS NW sensors.

The study of p-p heterojunctions for MOS NW sensors is considerably lower than the widely studied p-n and n-n heterojunctions in recent years. Suh et al. <sup>194</sup> reported NiO-decorated  $Co_3O_4$  NRs fabricated with multiple-step glancing angle deposition. The effective decoration of NiO on the whole surface of  $Co_3O_4$  NRs enabled the formation of numerous p-p heterojunctions. The NiO/ $Co_3O_4$  NRs exhibited a 16.78 times higher gas response to 50 ppm  $C_6H_6$  compared to that of bare  $Co_3O_4$  NRs with a detection limit of 13.91 ppb. Qu et al. <sup>192</sup> also reported hierarchical  $Co_3O_4$  ( $O_3O_4$  NiMoO4 core—shell NWs synthesized by the hydrothermal method. Due to the synergistic catalytic effect and the formation of a p-p heterostructure, the  $Co_3O_4$  ( $O_3O_4$  NiMoO4 core—shell NWs showed a high chemiresistive response ( $O_3O_4$  Rair = 24.6) to xylene at 100 ppm with a low detection limit of 424 ppb.

limit of 424 ppb.

Long et al. <sup>157</sup> utilized a  $ZnCo_2O_4$  dandelion-like structure with a needle-like NW for HCHO sensing. They used a suspended microheater design to mitigate power loss through thermal conservation and determined the highest response, ~100, to 5 ppm HCHO was at 250 °C, where the response is defined as  $(R_{\rm gas}-R_{\rm air})/R_{\rm air}$  (%), but the optimum temperature was chosen as 300 °C since the response and recovery times, ~18 and ~24 s, respectively, were rapid at little expense to the response. They reported a limit of detection of 3 ppb while 50 ppb was the lowest reliable concentration due to their limited gas delivery setup. No clear plateau up to 10 ppm was shown, indicating higher HCHO concentrations could be measured. The high sensitivity resulted from electron depletion layers extending to the whole grain of the  $ZnCo_2O_4$  coupled with the numerous available surface sites for gas diffusion and oxidation.

*Electrochemical*. Metal oxide NWs are widely used to develop electrochemical sensors in the area of heath care, food industry, and environmental protection. A label-free immunosensor based on iridium oxide (IrO<sub>x</sub>,  $0 \le x \le 2$ ) nanofibers was developed for the detection of the cancer biomarker α-fetoprotein (AFP).<sup>217</sup> The unique wire-in-tube nanostructure of the IrO<sub>x</sub> nanofibers provided channels for rapid electron transfer and a stable matrix for the conjugation of biomolecules. The device exhibited an enhanced electrochemical signal for the detection of AFP over a wide concentration range of 0.05–150 ng/mL with a detection limit of 20 pg/mL.

Ali et al. 166 also reported a label-free microfluidic immunosensor based on the hierarchical composite of graphene foam (GF) and titanium dioxide (nTiO<sub>2</sub>) nanofibers for the early detection of epidermal growth factor receptor 2 (ErbB2) proteins. The carbon contents in the GF-nTiO<sub>2</sub> composite enabled the formation of covalent binding between amide bonds and antibody molecules via the amidation coupling reactions, which enhanced the anti-ErbB2 loading capacity of the immunosensor. In addition, oxygen-vacancy-induced point defects in TiO<sub>2</sub> improved the stability with adsorbates on the surface. Results from pulse voltammetry and electrochemical impedance spectroscopy indicated both high sensitivity and wide detection range toward ErbB2 protein.

As one of the most vastly studied electrochemical sensors, nonenzymatic glucose sensors have always drawn much attention, and some new work has been reported in recent years. Wang et al. designed hierarchical core—shell IrO2@ NiO NWs, which have improved conductivity and accelerated the catalytic reaction toward glucose. With a high sensitivity of 1439.4  $\mu$ A mM<sup>-1</sup> cm<sup>-2</sup> and a low detection limit of 0.31  $\mu$ M, the proposed sensor could be used in monitoring glucose levels, enabling the detection of diabetes in individuals.

Sinha et al. <sup>156</sup> also reported a highly sensitive and selective nonenzymatic glucose sensor achieved by decorating the surface of  $\alpha$ -MnO<sub>2</sub> nanorods with Co<sub>3</sub>O<sub>4</sub> nanoparticles. The synergistic and interfacial effects between  $\alpha$ -MnO<sub>2</sub> and Co<sub>3</sub>O<sub>4</sub> led to enhanced electrochemical characteristics and demonstrated an excellent catalysis toward glucose oxidation. The synthesized  $\alpha$ -MnO<sub>2</sub>/Co<sub>3</sub>O<sub>4</sub> electrode exhibited a high sensitivity of 127  $\mu$ A mM<sup>-1</sup> cm<sup>-2</sup> with a detection limit of 0.03  $\mu$ M, which demonstrates its potential utilization in the clinical detection of diabetes.

A novel plasmon-aided photoelectrochemical nonenzymatic glucose sensor based on  $\operatorname{Au-NiO}_{1-x}$  hybrid NWs was fabricated by Wang et al. <sup>84</sup> Au NPs were incorporated into the  $\operatorname{NiO}_{1-x}$  NW matrix to absorb sunlight and acted as a plasmon exciter. Upon SPR excitation, the generated hot holes on the Au surface effectively transferred to proximate Au and  $\operatorname{NiO}_{1-x}$  to form the corresponding oxide, which further participates in glucose oxidation. This glucose sensor exhibited an ultrahigh sensitivity of 4.061 mA cm<sup>-2</sup> mM<sup>-1</sup> within the detection range of 0.005–15 mM.

In addition to glucose sensors, the application of metal oxide NWs in other biosensors has also been widely reported in recent years. H<sub>2</sub>O<sub>2</sub> plays an important role in regulating signal transduction processes in cellular reactions. The accumulation in cellular compartments from overproduction can cause severe damage to cells and both neurodegenerative and cardiovascular diseases.<sup>218</sup> Mani et al.<sup>197</sup> reported a H<sub>2</sub>O<sub>2</sub> sensor based on ZnCo<sub>2</sub>O<sub>4</sub>/Co<sub>3</sub>O<sub>4</sub> ternary nanoarrays on a Cu foam for real-time monitoring of H2O2 concentration in live cells. Due to the outstanding electrocatalytic activity of ZnCo<sub>2</sub>O<sub>4</sub>, the sensor operated at a minimized overpotential (-0.10 V vs Ag/AgCl), which is much lower than the oxidation potential of common biological species and provided excellent anti-interference performance. The modified electrode demonstrated an ultralow detection limit of 1 nM and quantified the amount of H<sub>2</sub>O<sub>2</sub> released from mammalian cells

 $(8.7 \times 10^{-14} \text{ mol})$ . Le et al. <sup>198</sup> fabricated a unique hierarchical nanostructure based on Au nanoparticle-decorated Cu@Cu<sub>x</sub>O NW arrays and applied them as a novel binder-free biosensor toward L-cysteine detection. The Au nanoparticles induced strong

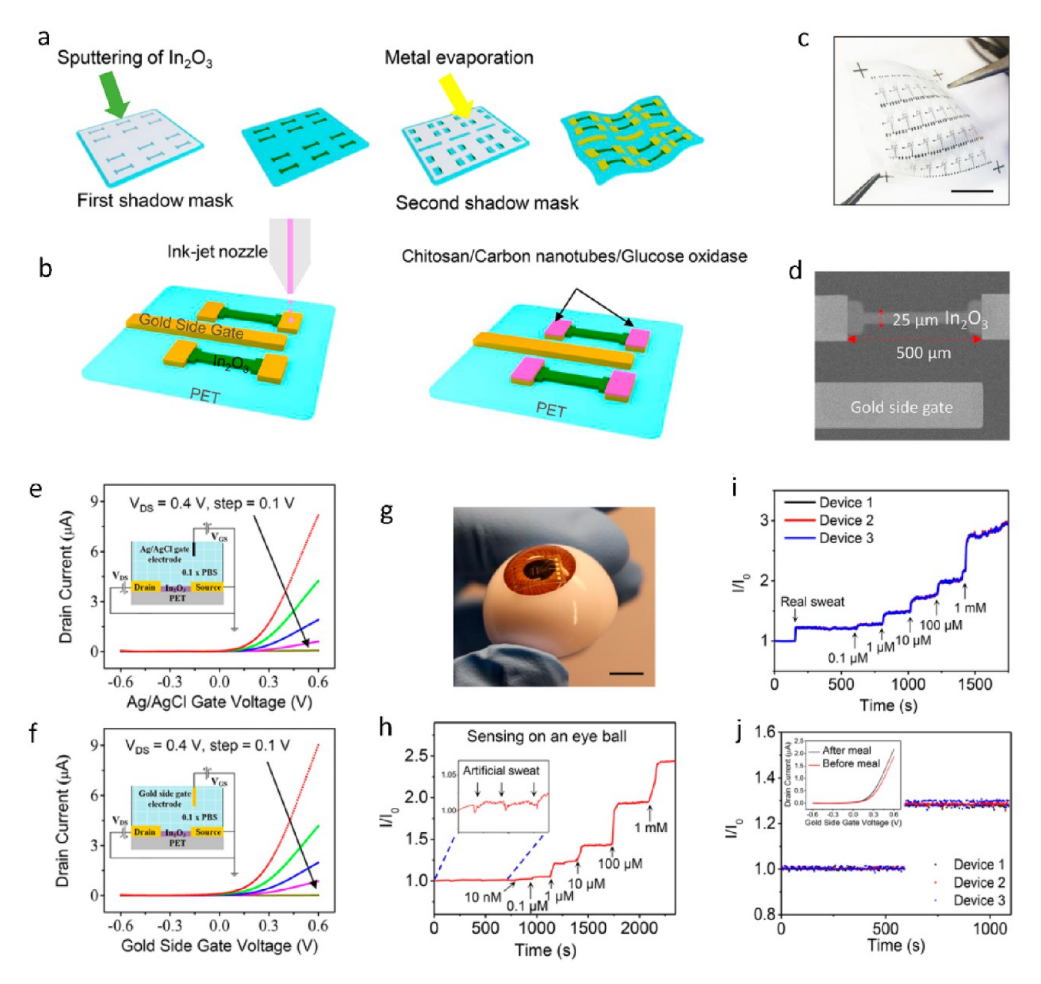


Figure 10. In<sub>2</sub>O<sub>3</sub> NR FET biosensor. (a) Schematic diagrams showing the fabrication procedure of In<sub>2</sub>O<sub>3</sub> FETs on a PET substrate using two-step shadow masks. (b) Schematic diagrams of functionalization on the surface of the electrodes using inkjet printing. (c) Photograph of as-fabricated In<sub>2</sub>O<sub>3</sub> FETs. Scale bar is 1 cm. (d) SEM image of an In<sub>2</sub>O<sub>3</sub> NR device and a gold side gate electrode. Drain current versus Ag/AgCl gate (e) and gold side gate (f) voltage with drain voltage changing from 0.4 to 0 V. (g) Photograph of the In<sub>2</sub>O<sub>3</sub> biosensors attached onto an eyeball replica. (h) Real-time glucose-sensing results on an artificial eyeball. (i) Real-time glucose sensing with real sweat collected from human subjects. (j) Glucose-sensing results of real sweat collected before and after a glucose beverage intake. Reproduced from Liu, Q.; Liu, Y.; Wu, F.; Cao, X.; Li, Z.; Alharbi, M.; Abbas, A. N.; Amer, M. R.; Zhou, C. Highly Sensitive and Wearable In<sub>2</sub>O<sub>3</sub> NR Transistor Biosensors with Integrated On-Chip Gate for Glucose Monitoring in Body Fluids. ACS Nano 2018, 12 (2), 1170–1178 (ref 211). Copyright 2018 American Chemical Society.

interactions toward Cu phage, increased the number of electroactive sites, accelerated charge transfer rate, and boosted the sensing performance. The proposed biosensor exhibited an accurate detection of L-cysteine in a human serum sample.

An ascorbic acid (AA) electrochemical sensor based on densely grown  ${\rm RuO_2}$  NWs on  ${\rm TiO_2}$  nanofibers was reported by Kim et al. The amperometric response of  ${\rm RuO_2/TiO_2}$  nanofibers at the applied potential of 0.018 V exhibited a high sensitivity (268.2  $\mu{\rm A}$  mM<sup>-1</sup> cm<sup>-2</sup>), low detection limit (<1.8  $\mu{\rm M}$ ), and exclusive selectivity over common biological interferences at their physiological levels. Moreover, the proposed electrode was successfully applied in real-time analysis of AA concentration from a living rat liver, which suggests the potential application of  ${\rm RuO_2/TiO_2}$  nanofibers in various complex biological/physiological samples for AA monitoring.

An electrochemical sensor based on Ag nanoparticles anchored onto CuO porous nanobelts (Ag/CuO) was constructed for the ultrasensitive determination of dopamine.  $^{206}$  Owing to the participation of the Ag(0)/Ag(I) cycle, Ag nanoparticles significantly enhanced the electrocatalytic

activity toward dopamine and exhibited an outstanding detection limit of 7.0 nM as well as a linear range from 0.04 to 10  $\mu$ M. Meanwhile, they exhibited high selectivity toward dopamine in the presence of a 100-fold excess of ascorbic acid, uric acid, and other physiological interferences, showing a promise for the detection of dopamine in real-sample analysis.

Potassium is an important body mineral that controls the cellular and electrical functions of the body. Abnormally low levels of potassium ions increase the risk of cardiovascular disease, weaken bone health, and induce hypokalemia. Ahn et al.  $^{220}$  reported a nonenzymatic potassium ion sensor based on  $\alpha\textsc{-MnO}_2$  nanorods. The  $\alpha\textsc{-MnO}_2$  nanorods showed well-crystalline nanostructures with an average length of 210 nm. Their reduced size offered an enhanced surface area, good electrochemical activity, and fast electron transfer to catalyze potassium ions and contributed to the sensor's good performance.

FETs. Although MOS NWs are widely used in gas sensors, these are usually operated using a two-terminal chemiresistor mode with no gate electrode. Metal oxide NWs exhibit more active sites per unit volume compared with thin films, and they

Table 5. Conductive Polymer NW Sensors

material	synthetic method	mechanism	category	analyte	LOD and sensing range <sup>b</sup>	response time $^c$	ref
PAni	inkjet printing	CR	gas	NH <sub>3</sub>	5 ppm 5–200 ppm	112 s	238
PEDOT:PSS	direct writing	n/a	n/a	n/a	n/a	n/a	232
PPy	chemical oxidative polymerization	Cr	gas	DMMP	0.5 ppb 0.1-100 ppb	$t_{90,\mathrm{res}} = 40 \text{ s}$	244
PPy	chemical oxidative polymerization	FET	bio	DA	100 pM 0.1 nM−10 μM	n/a	240
PEDOT:PSS	SNIL	CR	gas	$NH_3$	100 ppb (theoretical calc) 0.75–6 ppm	for 3 ppm NH <sub>3</sub> : $t_{90,res} = 70 \text{ s}$	227
						$t_{10,\text{rec}} = 276 \text{ s}$	
PEDOT:PSS	NAMIC and SNIL	CR	gas	NH <sub>3</sub> , NO <sub>2</sub>	NH <sub>3</sub> : 150 ppb	for 60 ppm NH <sub>3</sub> : $t_{90,res} = 57 \text{ s}$	237
					4-60 ppm		
					NO <sub>2</sub> : 6 ppb	n/a for NO <sub>2</sub>	
					4-60 ppm		
P3MT	electrochemical oxidative	Opt	bio	thrombin	10 pM	n/a	223
	polymerization				10 pM-100 nM		
PPy	chemical oxidative polymerization	CR	bio	CRP	$9.61 \times 10^{-18} \text{ M}$ $10^{-20} - 10^{-6} \text{ M}$	19 min	86
Pd-PAni	electrochemical oxidative	CR	gas	$NH_3$	10 ppm	resp time: 200-750 s	224
	polymerization			-	10-500 ppm	rec time: 650-950 s	
P3HT	LB-nTM	FET	gas	$NH_3$	8 ppb	n/a	230
					0-25 ppm		
PAni-TiO <sub>2</sub>	chemical oxidative	EC	bio	lactate	0.15 μM	n/a	259
	polymerization				$0-210 \ \mu M$		
PPy	electrochemical oxidative	EC	bio	DA	33 nM	n/a	243
	polymerization				$5 \times 10^{-8} - 1 \times 10^{-4} \text{ M}$		
PEDOT-coated	CVD and oCVD	CR	gas	$C_5H_{12}$	50 ppm	$t_{90,\text{res}} = 230 - 584 \text{ s}$	48
CNT					700-7000 pm	$t_{10,\text{rec}} = 226 - 374 \text{ s}$	
PPy/SWCNT/Ag	chemical oxidative polymerization	CR	gas	$NH_3$	1 ppm 1–5 ppm	$t_{90,\text{res}} = 25 \text{ s}$	260
PEGylated PAni	electrochemical oxidative	EC	bio	BRCA1	0.0038 pM	10 min	242
1 Edylated 17th	polymerization	LC	Dio	DICCITI	0.01 pM-50 nM	10 11111	212
biotin-doped	SNIL	EC	bio	PSA, E. coli	•	10 min	261
PEDOT:PSS		20		, 2. 0011	10 pg mL <sup>-1</sup> -50 ng mL <sup>-1</sup>		201
					E. coli: $10 \text{ CFU mL}^{-1}$		
					10–10 <sup>6</sup> CFU mL <sup>-1</sup>		
					10 10 CI C IIIL		

"Abbreviations: CR = chemiresistive, FET = field-effect transistor, OFET = organic field-effect transistor; EC = electrochemical, Opt = optical-based, BRCA1 = breast cancer susceptibility gene, CNT = carbon nanotube, CRP = C-reactive protein, CVD = chemical vapor deposition, DA = dopamine, DMMP = dimethyl methylphosphonate, *E. coli = Escherichia coli* bacteria, LB-nTM = liquid-bridge-mediated nanotransfer molding, NAMIC = nanomolding in capillaries, oCVD = oxidative chemical vapor deposition, P3HT = poly(3-hexylthiophene), P3MT = poly(3-methylthiophene), PAni = polyaniline, PEDOT:PSS = poly(3,4-ethylenedioxythiophene):polystyrene sulfonate, PEG = polyethylene glycol, PSA = prostate-specific antigen, SNIL = soft nanoimprint lithography, and SWCNT = single-walled carbon nanotube. <sup>b</sup>The limit of detection (LOD) and sensing range reported in this table are as reported from calibration curves or the main text from the original reference. <sup>c</sup>For gas sensors,  $t_{90,res}$  is defined as the time to reach 90% of the total, maximum signal, and  $t_{10,rec}$  is defined as time required for the signal to drop to 10% of the stabilized response. If a simple time is reported, it is either a response time for a gas sensor as reported by the authors or the time elapsed before taking a measurement. If response and recovery times were not explicitly stated in the original text, it was roughly estimated from real-time response curve figures in the text.

have more oxygen vacancies and interface trap states, all of which cause poor positive bias stress stability and severely restrict the electrical properties of NW FETs.  $^{165}$  To overcome this and control the level of oxygen vacancies in the nanofibers, oxygen vacancy suppressors are used to optimize the stability and electrical characteristics of metal oxide-based 1D FETs. Jun et al.  $^{165}$  reported an ethanol gas sensor based on Yb-doped In<sub>2</sub>O<sub>3</sub> (InYbO) NF FETs. Due to the low standard electrode potential of Yb, it tends to easily bond with O, leading to lower oxygen vacancies in the  $\rm In_2O_3$  nanofibers and enhancing the bias-stress stability.

1D metal oxide FET biosensors have also stimulated a lot of interest. In<sub>2</sub>O<sub>3</sub> NR FET sensors have been shown to have a

high sensitivity, fast response, and good anti-interface capability, which makes them well-suited for analyzing urgent medical conditions such as heart attacks. Liu et al. demonstrated a facile lithography-free process with a shadow mask for the fabrication of highly sensitive  $\rm In_2O_3$  NR FET biosensors. Combined with electronic enzyme-linked immunosorbent assays for signal amplification, the  $\rm In_2O_3$  NRs were optimized for the detection of cardiac biomarkers like cardiac troponin I (cTnI), creatine kinase MB (CK-MB), and B-type natriuretic peptide (BNP) with high sensitivity and reusability.

Current FET biosensors are created by using floating Ag/AgCl electrodes to set the operational point, which have prevented their practical application in medical and health

monitoring. To overcome this and simplify electrode preparation, Liu et al.<sup>211</sup> proposed a straightforward two-step shadow mask fabrication that was successfully used to fabricate In<sub>2</sub>O<sub>3</sub> FET-based wearable biosensors with on-chip gold side gate electrodes. The fabrication of these is accomplished as follows: First, a shadow mask is used to define the sputtercoating of In<sub>2</sub>O<sub>3</sub> NRs (Figure 10a); then, a second shadow mask is used for metal deposition of the source, drain, and side gate. The source and drain electrodes are modified with enzyme glucose oxidase (GO<sub>x</sub>), biocompatible polymer chitosan, and single-walled carbon nanotubes (SWCNTs) using inkjet printing (Figure 10b). The gold-side gated In<sub>2</sub>O<sub>3</sub> FETs show good electrical performance on highly flexible substrates (Figure 10c-f). The optimized glucose sensors show a very wide detection range and detection limits down to 10 nM as well as good performance in human body fluids, such as tears and sweat (Figure 10g-j), which indicate a great potential to work as indispensable components for wearable healthcare electronics. In their latest work, they reported flexible In<sub>2</sub>O<sub>3</sub> NR FET arrays fabricated on PET substrates using shadow mask patterning techniques.<sup>221</sup> Real-time detection of serotonin and dopamine was achieved by immobilizing recently identified high-affinity nucleic acid aptamers on individual In2O3 NR devices. With a detection limit of 10 fM and wide detection range, this sensor is expected to advance our understanding of the brain and other biological systems.

A high-performance FET biosensor based on Al functionalized  $\beta\text{-Bi}_2\text{O}_3$  nanofibers for highly selective and rapid detection of serotonin was reported by Veeralingam et al. Owing to the excellent electrochemical properties of the distributed multidimensional surface and the back-gate electrode-based control of the Debye screening length, the BioFET exhibited an excellent sensitivity of 51.64  $\mu\text{A/nM}$  toward serotonin with a detection limit of 0.29 nM. Furthermore, the real-time detection of the sensor was successfully conducted in urine samples, indicating a promising application in point-of care diagnostics.

Outlook on Metal Oxide NW Sensors. Metal oxide NWs have cemented their place in sensing applications, particularly MOS NW sensors. It is exciting to see the advent of unique morphological nanostructures displaying lower detection limits, higher selectivity toward target analytes, rapid response/recovery times, and remarkable humidity resistance. There are several aspects that push the boundaries of future work: the opportunity to perform advanced calculations on surface energies to predict material-target analyte compatibility with the rise of immense computational power; 164,173 tunable synthetic strategies that allow tight dimensional control and offer the ability to investigate how defects in metal oxide NW sensors affect performance; 173 the integration of a wider range of heterostructures like the vast number of MOF families into the MOS NWs for ameliorated selectivity and sensitivity.14

## ■ CONDUCTING POLYMER NWs AND NFs

Electronically conducting polymers (CPs) have attracted the attention of analytical chemists since the discovery of polyacetylene in the 1970s by Hideki Shirakawa, Alan Heeger, and Alan MacDiarmid and co-workers. Reversible electrochemical oxidative or reductive doping of these polymers, conveniently carried out electrochemically, provides one unique advantage relative to conventional inorganic semi-

conductors (Table 5). Here, we discuss one-dimensional structures (NWs, NRs, NTs, etc.) composed of CPs for sensing applications.

Synthesis of 1D Structures with Conducting Polymers. In the case of the most common class of CPs, the poly(heterocycles) (e.g., poly(thiophene), poly(pyrrole)), the synthesis of films involves the chemical or electrochemical oxidation of the corresponding monomer. With a few exceptions, the resulting polymers are insoluble in any solvents, limiting the methods that can be used for preparing 1D fibers or wires.

Electrochemical Methods. Templates are often used in conjunction with electrodeposition to obtain nanofibers or NWs of CPs, an idea first demonstrated in the mid-1980s. In one recent example, Cui et al.<sup>223</sup> fabricated a polythiophene single NW for the detection of proteins. In this work, traditional electrochemical oxidative polymerization of poly-(3-methylthiophene) (P3MT) was performed on a nanoporous anodic alumina template with tetrabutylammonium trifluoromethanesulfonic acid (TBACF<sub>3</sub>SO<sub>3</sub>) as the dopant. The template was then etched away, and the surface of the single P3MT NW was functionalized with an appropriate aptamer for biorecognition. When the electrostatic interaction between the sulfonate (SO<sub>3</sub><sup>-</sup>) group on the dopant and the terminal amine on the modified aptamer was exploited, the surface of the single NW was trivially modified.

Meanwhile, the modification of CP surfaces has been shown to be straightforward to improve the sensing performance by other methods as well. Hien et al. 224 demonstrated the electrochemical fabrication of Pd-modified poly(aniline) (PANI) NWs to detect ammonia. A three-electrode electrochemical cell contained aniline monomer along with sulfuric acid for the synthesis of PANI nanowires. These NWs were then decorated by drop-casting a solution containing Pd nanoparticles and leaving them to dry. While the method of electrochemically synthesizing conducting polymers has been around for a while, the modification of the biorecognition elements and then the exploitation of the moieties on the polymer chain or the dopants offer an easy route to adapt CP NWs as needed without a complex or cumbersome modification procedure.

Soft Lithography. Soft lithography, initially described by Xia and Whitesides, <sup>225</sup> offers advantages because of the facile and low-cost nature of the process. Further, soft lithography is well-adapted to patterning organic polymers on the surfaces of other insulators, on which conventional tools such as electron-beam lithography, ion-beam lithography, and focused ion beam deposition are not easily applied.

Nanoimprint lithography (NIL) represents an important and impactful variant of soft lithography. Jiang et al. <sup>226</sup> used NIL to create an array of poly(3,4-ethylene-dioxythiophene)—poly(styrenesulfonate) (PEDOT:PSS) NWs functionalized with self-assembled monolayers (SAMs) for the detection of a low concentration of volatile organic compounds (VOCs). NIL was also used by Tang and co-workers <sup>227</sup> to produce a flexible ammonia sensor, capable of interfacing with a smartphone. Both of these works involved the preparation of parallel nanogrooves by NIL on a flat substrate, such as polydimethylsiloxane (PDMS), which are then soft-bonded onto a substrate creating parallel nanochannels. Finally, drops of an aqueous solution of a soluble CP (e.g., PEDOT:PSS) were applied to the edge of the channels, and the channels were allowed to fill completely. The small amount of

conducting polymer material and the facile and fast nature of producing NWs makes this an easy, high throughput method to produce large arrays of CP nanowires.

Other examples include using liquid-bridge-mediated nanotransfer molding (LB-nTM) during which a polar liquid is used as a bridge to directly transfer various materials from a mold onto a substrate. Initially demonstrated with single-crystal PEDOT exhibiting high conductivity by Cho et al., 229 this method of NW synthesis was used to create a single-crystal P3HT NW organic field-effect transistor (OFET) for ammonia sensing by Mun and co-workers. Using polyurethane acrylate molds created by e-beam lithography, a P3HT ink solution was poured into the mold and brought into contact with the SiO<sub>2</sub>/Si substrate with ethanol acting as the polar liquid mediator, ultimately creating single-crystal P3HT NWs approximately 100 nm in diameter.

Direct Writing Techniques. A well-known direct writing tool is dip-pen nanolithography (DPN).<sup>231</sup> In DPN, a sharpened stylus receives a liquid ink either continuously from a reservoir or intermittently by dipping into a well and transfers this ink by lightly contacting a surface and laterally moving in a programmable path across this surface. An advantage of DPN is that very high aspect ratio structures can be prepared in a highly precise and controlled fashion. However, the minimum attainable lateral dimensions for these structures is frequently limited. A disadvantage shared by all direct-writing tools is that these methods are usually serial in nature and are not easily adaptable to high throughput fabrication of nanostructures at scale.

Zhang et al.<sup>232</sup> used a scanning ion conductance microscope to fabricate PEDOT:PSS pillars in an array format. A micropipette was filled with an aqueous solution of the conducting polymer, and a constant bias was applied between a Pt wire inside the pipet tip and the gold electrode substrate. The fabricated PEDOT:PSS pillars were optimized by varying the pulling speed, pulling time, concentration of the CP solution, and diameter of the micropipette. 232 Zips and coworkers<sup>233</sup> also demonstrated this method with aerosol-jet compatible PEDOT:PSS and multiwalled carbon nanotube composite ink to produce electrode arrays, albeit still on the order of tens of microns in height and length. Wajahat and coworkers<sup>234</sup> demonstrated a similar printing method with a CNT-PVP composite to produce flexible strain sensors. The improvement of direct writing techniques to more widely produce nanometer scale structures could allow facile fabrications of sensors consisting of large arrays of onedimensional structures.

Mechanisms of Transduction in CP NWs and NFs. Chemiresistors. CP-based NW chemiresistive gas sensors exploit two mechanisms for signal transduction: influences of an adsorbed analyte on the electron hopping rate and partial charge transfer between analyte molecules and the CP NW or NF. Many CPs are semicrystalline, containing crystalline domains with high conductivity, embedded within a disordered, glassy matrix of lower conductivity. Electronic conduction in these systems frequently involves variable range hopping of charge carriers between crystalline domains. However, in the presence of adsorbed gas molecules, the electron hopping rate is influenced, resulting in either an increase or decrease in resistance. Further, adsorbed gas molecules can either donate or withdraw electrons from the sensing material leading to the perturbation of the conductive polymer's Fermi level.

For example, PEDOT:PSS is a p-doped semiconductor where the holes on the PEDOT<sup>+</sup> chains are compensated by the sulfonate anions on the PSS<sup>-,235,236</sup> This p-type nature of PEDOT:PSS determines how the resistance will change upon exposure to an analyte of interest. When PEDOT:PSS NWs are exposed to an electron-donating gas such as NH<sub>3</sub>, a transfer of electrons from NH<sub>3</sub> to PEDOT will occur forming NH<sub>3</sub><sup>+</sup> and reducing the hole concentration of the PEDOT, leading to an increase in resistance. The exposure of PEDOT to an electron withdrawing gas such as NO<sub>2</sub> produces the opposite effect. Analogous phenomena occur in other conductive polymers such as PANI and PPy. The electron transfer between NH<sub>3</sub> and PANI results in the emeraldine salt form of PANI becoming dedoped into its emeraldine base form, which is insulating, causing an increase in the observed resistance. <sup>238</sup>

Fermi level modulation is a mechanism invoked in connection with some CP gas sensors. Specifically, when PPy is used to functionalize silicon NWs, a transfer of electrons to the PANI, as required to equalize their Fermi levels, results in the formation of a hole accumulation layer (silicon) and a hole depletion layer (PANI). Upon the introduction of NH<sub>3</sub>, the hole accumulation layer will shrink due to the increased number of electrons, causing increased resistance through the nanowire. <sup>239</sup>

When discussing chemiresistive biosensors, similar phenomena to gas sensors occur where the binding event of a biomolecule to its biorecognition element causes a change in electron density within the polymer, leading to a resistance change. In one unique example, C-reactive protein (CRP) is detected by finding a bioaffinity layer that contains its aptamer, causing a *physical* change in the sensing material. This biosensor consisted of a PPy NW network within a polymeric mesh matrix and relied on a two-step signal transduction cascade. First, the binding of the protein to the aptamer resulted in the shrinkage of the NW network, in-turn, causing the shrinkage of the overall mesh matrix network and the disruption of interchain electrical contacts and leading to an increased resistance. So

OFETs and FET-Based Sensors. Field-effect transistor (FET)-based sensors function by measuring the charge carrier mobility through a channel when an electric field is applied from a gate electrode. As an example, the signal transduction of organic field-effect transistor (OFET)-based sensors for the detection of ammonia can be described as a two-step process: <sup>230</sup> ammonia molecules are adsorbed onto the polymer surface and charge carrier traps and/or the induction of disorder in the electric field, leading to changes in the output current, carrier mobility, and threshold voltage.

FETs and oFETs configured for biodetection, BioFETs, operate under the principle where the FET is gated based upon the changes in the surface potential of a sensing material due to the binding of a target biomolecule, such as a protein or DNA. One recent example entails a p-type liquid-ion gated FET aptasensor for the detection of dopamine, where conductive polymer nanotubes bridging the source and drain electrode were surrounded by phosphate-buffered saline, which served as the electrolyte and liquid-gate for the FET sensor.<sup>240</sup>

Electrochemical Methods. Common electrochemical methods of signal transduction include potentiometric methods, involving a voltage measurement at zero current, amperometric methods, involving the measurement of current at constant voltage, and voltametric methods, in which a current response to a time-varying voltage is measured.<sup>241</sup> Differential pulse

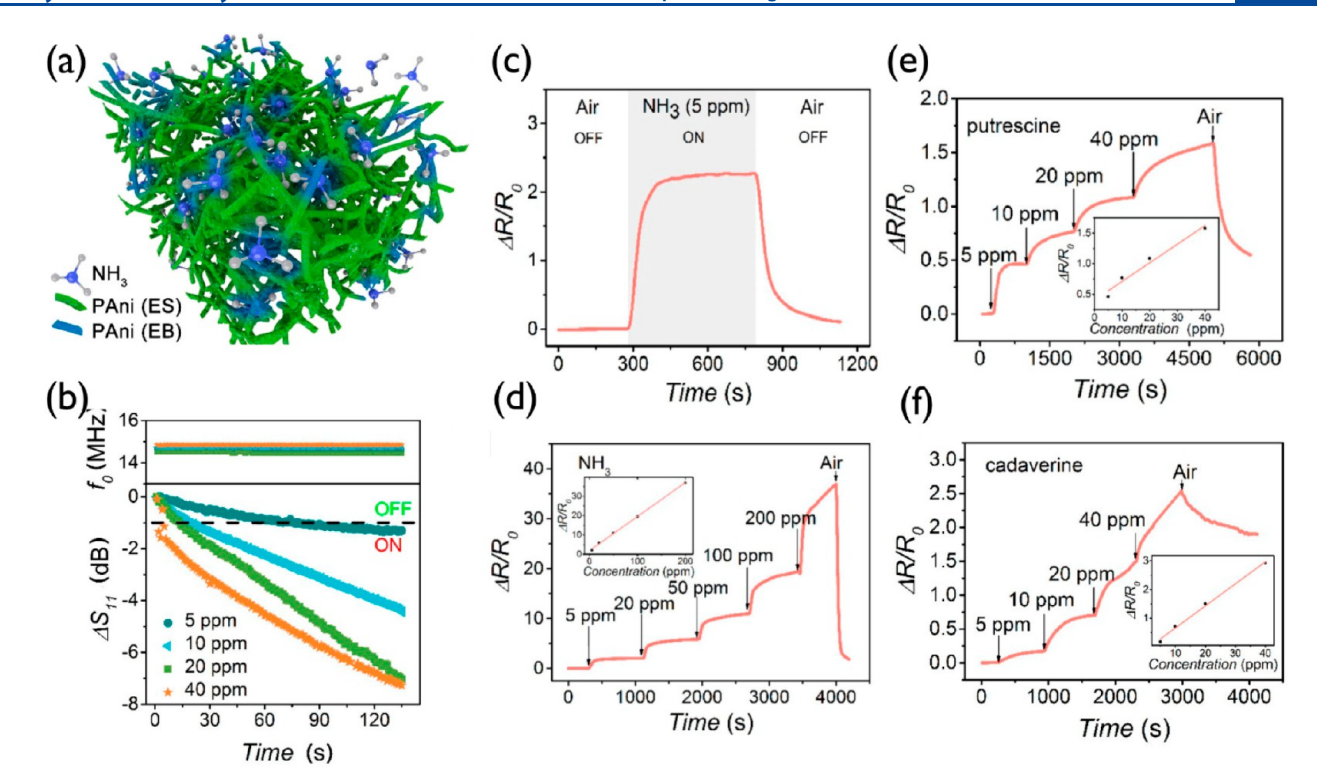


Figure 11. Sensing of biogenic amines using a p-toluene sulfonate hexahydrate—polyaniline hybrid (PTS—PANI). (a) A schematic illustration of the interaction with NH $_3$  gas, where upon exposure, the PTS—PANI will become dedoped into an insulating emeraldine base (EB) form (blue) from its conductive emeraldine salt (ES) form (green). (b) Real time reduced reflection coefficient ( $S_{11}$ ) responses and resonance frequency ( $f_0$ ) to various concentrations of NH $_3$ . (c) Response of PTS—PANI to 5 ppm NH $_3$ . (d) Dynamic responses of PTS—PANI to different concentrations of NH $_3$ . (e) Dynamic responses of PTS—PANI to different concentrations of putrescine. (f) Dynamic responses of PTS—PANI to different concentrations of cadaverine. Reproduced from Ma, Z.; Chen, P.; Cheng, W.; Yan, K.; Pan, L.; Shi, Y.; Yu, G. Highly Sensitive, Printable Nanostructured Conductive Polymer Wireless Sensor for Food Spoilage Detection. *Nano Lett.* **2018**, *18* (7), 4570—4575 (ref 238). Copyright 2018 American Chemical Society.

voltammetry (DPV) is a common voltametric technique where fixed magnitude pulses are superimposed on top of a linear potential ramp. <sup>241</sup> DPV has been used to observe changes in the electrochemical reduction of an indicator, such as methylene blue (MB), upon binding of the biomolecules, <sup>242</sup> and Teng et al. <sup>243</sup> demonstrated the use of DPV to measure the response to varying dose concentrations of dopamine.

Recent Research. Gas Sensing. An innovative device architecture, demonstrated by Ma and co-workers, <sup>238</sup> consisted of a nanostructured CP film configured as a chemiresistor on top of a near-field communication (NFC) transducer, which is a resonant circuit that is planar, flexible, and inexpensive. Nanostructured p-toluene sulfonate hexahydrate-doped polyaniline (PTS-PANI), a sensor for the detection of food spoilage, was demonstrated (Figure 11).<sup>238</sup> The PTS-PANI deposit, consisting of intertwined nanofibers approximately 60 nm in diameter, detected ammonia over a large dynamic range from 5 to 200 ppm and also showed high sensitivities of 225%, 46%, and 17% toward 5 ppm ammonia, putrescine, and cadaverine, respectively.<sup>238</sup> The PTS-PANI nanofibers were also used as an on-off switch to gate the NFC with the goal of interfacing with a smartphone that could be used by the consumer to detect food spoilage. In this case, the CP was integrated onto the NFC tag via a facile inkjet process, effectively shorting the NFC coils and leaving the NFC tag in the "off" state. Upon exposure to total volatile basic nitrogen (TVBN), the PANI becomes dedoped, leading to an increase in resistance, eliminating the short circuit and allowing the

NFC tag to be "on" or readable, indicating the presence of TVBN.

Kwon et al.<sup>244</sup> used conducting polymer polypyrrole (PPy) nanotubes functionalized with carboxylic acids to create a sensor capable of detecting the sarin simulant, dimethyl methylphosphonate (DMMP), at sub-0.5 ppb concentrations. Pyrrole and pyrrole-3-carboxylic acid were copolymerized using FeCl<sub>3</sub>, and the resulting copolymer nanotubes were anchored covalently onto the surface of the interdigitated electrode arrays (IDEs). This system produced  $\Delta R/R_0$  of  $\approx 3\%$ upon exposure to 0.5 ppb DMMP while unmodified PPy nanotubes exhibited no response below 10 ppm DMMP.<sup>244</sup> Over a period of 3 weeks, these nanotubes maintained 95% of their initial sensitivity. The sensitivity observed with these nanotubes was directly correlated to the generation of carboxyl groups during the polymerization process, indicating the functionalization of the NWs was crucial in producing a chemiresistive response toward this analyte. The authors propose that hydrogen bonding interactions between the carboxyl group on the surface of the PPy NWs and the phosphoryl group of the DMMP influenced the transport of charge carriers along the polymer backbone, leading to an increase in resistance.<sup>244</sup>

While 1D CP NWs have been shown to perform well as chemiresistive gas sensors, one challenge to commercializing these sensors is large-scale fabrication of CP nanowires. Tang et al. 237 demonstrated a facile method for fabricating PEDOT:PSS NWs for gas sensing using NIL of a polymeric

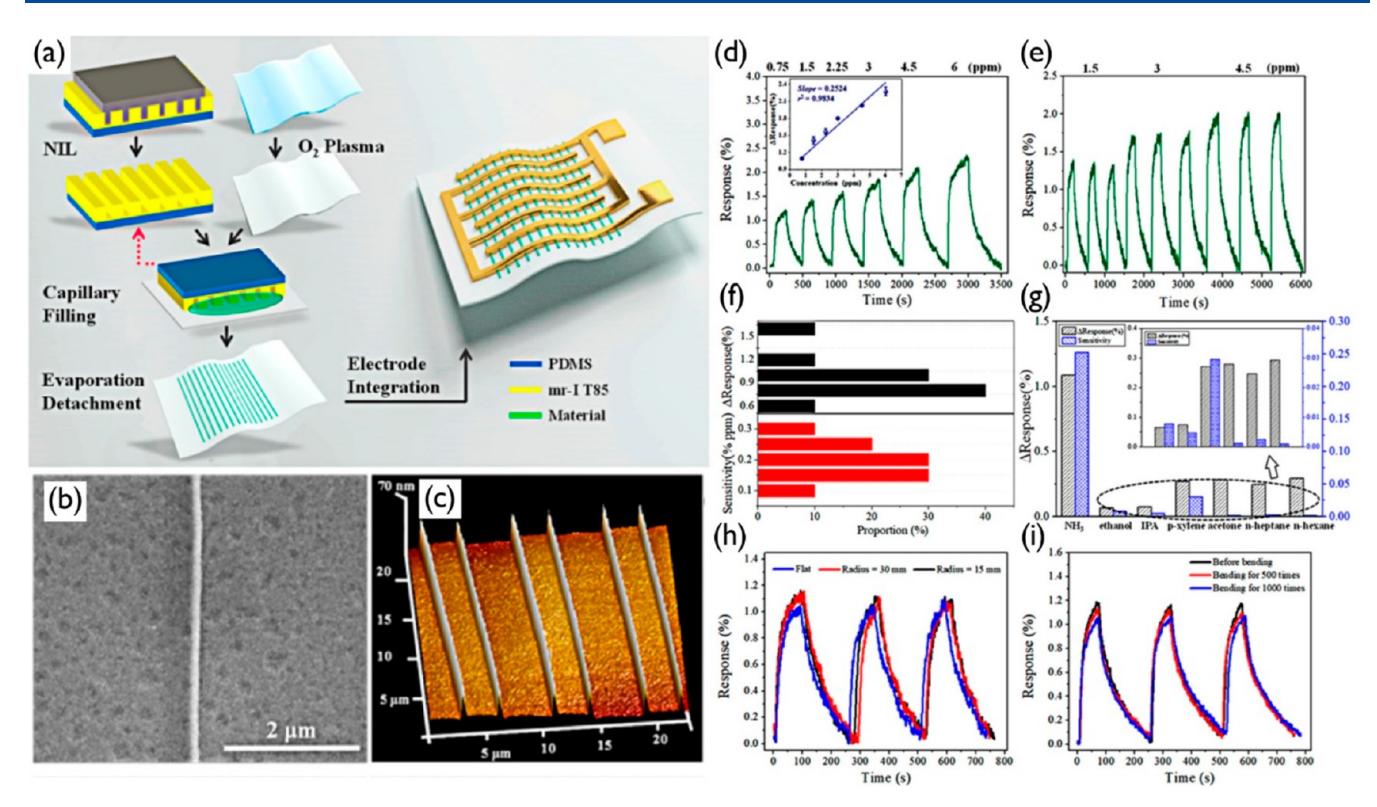


Figure 12. Flexible PEDOT:PSS NW fabrication, characterization, and sensing performance. (a) Schematic of the soft lithography fabrication process for the flexible PEDOT:PSS sensor. (b) Top-view SEM image of an isolated nanowire. (c) 3D AFM image of a NW array. (d) Real-time response of the flexible NW gas sensor to NH<sub>3</sub>. (e) Repeatability of responses for one NW sensor toward different concentrations of NH<sub>3</sub>. (f) Distributions of the responsivity at 0.75 ppm NH<sub>3</sub> and the sensitivity of ten different sensors. (g) Responsivity and sensitivity to different gases (NH<sub>3</sub> (0.75 ppm), ethanol (15 ppm), IPA (11.2 ppm), p-xylene (2.3 ppm), n-heptane (11.9 ppm), n-hexane (39.8 ppm), and acetone (60 ppm)). (h) Response curves to 1.5 ppm NH<sub>3</sub> at various bending radii. (i) Response curve to 1.5 ppm NH<sub>3</sub> before and after bending 500 and 1000 times with a bending radius of 15 mm. Reproduced from Tang, N.; Zhou, C.; Xu, L.; Jiang, Y.; Qu, H.; Duan, X. A Fully Integrated Wireless Flexible Ammonia Sensor Fabricated by Soft Nano-Lithography. ACS Sensors 2019, 4 (3), 726–732 (ref 227). Copyright 2019 American Chemical Society.

mold coupled with capillary filling to produce linear nanowire arrays. These arrays functioned as chemiresistors. Exposure to  $\mathrm{NH_3}$  and  $\mathrm{NO_2}$  showed linear resistance responses and LODs of 150 and 6 ppb for these two gases, respectively. Signal stability, monitored over a period of 60 days, showed a loss of 40% of the initial sensor signal amplitude.

Using the same soft lithographic process (Figure 12), Tang et al.  $^{227}$  synthesized arrays of PEDOT:PSS NWs on a flexible, polyethylene terephthalate substrate and demonstrated a LOD of 0.75 ppm for ammonia, a rapid response in the 50–70 s range, and significant selectivity. Repetitive bending tests were performed at a bending radius of 5 mm where simulations showed the maximum strains for the device and exhibited virtually no change in the  $\Delta R/R_0$  value over 1200 cycles. With regard to sensing performance, this flexible NW sensor exhibited a dynamic linear range from 0.75 to 6 ppm and took 70 s to reach 90% of the maximum response signal at 3 ppm ammonia.

Mun and co-workers<sup>230</sup> developed a single-crystal ammonia gas sensor using poly(3-hexylthiophene) (P3HT) NWs as an OFET. When a single-crystal P3HT NW is synthesized as the channel, the sensor can exhibit high charge carrier mobility as well as a high current signal imparted by an efficient charge carrier transport due to the lack of defects in a single crystal that form charge traps. These NWs exhibited an extremely high field-effect mobility, especially when compared to their thin-film counterparts (0.93 vs 0.008 cm<sup>2</sup> V<sup>-1</sup> s<sup>-1</sup>), as well as high on/off currents, suggesting good ammonia sensing

performance.<sup>230</sup> The created ammonia response curve demonstrated a LOD of 8 ppb.<sup>230</sup> However, the concentration calibration curve for the sensor shows a saturation behavior that restricts its dynamic range, an issue that may be correctable in future work. Ultimately, the use of single-crystalline P3HT NWs improved two key performance metrics for ammonia detection, providing motivation for investigating single crystalline NWs in other gas sensing systems.

Combinations of nanomaterials operating in parallel provide opportunities for expanded dynamic range and enhanced sensitivity. Wang and co-workers<sup>48</sup> developed a novel hybrid sensing material using both CNTs and CPs, featuring PEDOT synthesized on top of vertically aligned CNTs (VA-CNTs) to improve performance for the detection of nonpolar VOCs. In this work, an 8 nm PEDOT layer was synthesized on top of VA-CNTs using the oxidative chemical vapor deposition (oCVD) technique, resulting in an 8-fold increase in signal compared to bare VA-CNTs with an excellent signal-to-noise ratio (S/N), comparable to typical metal nanoparticle chemresistors. 48 Interestingly, an additional layer of insulating polystyrene (PS) was coated onto the VA-CNT/PEDOT structure, resulting in 2-times longer response time ( $t_{90}$ , time required to reach 90% of total signal) but a sensitivity that was approximately 3-times larger than without the layer of PS. 48 The enhancement of performance achieved using this hybrid nanomaterial, including fast response/recovery, high selectivity, and superb signal-to-noise ratio, provides motivation for the exploration of this paradigm in other systems.

Biological Sensing. Sensors that exploit single NWs, as opposed to ensembles of many NWs, are challenging to fabricate but also afford opportunities to precisely isolate key variables in sensor performance such as nanostructure dimensions, composition, and functionalization. A deeper understanding of the function of these systems can thereby be achieved. Cui et al. 223 functionalized a single P3MT NW to demonstrate a method of detecting the protein thrombin using the phase transitions that are induced at P3MT nanowires functionalized with the thrombin aptamer. 223 Using a combination of the Raman signal and photoluminescence (PL), the conformational states of the P3MT NW were probed, and a 55-fold enhancement of the Raman signal was observed in the presence of thrombin. Increases in the P3MT crystallinity also resulted in a 37-fold increase in the PL intensity. This work demonstrated the viability of using the optical properties of conductive polymer NWs for the selective and sensitive detection of biomolecules.

Polypyrrole (PPy) nanotubes were functionalized with carboxyl groups by Park et al.<sup>240</sup> to detect dopamine using a liquid-ion gated FET sensor. The interdigitated microelectrodes (IMEs) and carboxylated PPy nanotubes were synthesized using a process similar to that employed for the gas sensing work discussed above. The key difference was an additional modification step where a condensation reaction takes place in the presence of 4-(4,6-dimethoxy-1,3,5-triazin-2yl)—4-methyl-morpholinium chloride (DMT-MM) to perform a chemical conjugation between the PPy nanotubes and dopamine-specific aptamer. These nanotubes have a LOD of 100 pM in the presence of other neurotransmitters such as serotonin and norepinephrine. The first demonstration of a liquid-gated FET aptasensor showed the application of this sensor architecture in conjunction with a versatile method of CP nanotube synthesis for the detection of a common neurotransmitter.

Lin and co-workers <sup>86</sup> created a mesh architecture consisting of a polymeric matrix of acrylamide (AM), methylenebis-(acrylamide) (MBAA), N-Isopropylacrylamide (NIPAAm), and C-reactive protein (CRP)/CRP—aptamers complex and then synthesized PPy NFs within this matrix in situ for the purpose of detecting CRP, a possible biomarker for melanoma. Using these flexible sensors, CRP concentrations down to a LOD of  $7.8 \times 10^{-19}$  M or  $9.0 \times 10^{-17}$  g mL<sup>-1</sup> were detected. <sup>86</sup> The PPy nanofibers forming the conductive network within the polymer matrix were a decisive factor enabling this performance.

An ubiquitous problem in the development of biosensors is nonspecific adsorption onto the bioaffinity layer of the biosensor. To thwart nonspecific adsorption, Hui and coworkers<sup>242</sup> grafted polyethylene glycol (PEG) onto PANI nanofibers to develop a sensitive electrochemical biosensor for the breast cancer susceptibility gene, BRCA1. Typically, the grafting of antifouling polymers like PEG, which are nonconductive, lead to a decrease in sensitivity due to the formation of interfaces with high impedance. However, in this case, a good electrochemical performance was obtained in concert with strong antifouling behavior as differential pulse voltammetry (DPV) measurements show the nanofibers retaining 92.17% of their initial current signal even after incubation in 100% serum. 242 DPV was used to transduce the hybridization reaction between the capture DNA immobilized on the surface of the NF and the target BRCA1 using methylene blue (MB) as an indicator, and a decrease of the

well-defined DPV peaks (indicating electrochemical reduction of MB) occurring at around -0.31~V (vs Ag/AgCl) was observed after the introduction of BRCA1. The interaction between MB and the DNA backbone was suggested to be a reason for the decrease in the reduction current of MB. Calibration curves showed a wide linear range between 0.01 pM and 1 nM with a LOD of 0.0038 pM. This PEGylated PANI NF sensor proved to be a novel, ultrasensitive device capable of accurate operation in complex media.

#### CONCLUDING REMARKS

Twenty years since the introduction of new synthetic tools for making single NW chemical sensors, the interest and creativity of analytical chemists working with 1D systems has been sustained, even in the face of distractions in the form of newer 2D materials. On the contrary, this article highlights many new and exciting advances and applications. Innovation is evident in a range of new synthetic methods that have been developed for preparing 1D materials and for elaborating them with protective layers, filtering layers, receptors, and catalysts that amplify or modify sensing performance. Barriers impeding progress, such as Debye length limitations in the case of biosensors operating in high ionic strength solutions, have been investigated and mitigated to a great extent, but plenty of room for further advances remains, as few commercial successes for sensors based upon 1D materials have so far been realized. We hope and expect that this part of the story will change in the ensuing 20 years.

### AUTHOR INFORMATION

#### **Corresponding Author**

Reginald M. Penner — Department of Chemistry, University of California, Irvine, Irvine, California 92697, United States;
orcid.org/0000-0003-2831-3028; Email: rmpenner@

## **Authors**

Joshua M. Ziegler — Department of Chemistry, University of California, Irvine, Irvine, California 92697, United States Ilektra Andoni — Department of Chemistry, University of California, Irvine, Irvine, California 92697, United States Eric J. Choi — Department of Chemistry, University of California, Irvine, Irvine, California 92697, United States

Lu Fang – Department of Automation, Hangzhou Dianzi University, Xiasha, Hangzhou 310018, China

Heriberto Flores-Zuleta – Department of Chemistry, University of California, Irvine, Irvine, California 92697, United States

Nicholas J. Humphrey – Department of Chemistry, University of California, Irvine, Irvine, California 92697, United States

Dong-Hwan Kim — School of Chemical Engineering, Sungkyunkwan University, Jangan-gu Suwon, Gyeonggi-do 16419, South Korea; o orcid.org/0000-0002-2753-0955

Jihoon Shin — School of Chemical Engineering, Sungkyunkwan University, Jangan-gu Suwon, Gyeonggi-do 16419, South Korea

Hyunho Youn — School of Chemical Engineering, Sungkyunkwan University, Jangan-gu Suwon, Gyeonggi-do 16419, South Korea

Complete contact information is available at: https://pubs.acs.org/10.1021/acs.analchem.0c04476

#### Notes

The authors declare no competing financial interest.

#### **Biographies**

Joshua M. Ziegler is a Ph.D. candidate in the Department of Chemistry at the University of California, Irvine. Joshua received a B.S. in Chemistry with a minor in Materials Science from Western Washington University in 2015. During his time at Western, he studied electrocatalysis and synthetic inorganic chemistry in the lab of Professor John Gilbertson. Josh is now at UCI studying electrochemistry under Professor Reginald M. Penner. His research focuses on understanding the degradation of electrochemical energy storage materials.

Ilektra Andoni is a graduate student in the Department of Chemistry at the University of California, Irvine (UCI). Ilektra received a B.S. in Biochemistry in 2017 from Boston College in Chestnut Hill, MA. During that time, Ilektra studied core—shell metal nanoparticles for heterogeneous electrochemical catalysis with Prof. Frank Tsung. She is now pursuing a Ph.D. with a focus on the pseudocapacitive energy storage behavior of niobium oxide nanowires.

Eric J. Choi is a Ph.D. candidate in the Department of Chemistry at the University of California, Irvine (UCI). He received his A.B. in Chemistry from Washington University in St. Louis in 2016, where he developed solid-state NMR instrumentation and methods with Professor Alexander B. Barnes. Eric's current graduate research centers on the intersection of electrochemistry, materials, and biosensing under the guidance of Professor Reginald M. Penner.

Lu Fang received her Ph.D. degree in Biomedical Engineering at Zhejiang University in 2014 and is currently a lecturer in the Department of Automation in Hangzhou Dianzi University in China. Her research interests are mainly in the area of electrochemical biosensors for the diagnosis of disease and health maintenance, including wearable and implantable biosensors for continuous physiological monitoring and sensors for clinical use at the point-of-care.

Heriberto Flores-Zuleta received a B.S. degree in Chemistry from the University of Illinois at Urbana—Champaign where he studied the Li<sup>+</sup> intercalation kinetics and dynamics in graphene with scanning electrochemical microscopy under Professor Joaquin Rodriguez-López. He joined the Department of Chemistry at the University of California, Irvine in 2019 as a doctoral student where he is investigating electrodeposited nanomaterials for reversible Na<sup>+</sup> energy storage.

Nicholas J. Humphrey is a graduate student in the Department of Chemistry at the University of California, Irvine (UCI). He received a B.A. in Biochemistry from Colorado College in 2019, where he developed a bipolar electrochemical sensor for aqueous lead detection in Professor Eli Fahrenkrug's research lab. Nicholas' current research at UCI focuses on nanomaterial-based hydrogen sensors under the guidance of Professor Reginald M. Penner.

Dong-Hwan Kim, Richie, received his Ph.D. in 2005 from University of Michigan and moved to Duke University for his postdoctoral training. He had a tenured faculty appointment in the School of Chemical and Biomolecular Engineering at Nanyang Technological University before he joined Sungkyunkwan University (SKKU) in 2015. He is currently a full professor in the School of Chemical Engineering at SKKU. Prof. Kim has been the director of the Precision Biology Research Center, SKKU, since 2018 and the director of Global Talent Fostering Program, SKKU, since 2019. His current research interest focuses on optical materials and nanoassemblies for bioanalytical platforms.

Jihoon Shin is a postdoctoral researcher in the research group of Prof. Dong-Hwan Kim at Sungkyunkwan University in South Korea. He received his Ph.D. degree in Nanoscience from Sungkyunkwan University in 2014. His research interests are in the area of experimental nanobiology. More specifically, he is interested in creating DNA assemblies that facilitate communication between external stimuli and biomolecules for the ultimate purpose of diagnostic/therapeutic applications.

Hyunho Youn graduated from Sungkyunkwan University, South Korea, with a Master's degree in Polymer Engineering in 2016. He is currently working on his Ph.D. in Chemical Engineering at the same university, and his research focuses on chemical and biological sensors based on localized surface plasmon resonance and electrochemical impedance spectroscopy.

Reginald M. Penner is an electrochemist who received a B.A. degree in Chemistry and Biology from Gustavus Adolphus College and a Ph.D. with Charles Martin at Texas A&M University. He studied with Nate Lewis as a postdoctoral fellow at Stanford and Caltech and joined the Department of Chemistry at University of California, Irvine in 1990. His research group investigates electrochemical methods for preparing nanomaterials and studies applications for these nanomaterials in sensors, energy storage, and photonic devices. He is the Chancellor's Professor in the Department of Chemistry and Associate Dean for Research and Innovation in the School of Physical Sciences at UC Irvine.

#### ACKNOWLEDGMENTS

The financial support of the National Science Foundation through grant NSF CBET 1803314 is gratefully acknowledged.

## REFERENCES

- (1) Kong, J.; Franklin, N. R.; Zhou, C.; Chapline, M. G.; Peng, S.; Cho, K.; Dai, H. Science (Washington, DC, U. S.) 2000, 287 (5453), 622–625.
- (2) Favier, F.; Walter, E. C.; Zach, M. P.; Benter, T.; Penner, R. M. Science (Washington, DC, U. S.) 2001, 293 (5538), 2227-2231.
- (3) Cui, Y.; Wei, Q.; Park, H.; Lieber, C. M. Science (Washington, DC, U. S.) 2001, 293 (5533), 1289-1292.
- (4) Johnson, J. L.; Behnam, A.; Pearton, S. J.; Ural, A. Adv. Mater. 2010, 22 (43), 4877–4880.
- (5) Kumar, R.; Goel, N.; Kumar, M. Appl. Phys. Lett. 2018, 112 (5), 053502.
- (6) Levitt, A.; Seyedin, S.; Zhang, J.; Wang, X.; Razal, J. M.; Dion, G.; Gogotsi, Y. Small **2020**, 16 (26), 2002158.
- (7) Sharma, S.; Chhetry, A.; Sharifuzzaman, M.; Yoon, H.; Park, J. Y. ACS Appl. Mater. Interfaces 2020, 12 (19), 22212–22224.
- (8) Ding, B.; Wang, M.; Wang, X.; Yu, J.; Sun, G. Mater. Today **2010**, 13 (11), 16–27.
- (9) Jolly, A.; Miao, D.; Daigle, M.; Morin, J. Angew. Chem. **2020**, 132 (12), 4652–4661.
- (10) Rezapour, M. R.; Myung, C. W.; Yun, J.; Ghassami, A.; Li, N.; Yu, S. U.; Hajibabaei, A.; Park, Y.; Kim, K. S. ACS Appl. Mater. Interfaces 2017, 9 (29), 24393–24406.
- (11) Jariwala, D.; Sangwan, V. K.; Lauhon, L. J.; Marks, T. J.; Hersam, M. C. ACS Nano 2014, 8 (2), 1102–1120.
- (12) Tan, W. C.; Wang, L.; Feng, X.; Chen, L.; Huang, L.; Huang, X.; Ang, K.-W. W. Adv. Electron. Mater. 2019, 5 (2), 1800666.
- (13) Abbas, A. N.; Liu, B.; Chen, L.; Ma, Y.; Cong, S.; Aroonyadet, N.; Köpf, M.; Nilges, T.; Zhou, C. ACS Nano 2015, 9 (5), 5618–5624
- (14) Li, X.; Wang, X.; Zhang, L.; Lee, S.; Dai, H. Science (Washington, DC, U. S.) 2008, 319 (5867), 1229-1232.
- (15) Jiao, L.; Zhang, L.; Wang, X.; Diankov, G.; Dai, H. Nature 2009, 458 (7240), 877-880.
- (16) Iijima, S. Nature 1991, 354 (6348), 56-58.

- (17) Guo, T.; Nikolaev, P.; Thess, A.; Colbert, D. T.; Smalley, R. E. Chem. Phys. Lett. **1995**, 243 (1–2), 49–54.
- (18) Cassell, A. M.; Franklin, N. R.; Tombler, T. W.; Chan, E. M.; Han, J.; Dai, H. J. Am. Chem. Soc. 1999, 121 (34), 7975-7976.
- (19) Son, M.; Kim, D.; Park, K. S.; Hong, S.; Park, T. H. Biosens. Bioelectron. 2016, 78, 87-91.
- (20) Park, M.; Kim, H. S.; Kim, T.; Kim, J.; Seo, S.; Lee, B. Y. Sens. Actuators, B 2018, 263, 486-492.
- (21) Li, D.; Wang, C.; Sun, G.; Senapati, S.; Chang, H. C. Biosens. Bioelectron. 2017, 97 (May), 143-149.
- (22) Fu, Y.; Romay, V.; Liu, Y.; Ibarlucea, B.; Baraban, L.; Khavrus, V.; Oswald, S.; Bachmatiuk, A.; Ibrahim, I.; Rümmeli, M.; et al. *Sens. Actuators*, B **2017**, 249, 691–699.
- (23) Xu, X.; Clément, P.; Eklöf-Österberg, J.; Kelley-Loughnane, N.; Moth-Poulsen, K.; Chávez, J. L.; Palma, M. Nano Lett. **2018**, 18 (7), 4130–4135.
- (24) Li, W.; Gao, Y.; Zhang, J.; Wang, X.; Yin, F.; Li, Z.; Zhang, M. *Nanoscale Adv.* **2020**, 2 (2), 717–723.
- (25) Liang, Y.; Xiao, M.; Wu, D.; Lin, Y.; Liu, L.; He, J.; Zhang, G.; Peng, L.-M.; Zhang, Z. ACS Nano 2020, 14 (7), 8866–8874.
- (26) Hersam, M. C. Nat. Nanotechnol. 2008, 3 (7), 387-394.
- (27) Gu, J.; Han, J.; Liu, D.; Yu, X.; Kang, L.; Qiu, S.; Jin, H.; Li, H.; Li, Q.; Zhang, J. Small **2016**, 12 (36), 4993–4999.
- (28) Pohl, H. A. J. Electrochem. Soc. 1968, 115 (6), 155C.
- (29) Wejinya, U. C.; Xi, N.; Lai, K. W. C.; Zhang, J.; Shen, Y. Design and Generation of DEP Force for Assembly of CNT-Based Nano Devices. In 2008 IEEE/RSJ International Conference on Intelligent Robots and Systems, Nice, France, September 22–26, 2008; pp 925–930; DOI: 10.1109/IROS.2008.4651059.
- (30) Monica, A. H.; Papadakis, S. J.; Osiander, R.; Paranjape, M. Nanotechnology 2008, 19 (8), 085303.
- (31) Xiang, C.; Kung, S. C.; Taggart, D. K.; Yang, F.; Thompson, M. A.; Güell, A. G.; Yang, Y.; Penner, R. M. ACS Nano 2008, 2 (9), 1939–1949.
- (32) Li, X.; Le Thai, M.; Dutta, R. K.; Qiao, S.; Chandran, G. T.; Penner, R. M. ACS Sensors 2017, 2 (2), 282–289.
- (33) Seekaew, Y.; Wisitsoraat, A.; Phokharatkul, D.; Wongchoosuk, C. Sensors Actuators, B Chem. **2019**, 279, 69–78.
- (34) Bushmaker, A. W.; Oklejas, V.; Walker, D.; Hopkins, A. R.; Chen, J.; Cronin, S. B. *Nat. Commun.* **2016**, *7*, 10475.
- (35) Kosynkin, D. V.; Higginbotham, A. L.; Sinitskii, A.; Lomeda, J. R.; Dimiev, A.; Price, B. K.; Tour, J. M. *Nature* **2009**, 458 (7240), 872–876
- (36) Lee, H. J.; Lim, J.; Cho, S. Y.; Kim, H.; Lee, C.; Lee, G. Y.; Sasikala, S. P.; Yun, T.; Choi, D. S.; Jeong, M. S.; et al. ACS Appl. Mater. Interfaces 2019, 11 (41), 38006–38015.
- (37) Cai, J.; Ruffieux, P.; Jaafar, R.; Bieri, M.; Braun, T.; Blankenburg, S.; Muoth, M.; Seitsonen, A. P.; Saleh, M.; Feng, X.; et al. *Nature* **2010**, *466* (7305), 470–473.
- (38) Mehdi Pour, M.; Lashkov, A.; Radocea, A.; Liu, X.; Sun, T.; Lipatov, A.; Korlacki, R. A.; Shekhirev, M.; Aluru, N. R.; Lyding, J. W.; et al. *Nat. Commun.* **2017**, 8 (1), 820.
- (39) Shekhirev, M.; Lipatov, A.; Torres, A.; Vorobeva, N. S.; Harkleroad, A.; Lashkov, A.; Sysoev, V.; Sinitskii, A. ACS Appl. Mater. Interfaces 2020, 12 (6), 7392–7402.
- (40) Jiang, X.; Qin, S.; Cao, Y.; Wu, R.; Han, D.; Hua, Z.; Zhu, C.; Huang, X.; Wang, L.; Yang, S. ACS Appl. Nano Mater. **2020**, 3 (4), 3402–3409.
- (41) Cho, K. M.; Cho, S.-Y. Y.; Chong, S.; Koh, H.-J. J.; Kim, D. W.; Kim, J.; Jung, H.-T. T. ACS Appl. Mater. Interfaces 2018, 10 (49), 42905–42914.
- (42) Kumar, D.; Chaturvedi, P.; Saho, P.; Jha, P.; Chouksey, A.; Lal, M.; Rawat, J. S. B. S.; Tandon, R. P.; Chaudhury, P. K. Sens. Actuators, B 2017, 240, 1134–1140.
- (43) Chen, J.; Lotfi, A.; Hesketh, P. J.; Kumar, S. Sens. Actuators, B **2019**, 281, 1080–1087.
- (44) Panes-Ruiz, L. A.; Shaygan, M.; Fu, Y.; Liu, Y.; Khavrus, V.; Oswald, S.; Gemming, T.; Baraban, L.; Bezugly, V.; Cuniberti, G. ACS Sensors 2018, 3 (1), 79–86.

- (45) Xiao, M.; Liang, S.; Han, J.; Zhong, D.; Liu, J.; Zhang, Z.; Peng, L. ACS Sensors 2018, 3 (4), 749–756.
- (46) Gunlycke, D.; Li, J.; Mintmire, J. W.; White, C. T. Nano Lett. **2010**, 10 (9), 3638–3642.
- (47) Sun, Y.; Peng, Z.; Li, H.; Wang, Z.; Mu, Y.; Zhang, G.; Chen, S.; Liu, S.; Wang, G.; Liu, C.; et al. *Biosens. Bioelectron.* **2019**, 137 (April), 255–262.
- (48) Wang, X.; Ugur, A.; Goktas, H.; Chen, N.; Wang, M.; Lachman, N.; Kalfon-Cohen, E.; Fang, W.; Wardle, B. L.; Gleason, K. K. ACS Sensors 2016, 1 (4), 374–383.
- (49) Hwang, S. I.; Franconi, N. G.; Rothfuss, M. A.; Bocan, K. N.; Bian, L.; White, D. L.; Burkert, S. C.; Euler, R. W.; Sopher, B. J.; Vinay, M. L.; et al. *ACS Sensors* **2019**, *4* (8), 2084–2093.
- (50) Ji, S.; Lee, M.; Kim, D. Biosens. Bioelectron. 2018, 102, 345–350.
- (51) Ishihara, S.; Labuta, J.; Nakanishi, T.; Tanaka, T.; Kataura, H. *ACS Sensors* **2017**, 2 (10), 1405–1409.
- (52) Li, Y.; Mann, D.; Rolandi, M.; Kim, W.; Ural, A.; Hung, S.; Javey, A.; Cao, J.; Wang, D.; Yenilmez, E.; et al. *Nano Lett.* **2004**, *4* (2), 317–321.
- (53) Tulevski, G. S.; Franklin, A. D.; Afzali, A. ACS Nano 2013, 7 (4), 2971–2976.
- (54) Tapasztó, L.; Dobrik, G.; Lambin, P.; Biró, L. P. Nat. Nanotechnol. 2008, 3 (7), 397-401.
- (55) Winter, A.; Ekinci, Y.; Gölzhaüser, A.; Turchanin, A. 2D Mater. **2019**, 6 (2), 021002.
- (56) Fox, D. S.; Zhou, Y.; Maguire, P.; Oneill, A.; Ócoileaín, C.; Gatensby, R.; Glushenkov, A. M.; Tao, T.; Duesberg, G. S.; Shvets, I. V.; et al. *Nano Lett.* **2015**, *15* (8), 5307–5313.
- (57) Lee, S.; Yang, F.; Suh, J.; Yang, S.; Lee, Y.; Li, G.; Sung Choe, H.; Suslu, A.; Chen, Y.; Ko, C.; et al. *Nat. Commun.* **2015**, *6* (1), 8573.
- (58) Feng, X.; Huang, X.; Chen, L.; Tan, W. C.; Wang, L.; Ang, K.-W. Adv. Funct. Mater. 2018, 28 (28), 1801524.
- (59) Chen, H.; Huang, P.; Guo, D.; Xie, G. J. Phys. Chem. C 2016, 120 (51), 29491–29497.
- (60) Masih Das, P.; Danda, G.; Cupo, A.; Parkin, W. M.; Liang, L.; Kharche, N.; Ling, X.; Huang, S.; Dresselhaus, M. S.; Meunier, V.; et al. *ACS Nano* **2016**, *10* (6), 5687–5695.
- (61) Li, Q.; Newberg, J. T.; Walter, E. C.; Hemminger, J. C.; Penner, R. M. *Nano Lett.* **2004**, 4 (2), 277–281.
- (62) Li, Q.; Walter, E. C.; Van Der Veer, W. E.; Murray, B. J.; Newberg, J. T.; Bohannan, E. W.; Switzer, J. A.; Hemminger, J. C.; Penner, R. M. J. Phys. Chem. B 2005, 109 (8), 3169–3182.
- (63) Wei, W.; Samad, L.; Choi, J. W.; Joo, Y.; Way, A.; Arnold, M. S.; Jin, S.; Gopalan, P. Chem. Mater. **2016**, 28 (11), 4017–4023.
- (64) Yun, T.; Jin, H. M.; Kim, D.; Han, K. H.; Yang, G. G.; Lee, G. Y.; Lee, G. S.; Choi, J. Y.; Kim, I.; Kim, S. O. *Adv. Funct. Mater.* **2018**, 28 (50), 1804508.
- (65) Hantanasirisakul, K.; Gogotsi, Y. Adv. Mater. 2018, 30, 1804779.
- (66) Li, N.; Jiang, Y.; Zhou, C.; Xiao, Y.; Meng, B.; Wang, Z.; Huang, D.; Xing, C.; Peng, Z. ACS Appl. Mater. Interfaces 2019, 11 (41), 38116–38125.
- (67) Wang, H.; Wu, C.; Huang, Y.; Sun, F.; Lin, N.; Soomro, A. M.; Zhong, Z.; Yang, X.; Chen, X.; Kang, J.; et al. ACS Appl. Mater. Interfaces 2016, 8 (42), 28709–28717.
- (68) Chen, Z. A.; Lu, W.; Bao, C.; Niu, Q.; Cao, X.; Wang, H.; Yao, R. X. Microchim. Acta **2019**, 186 (12), 758.
- (69) Scott, J. A.; Totonjian, D.; Martin, A. A.; Tran, T. T.; Fang, J.; Toth, M.; McDonagh, A. M.; Aharonovich, I.; Lobo, C. J. *Nanoscale* **2016**, 8 (5), 2804–2810.
- (70) Jang, J. S.; Qiao, S.; Choi, S. J.; Jha, G.; Ogata, A. F.; Koo, W. T.; Kim, D. H.; Kim, I. D.; Penner, R. M. ACS Appl. Mater. Interfaces **2017**, 9 (45), 39464–39474.
- (71) Zhai, Q.; Gong, S.; Wang, Y.; Lyu, Q.; Liu, Y.; Ling, Y.; Wang, J.; Simon, G. P.; Cheng, W. ACS Appl. Mater. Interfaces 2019, 11 (10), 9724–9729.
- (72) Guo, Z.; Jia, Y.; Song, X.; Lu, J.; Lu, X.; Liu, B.; Han, J.; Huang, Y.; Zhang, J.; Chen, T. *Anal. Chem.* **2018**, *90* (10), 6124–6130.

- (73) Chen, Y. C.; Hsu, J. H.; Hsu, Y. K. Microchim. Acta 2018, 185 (2), 106.
- (74) Kim, D. H.; Kim, S. J.; Shin, H.; Koo, W. T.; Jang, J. S.; Kang, J. Y.; Jeong, Y. J.; Kim, I. D. ACS Nano **2019**, 13 (5), 6071–6082.
- (75) Vilian, A. T. E.; Kim, W.; Park, B.; Oh, S. Y.; Kim, T. Y.; Huh, Y. S.; Hwangbo, C. K.; Han, Y. K. Biosens. Bioelectron. 2019, 142, 111549.
- (76) Wu, Y.; Jiao, L.; Xu, W.; Gu, W.; Zhu, C.; Du, D.; Lin, Y. Small **2019**, *15* (17), 1900632.
- (77) Yuan, Z.; Chen, J.; Wen, Y.; Zhang, C.; Zhou, Y.; Yang, Z.; Yu, C. Biosens. Bioelectron. **2019**, 145, 111677.
- (78) Liu, L.; Xiang, G.; Jiang, D.; Du, C.; Liu, C.; Huang, W.; Pu, X. *Microchim. Acta* **2016**, *183* (1), 379–387.
- (79) Li, Z.; Gao, F.; Gu, Z. Sens. Actuators, B 2017, 243, 1092-1101.
- (80) Kawamura, G.; Muto, H.; Matsuda, A. Front. Chem. 2014, 2, 104.
- (81) Qin, L.; He, L.; Zhao, J.; Zhao, B.; Yin, Y.; Yang, Y. Sens. Actuators, B 2017, 240, 779-784.
- (82) Tian, T.; Dong, J.; Xu, J. Microchim. Acta 2016, 183 (6), 1925–1932.
- (83) Trafela, Š.; Zavašnik, J.; Šturm, S.; Rožman, K. Ž. Electrochim. Acta 2019, 309, 346–353.
- (84) Wang, L.; Lu, W.; Zhu, W.; Wu, H.; Wang, F.; Xu, X. Sens. Actuators, B 2020, 304, 127330.
- (85) Muench, F.; Schaefer, S.; Hagelüken, L.; Molina-Luna, L.; Duerrschnabel, M.; Kleebe, H. J.; Brötz, J.; Vaskevich, A.; Rubinstein, I.; Ensinger, W. ACS Appl. Mater. Interfaces 2017, 9 (36), 31142–31152.
- (86) Lin, Z. T.; Li, Y.; Gu, J.; Wang, H.; Zhu, Z.; Hong, X.; Zhang, Z.; Lu, Q.; Qiu, J.; Wang, X.; et al. *Adv. Funct. Mater.* **2018**, 28 (31), 1802482.
- (87) Liu, L.; Xiang, G.; Jiang, D.; Du, C.; Liu, C.; Huang, W.; Pu, X. Microchim. Acta **2016**, 183 (1), 379–387.
- (88) Li, H. H.; Xie, M. L.; Cui, C. H.; He, D.; Gong, M.; Jiang, J.; Zheng, Y. R.; Chen, G.; Lei, Y.; Yu, S. H. *Chem. Mater.* **2016**, 28 (24), 8890–8898.
- (89) Huang, H.; Nie, R.; Song, Y.; Ji, Y.; Guo, R.; Liu, Z. Sens. Actuators, B **2016**, 230, 422–426.
- (90) Jajcevic, K.; Chami, M.; Sugihara, K. Small **2016**, 12 (35), 4830–4836.
- (91) Cho, H.-J.; Chen, V. T.; Qiao, S.; Koo, W.-T.; Penner, R. M.; Kim, I.-D. ACS Sensors **2018**, 3 (10), 2152–2158.
- (92) Prajapati, C. S.; Bhat, N. Sens. Actuators, B 2018, 260, 236-242.
- (93) Cho, M.; Zhu, J.; Kim, H.; Kang, K.; Park, I. ACS Appl. Mater. Interfaces 2019, 11 (14), 13343–13349.
- (94) Koo, W. T.; Qiao, S.; Ogata, A. F.; Jha, G.; Jang, J. S.; Chen, V. T.; Kim, I. D.; Penner, R. M. ACS Nano 2017, 11 (9), 9276–9285.
- (95) Yang, F.; Taggart, D. K.; Penner, R. M. Small 2010, 6 (13), 1422-1429.
- (96) Liu, W.; Xu, L.; Sheng, K.; Zhou, X.; Dong, B.; Lu, G.; Song, H. NPG Asia Mater. **2018**, 10 (4), 293–308.
- (97) Hwang, T. Y.; Go, G. M.; Park, S.; Lee, J.; Song, Y.; Kim, S.; Cho, H. B.; Choa, Y. H. ACS Appl. Mater. Interfaces **2019**, 11 (50), 47015–47024.
- (98) Gwak, R.; Kim, H.; Yoo, S. M.; Lee, S. Y.; Lee, G. J.; Lee, M. K.; Rhee, C. K.; Kang, T.; Kim, B. Sci. Rep. **2016**, 6, 19646.
- (99) Koh, E. H.; Mun, C.; Kim, C.; Park, S. G.; Choi, E. J.; Kim, S. H.; Dang, J.; Choo, J.; Oh, J. W.; Kim, D. H.; et al. ACS Appl. Mater. Interfaces 2018, 10 (12), 10388–10397.
- (100) Eom, G.; Kim, H.; Hwang, A.; Son, H.-Y. Y.; Choi, Y.; Moon, J.; Kim, D.; Lee, M.; Lim, E.-K. K.; Jeong, J.; et al. *Adv. Funct. Mater.* **2017**, *27* (37), 1701832.
- (101) Jibril, L.; Ramírez, J.; Zaretski, A. V.; Lipomi, D. J. Sens. Actuators, A 2017, 263, 702–706.
- (102) Zhang, S.; Liu, H.; Yang, S.; Shi, X.; Zhang, D.; Shan, C.; Mi, L.; Liu, C.; Shen, C.; Guo, Z. ACS Appl. Mater. Interfaces 2019, 11 (11), 10922–10932.
- (103) Ho, M. D.; Ling, Y.; Yap, L. W.; Wang, Y.; Dong, D.; Zhao, Y.; Cheng, W. Adv. Funct. Mater. 2017, 27 (25), 1700845.

- (104) Kim, S. R.; Kim, J. H.; Park, J. W. ACS Appl. Mater. Interfaces **2017**, 9 (31), 26407–26416.
- (105) Xie, F.; Cao, X.; Qu, F.; Asiri, A. M.; Sun, X. Sens. Actuators, B 2018, 255, 1254–1261.
- (106) Wang, J.; Yang, B.; Gao, F.; Song, P.; Li, L.; Zhang, Y.; Lu, C.; Goh, M. C.; Du, Y. Nanoscale Res. Lett. 2019, 14 (1), 11.
- (107) Gao, N.; Zhou, W.; Jiang, X.; Hong, G.; Fu, T. M.; Lieber, C. M. Nano Lett. 2015, 15 (3), 2143–2148.
- (108) Cao, A.; Zhu, W.; Shang, J.; Klootwijk, J. H.; Sudhölter, E. J. R.; Huskens, J.; De Smet, L. C. P. M. Nano Lett. 2017, 17 (1), 1–7. (109) Jin, Y.; Gao, A.; Jin, Q.; Li, T.; Wang, Y.; Zhao, J. Nanotechnology 2018, 29 (13), 135501.
- (110) Janissen, R.; Sahoo, P. K.; Santos, C. A.; Da Silva, A. M.; Von Zuben, A. A. G.; Souto, D. E. P.; Costa, A. D. T.; Celedon, P.; Zanchin, N. I. T.; Almeida, D. B.; et al. *Nano Lett.* **2017**, *17* (10), 5938–5949.
- (111) Lynall, D.; Tseng, A. C.; Nair, S. V.; Savelyev, I. G.; Blumin, M.; Wang, S.; Wang, Z. M.; Ruda, H. E. ACS Nano 2020, 14 (1), 964–973
- (112) Riedel, M.; Hölzel, S.; Hille, P.; Schörmann, J.; Eickhoff, M.; Lisdat, F. *Biosens. Bioelectron.* **2017**, *94*, 298–304.
- (113) Zhao, D.; Huang, H.; Chen, S.; Li, Z.; Li, S.; Wang, M.; Zhu, H.; Chen, X. Nano Lett. **2019**, 19 (6), 3448–3456.
- (114) Kan, H.; Li, M.; Luo, J.; Zhang, B.; Liu, J.; Hu, Z.; Zhang, G.; Jiang, S.; Liu, H. *IEEE Sens. J.* **2019**, *19* (3), 846–851.
- (115) Yen, L. C.; Pan, T. M.; Lee, C. H.; Chao, T. S. Sens. Actuators, B 2016, 230, 398-404.
- (116) Kutovyi, Y.; Hlukhova, H.; Boichuk, N.; Menger, M.; Offenhäusser, A.; Vitusevich, S. *Biosens. Bioelectron.* **2020**, *154*, 112053
- (117) Kim, D.; Park, C.; Choi, W.; Shin, S. H.; Jin, B.; Baek, R. H.; Lee, J. S. *IEEE Sens. J.* **2020**, 20 (5), 2270–2277.
- (118) Kutovyi, Y.; Li, J.; Zadorozhnyi, I.; Hlukhova, H.; Boichuk, N.; Yehorov, D.; Menger, M.; Vitusevich, S. MRS Adv. 2020, 5 (16), 835–846.
- (119) Zhou, K.; Zhao, Z.; Pan, L.; Wang, Z. Sens. Actuators, B 2019, 279, 111-121.
- (120) Rani, D.; Pachauri, V.; Madaboosi, N.; Jolly, P.; Vu, X. T.; Estrela, P.; Chu, V.; Conde, J. P.; Ingebrandt, S. *ACS Omega* **2018**, 3 (8), 8471–8482.
- (121) Maedler, C.; Kim, D.; Spanjaard, R. A.; Hong, M.; Erramilli, S.; Mohanty, P. ACS Sensors **2016**, *1* (6), 696–701.
- (122) Shalev, G.; Landman, G.; Amit, I.; Rosenwaks, Y.; Levy, I. NPG Asia Mater. 2013, 5 (3), e41.
- (123) Swaminathan, N.; Henning, A.; Vaknin, Y.; Shimanovich, K.; Godkin, A.; Shalev, G.; Rosenwaks, Y. ACS Sensors 2016, 1 (6), 688–605
- (124) Swaminathan, N.; Henning, A.; Jurca, T.; Hayon, J.; Shalev, G.; Rosenwaks, Y. Sens. Actuators, B **2017**, 248, 240–246.
- (125) Liu, Q.; Yang, T.; Ye, Y.; Chen, P.; Ren, X.; Rao, A.; Wan, Y.; Wang, B.; Luo, Z. *J. Mater. Chem. B* **2019**, *7* (9), 1442–1449.
- (126) Liu, D.; Lin, L.; Chen, Q.; Zhou, H.; Wu, J. ACS Sensors 2017, 2 (10), 1491–1497.
- (127) Ma, S.; Li, X.; Lee, Y. K.; Zhang, A. Biosens. Bioelectron. 2018, 117, 276–282.
- (128) Israelachvili, J. N. *Intermolecular and Surface Forces*; Elsevier: Amsterdam, 2011; https://books.google.com/books?hl=en&lr=&id=vgyBJbtNOcoC&oi=fnd&pg=PP1&ots=\_QNk6mB4U8&sig=1zapSOsR6YB5gi-Ztp6iyVP5duI#v=onepage&q&f=false (accessed 2020-09-16).
- (129) Gao, A.; Lu, N.; Wang, Y.; Li, T. Sci. Rep. 2016, 6 (1), 22554. (130) Tran, D. P.; Winter, M. A.; Wolfrum, B.; Stockmann, R.; Yang,
- C. T.; Pourhassan-Moghaddam, M.; Offenhaüsser, A.; Thierry, B. *ACS Nano* **2016**, *10* (2), 2357–2364.
- (131) Vacic, A.; Criscione, J. M.; Rajan, N. K.; Stern, E.; Fahmy, T. M.; Reed, M. A. J. Am. Chem. Soc. 2011, 133 (35), 13886–13889.
- (132) Liu, Y.; Rahimian, A.; Krylyuk, S.; Vu, T.; Crulhas, B.; Stybayeva, G.; Imanbekova, M.; Shin, D. S.; Davydov, A.; Revzin, A. ACS Sensors 2017, 2 (11), 1644–1652.

- (133) Lin, L.; Liu, D.; Chen, Q.; Zhou, H.; Wu, J. Nanoscale 2016, 8 (41), 17757–17764.
- (134) Krivitsky, V.; Zverzhinetsky, M.; Patolsky, F. Nano Lett. 2016, 16 (10), 6272-6281.
- (135) Krivitsky, V.; Zverzhinetsky, M.; Patolsky, F. ACS Nano 2020, 14, 3587.
- (136) Lee, M.; Palanisamy, S.; Zhou, B. H.; Wang, L. Y.; Chen, C. Y.; Lee, C. Y.; Yuan, S. S. F.; Wang, Y. M. ACS Appl. Mater. Interfaces **2018**, 10 (42), 36120–36127.
- (137) Mu, L.; Droujinine, I. A.; Lee, J.; Wipf, M.; Davis, P.; Adams, C.; Hannant, J.; Reed, M. A. Anal. Chem. **2017**, 89 (21), 11325–11331.
- (138) Wipf, M.; Stoop, R. L.; Navarra, G.; Rabbani, S.; Ernst, B.; Bedner, K.; Schönenberger, C.; Calame, M. ACS Sensors 2016, 1 (6), 781–788
- (139) Li, J.; Kutovyi, Y.; Zadorozhnyi, I.; Boichuk, N.; Vitusevich, S. Adv. Mater. Interfaces 2020, 7 (15), 2000508.
- (140) Kim, K.; Park, C.; Kwon, D.; Kim, D.; Meyyappan, M.; Jeon, S.; Lee, J. S. *Biosens. Bioelectron.* **2016**, *77*, 695–701.
- (141) Vu, C. A.; Hu, W. P.; Yang, Y. S.; Chan, H. W. H.; Chen, W. Y. ACS Omega 2019, 4 (12), 14765–14771.
- (142) Schütt, J.; Ibarlucea, B.; Illing, R.; Zörgiebel, F.; Pregl, S.; Nozaki, D.; Weber, W. M.; Mikolajick, T.; Baraban, L.; Cuniberti, G. *Nano Lett.* **2016**, *16* (8), 4991–5000.
- (143) Shehada, N.; Cancilla, J. C.; Torrecilla, J. S.; Pariente, E. S.; Brönstrup, G.; Christiansen, S.; Johnson, D. W.; Leja, M.; Davies, M. P. A.; Liran, O.; et al. *ACS Nano* **2016**, *10* (7), 7047–7057.
- (144) Kwon, J.; Lee, B. H.; Kim, S. Y.; Park, J. Y.; Bae, H.; Choi, Y. K.; Ahn, J. H. ACS Sensors **2019**, *4* (6), 1724–1729.
- (145) Chen, X.; Hu, Q.; Chen, S.; Netzer, N. L.; Wang, Z.; Zhang, S. L.; Zhang, Z. Sens. Actuators, B 2018, 270, 89–96.
- (146) Anand, A.; Liu, C. R.; Chou, A. C.; Hsu, W. H.; Ulaganathan, R. K.; Lin, Y. C.; Dai, C. A.; Tseng, F. G.; Pan, C. Y.; Chen, Y. T. ACS Sensors **2017**, 2 (1), 69–79.
- (147) Ren, Y.; Zou, Y.; Liu, Y.; Zhou, X.; Ma, J.; Zhao, D.; Wei, G.; Ai, Y.; Xi, S.; Deng, Y. Nat. Mater. **2020**, 19 (2), 203–211.
- (148) Yao, M. S.; Tang, W. X.; Wang, G. E.; Nath, B.; Xu, G. Adv. Mater. 2016, 28 (26), 5229–5234.
- (149) Drobek, M.; Kim, J. H.; Bechelany, M.; Vallicari, C.; Julbe, A.; Kim, S. S. ACS Appl. Mater. Interfaces 2016, 8 (13), 8323–8328.
- (150) Song, Z.; Wei, Z.; Wang, B.; Luo, Z.; Xu, S.; Zhang, W.; Yu, H.; Li, M.; Huang, Z.; Zang, J.; et al. *Chem. Mater.* **2016**, 28 (4), 1205–1212.
- (151) Meng, S.; Hong, Y.; Dai, Z.; Huang, W.; Dong, X. ACS Appl. Mater. Interfaces 2017, 9 (14), 12453–12460.
- (152) Chen, L.; Cui, J.; Sheng, X.; Xie, T.; Xu, T.; Feng, X. ACS Sensors 2017, 2 (11), 1567–1572.
- (153) Cho, I.; Sim, Y. C.; Cho, M.; Cho, Y. H.; Park, I. ACS Sensors **2020**, 5 (2), 563–570.
- (154) Wang, Y.; Zhou, Y.; Ren, H.; Wang, Y.; Zhu, X.; Guo, Y.; Li, X. Anal. Chem. **2020**, 92 (16), 11007–11017.
- (155) Yuan, K.; Wang, C. Y.; Zhu, L. Y.; Cao, Q.; Yang, J. H.; Li, X. X.; Huang, W.; Wang, Y. Y.; Lu, H. L.; Zhang, D. W. ACS Appl. Mater. Interfaces 2020, 12 (12), 14095–14104.
- (156) Sinha, L.; Pakhira, S.; Bhojane, P.; Mali, S.; Hong, C. K.; Shirage, P. M. ACS Sustainable Chem. Eng. 2018, 6 (10), 13248–13261
- (157) Long, H.; Harley-Trochimczyk, A.; Cheng, S.; Hu, H.; Chi, W. S.; Rao, A.; Carraro, C.; Shi, T.; Tang, Z.; Maboudian, R. ACS Appl. Mater. Interfaces 2016, 8 (46), 31764–31771.
- (158) Kim, S. J.; Choi, S. J.; Jang, J. S.; Cho, H. J.; Koo, W. T.; Tuller, H. L.; Kim, I. D. *Adv. Mater.* **2017**, *29* (36), 1700737.
- (159) Choi, S. J.; Chattopadhyay, S.; Kim, J. J.; Kim, S. J.; Tuller, H. L.; Rutledge, G. C.; Kim, I. D. *Nanoscale* **2016**, 8 (17), 9159–9166. (160) Jeong, Y. J.; Koo, W. T.; Jang, J. S.; Kim, D. H.; Kim, M. H.; Kim, I. D. *ACS Appl. Mater. Interfaces* **2018**, 10 (2), 2016–2025.
- (161) Katwal, G.; Paulose, M.; Rusakova, I. A.; Martinez, J. E.; Varghese, O. K. Nano Lett. **2016**, 16 (5), 3014–3021.

- (162) Wang, J.; Xu, L.; Lu, Y.; Sheng, K.; Liu, W.; Chen, C.; Li, Y.; Dong, B.; Song, H. *Anal. Chem.* **2016**, 88 (24), 12346–12353.
- (163) Steinhauer, S.; Chapelle, A.; Menini, P.; Sowwan, M. ACS Sensors 2016, 1 (5), 503-507.
- (164) Song, L.; Dou, K.; Wang, R.; Leng, P.; Luo, L.; Xi, Y.; Kaun, C. C.; Han, N.; Wang, F.; Chen, Y. ACS Appl. Mater. Interfaces 2020, 12 (1), 1270–1279.
- (165) Jun, L.; Chen, Q.; Fu, W.; Yang, Y.; Zhu, W.; Zhang, J. ACS Appl. Mater. Interfaces 2020, 12 (34), 38425-38434.
- (166) Ali, M. A.; Mondal, K.; Jiao, Y.; Oren, S.; Xu, Z.; Sharma, A.; Dong, L. ACS Appl. Mater. Interfaces 2016, 8 (32), 20570–20582.
- (167) Bulemo, P. M.; Cho, H. J.; Kim, N. H.; Kim, I. D. ACS Appl. Mater. Interfaces 2017, 9 (31), 26304–26313.
- (168) Shankar, P.; Rayappan, J. B. B. ACS Appl. Mater. Interfaces 2017, 9 (43), 38135–38145.
- (169) Choi, S. J.; Ku, K. H.; Kim, B. J.; Kim, I. D. ACS Sensors 2016, 1 (9), 1124–1131.
- (170) Hung, P. T.; Hoat, P. D.; Hien, V. X.; Lee, H. Y.; Lee, S.; Lee, J. H.; Kim, J. J.; Heo, Y. W. ACS Appl. Mater. Interfaces **2020**, 12 (30), 34274–34282.
- (171) Van Dang, T.; Duc Hoa, N.; Van Duy, N.; Van Hieu, N. ACS Appl. Mater. Interfaces 2016, 8 (7), 4828–4837.
- (172) Zhou, X.; Wang, A.; Wang, Y.; Bian, L.; Yang, Z.; Bian, Y.; Gong, Y.; Wu, X.; Han, N.; Chen, Y. ACS Sensors **2018**, 3 (11), 2385–2393.
- (173) Kwon, Y. J.; Kang, S. Y.; Wu, P.; Peng, Y.; Kim, S. S.; Kim, H. W. ACS Appl. Mater. Interfaces **2016**, 8 (21), 13646–13658.
- (174) Kim, J. H.; Mirzaei, A.; Kim, H. W.; Kim, S. S. ACS Appl. Mater. Interfaces **2019**, 11 (27), 24172-24183.
- (175) Cao, X.; Cao, X.; Guo, H.; Li, T.; Jie, Y.; Wang, N.; Wang, Z. L. ACS Nano **2016**, 10 (8), 8038–8044.
- (176) Han, L.; Shao, C.; Liang, B.; Liu, A. ACS Appl. Mater. Interfaces 2016, 8 (22), 13768–13776.
- (177) Du, X.; Li, Y.; Motley, J. R.; Stickle, W. F.; Herman, G. S. ACS Appl. Mater. Interfaces **2016**, 8 (12), 7631–7637.
- (178) Meng, G.; Zhuge, F.; Nagashima, K.; Nakao, A.; Kanai, M.; He, Y.; Boudot, M.; Takahashi, T.; Uchida, K.; Yanagida, T. *ACS Sensors* **2016**, *1* (8), 997–1002.
- (179) Zeng, H.; Takahashi, T.; Kanai, M.; Zhang, G.; He, Y.; Nagashima, K.; Yanagida, T. ACS Sensors 2017, 2 (12), 1854–1859. (180) Suh, J. M.; Sohn, W.; Shim, Y. S.; Choi, J. S.; Song, Y. G.; Kim, T. L.; Jeon, J. M.; Kwon, K. C.; Choi, K. S.; Kang, C. Y.; et al. ACS Appl. Mater. Interfaces 2018, 10 (1), 1050–1058.
- (181) Cho, S. Y.; Yoo, H. W.; Kim, J. Y.; Jung Bin, W.; Jin, M. L.; Kim, J. S.; Jeon, H. J.; Jung, H. T. *Nano Lett.* **2016**, *16* (7), 4508–4515
- (182) Zappa, D.; Galstyan, V.; Kaur, N.; Munasinghe Arachchige, H. M. M.; Sisman, O.; Comini, E. Anal. Chim. Acta 2018, 1039, 1–23.
- (183) Ahmad, R.; Majhi, S. M.; Zhang, X.; Swager, T. M.; Salama, K. N. Adv. Colloid Interface Sci. 2019, 270, 1-27.
- (184) Yuan, K.; Wang, C.-Y.; Zhu, L.-Y.; Cao, Q.; Yang, J.-H.; Li, X.-X.; Huang, W.; Wang, Y.-Y.; Lu, H.-L.; Zhang, D. W. ACS Appl. Mater. Interfaces 2020, 12 (12), 14095–14104.
- (185) Cho, S.-Y.; Jang, D.; Kang, H.; Koh, H.-J.; Choi, J.; Jung, H.-T. Anal. Chem. **2019**, 91 (10), 6850–6858.
- (186) Choi, M. S.; Bang, J. H.; Mirzaei, A.; Na, H. G.; Jin, C.; Oum, W.; Kim, S. S.; Kim, H. W. Appl. Surf. Sci. 2019, 484, 1102–1110.
- (187) Raza, M. H.; Kaur, N.; Comini, E.; Pinna, N. ACS Appl. Mater. Interfaces 2020, 12 (4), 4594–4606.
- (188) Choi, Y. M.; Cho, S.; Jang, D.; Koh, H.; Choi, J.; Kim, C.; Jung, H. Adv. Funct. Mater. 2019, 29 (9), 1808319.
- (189) Choi, S.-J.; Ku, K. H.; Kim, B. J.; Kim, I.-D. ACS Sensors 2016, 1 (9), 1124–1131.
- (190) Kim, J.-H.; Lee, J.-H.; Park, Y.; Kim, J.-Y.; Mirzaei, A.; Kim, H. W.; Kim, S. S. Sens. Actuators, B **2019**, 294, 78–88.
- (191) Wang, L.; Li, J.; Wang, Y.; Yu, K.; Tang, X.; Zhang, Y.; Wang, S.; Wei, C. Sci. Rep. **2016**, *6*, 35079.
- (192) Qu, F.; Zhang, S.; Zhang, B.; Zhou, X.; Du, S.; Lin, C.-T.; Ruan, S.; Yang, M. Microchim. Acta 2019, 186 (4), 222.

- (193) Li, F.; Zhang, T.; Gao, X.; Wang, R.; Li, B. Sens. Actuators, B **2017**, 252, 822–830.
- (194) Suh, J. M.; Sohn, W.; Shim, Y.-S.; Choi, J.-S.; Song, Y. G.; Kim, T. L.; Jeon, J.-M.; Kwon, K. C.; Choi, K. S.; Kang, C.-Y.; et al. ACS Appl. Mater. Interfaces 2018, 10 (1), 1050–1058.
- (195) Hung, P. T.; Hoat, P. D.; Hien, V. X.; Lee, H.-Y.; Lee, S.; Lee, J.-H.; Kim, J.-J.; Heo, Y.-W. ACS Appl. Mater. Interfaces **2020**, 12 (30), 34274–34282.
- (196) Diao, K.; Xiao, J.; Zheng, Z.; Cui, X. Appl. Surf. Sci. 2018, 459, 630–638.
- (197) Mani, V.; Selvaraj, S.; Peng, T.-K.; Lin, H.-Y.; Jeromiyas, N.; Ikeda, H.; Hayakawa, Y.; Ponnusamy, S.; Muthamizhchelvan, C.; Huang, S.-T. ACS Appl. Nano Mater. 2019, 2 (8), 5049–5060.
- (198) Le, H. T.; Tran, D. T.; Doan, T. L. L.; Kim, N. H.; Lee, J. H. Biosens. Bioelectron. **2019**, 139, 111327.
- (199) He, Q.; Liu, J.; Liu, X.; Li, G.; Chen, D.; Deng, P.; Liang, J. Electrochim. Acta 2019, 296, 683–692.
- (200) Wang, J.; Xu, L.; Lu, Y.; Sheng, K.; Liu, W.; Chen, C.; Li, Y.; Dong, B.; Song, H. *Anal. Chem.* **2016**, *88* (24), 12346–12353.
- (201) Xu, J.; Xu, N.; Zhang, X.; Xu, P.; Gao, B.; Peng, X.; Mooni, S.; Li, Y.; Fu, J.; Huo, K. Sens. Actuators, B 2017, 244, 38–46.
- (202) You, Q.; Liu, T.; Pang, J.; Jiang, D.; Chu, Z.; Jin, W. Sens. Actuators, B 2019, 296, 126617.
- (203) Mani, V.; Selvaraj, S.; Peng, T. K.; Lin, H. Y.; Jeromiyas, N.; Ikeda, H.; Hayakawa, Y.; Ponnusamy, S.; Muthamizhchelvan, C.; Huang, S. T. ACS Appl. Nano Mater. 2019, 2 (8), 5049–5060.
- (204) Danielson, E.; Dhamodharan, V.; Porkovich, A.; Kumar, P.; Jian, N.; Ziadi, Z.; Grammatikopoulos, P.; Sontakke, V. A.; Yokobayashi, Y.; Sowwan, M. Sci. Rep. 2019, 9 (1), 1–10.
- (205) Paul, K. B.; Singh, V.; Vanjari, S. R. K.; Singh, S. G. Biosens. Bioelectron. 2017, 88, 144-152.
- (206) Li, Y.-Y.; Kang, P.; Wang, S.-Q.; Liu, Z.-G.; Li, Y.-X.; Guo, Z. Sens. Actuators, B **2021**, 327, 128878.
- (207) Pham, T. T., Tran, D. P.; Thierry, B. Nanoscale Adv. 2019, 1 (12), 4870–4877.
- (208) Meng, Y.; Liu, G.; Liu, A.; Guo, Z.; Sun, W.; Shan, F. ACS Appl. Mater. Interfaces 2017, 9 (12), 10805–10812.
- (209) Zhao, C.; Xu, X.; Bae, S.-H.; Yang, Q.; Liu, W.; Belling, J. N.; Cheung, K. M.; Rim, Y. S.; Yang, Y.; Andrews, A. M.; et al. *Nano Lett.* **2018**, *18* (9), 5590–5595.
- (210) Liu, Q.; Aroonyadet, N.; Song, Y.; Wang, X.; Cao, X.; Liu, Y.; Cong, S.; Wu, F.; Thompson, M. E.; Zhou, C. ACS Nano 2016, 10 (11), 10117–10125.
- (211) Liu, Q.; Liu, Y.; Wu, F.; Cao, X.; Li, Z.; Alharbi, M.; Abbas, A. N.; Amer, M. R.; Zhou, C. ACS Nano 2018, 12 (2), 1170–1178.
- (212) Nakatsuka, N.; Yang, K. A.; Abendroth, J. M.; Cheung, K. M.; Xu, X.; Yang, H.; Zhao, C.; Zhu, B.; Rim, Y. S.; Yang, Y.; et al. *Science (Washington, DC, U. S.)* **2018**, 362 (6412), 319–324.
- (213) Veeralingam, S.; Badhulika, S. Sens. Actuators, B 2020, 321, 128540.
- (214) Cho, S.-Y.; Yoo, H.-W.; Kim, J. Y.; Jung, W.-B.; Jin, M. L.; Kim, J.-S.; Jeon, H.-J.; Jung, H.-T. *Nano Lett.* **2016**, *16* (7), 4508–4515.
- (215) Kim, K.-H.; Kim, S.-J.; Cho, H.-J.; Kim, N.-H.; Jang, J.-S.; Choi, S.-J.; Kim, I.-D. Sens. Actuators, B **2017**, 241, 1276–1282.
- (216) Li, F.; Gao, X.; Wang, R.; Zhang, T.; Lu, G.; Barsan, N. ACS Appl. Mater. Interfaces 2016, 8 (30), 19799–19806.
- (217) Li, Q.; Liu, D.; Xu, L.; Xing, R.; Liu, W.; Sheng, K.; Song, H. ACS Appl. Mater. Interfaces 2015, 7 (40), 22719–22726.
- (218) Sies, H. Redox Biol. 2017, 11, 613-619.
- (219) Kim, S.; Cho, Y. K.; Lee, C.; Kim, M. H.; Lee, Y. Biosens. Bioelectron. **2016**, 77, 1144–1152.
- (220) Ahn, M.-S.; Ahmad, R.; Yoo, J.-Y.; Hahn, Y.-B. J. Colloid Interface Sci. 2018, 516, 364–370.
- (221) Liu, Q.; Zhao, C.; Chen, M.; Liu, Y.; Zhao, Z.; Wu, F.; Li, Z.; Weiss, P. S.; Andrews, A. M.; Zhou, C. *iScience* **2020**, 23 (9), 101469. (222) Shirakawa, H.; Louis, E. J.; MacDiarmid, A. G.; Chiang, C. K.; Heeger, A. J. *J. Chem. Soc., Chem. Commun.* **1977**, No. 16, 578–580.

- (223) Cui, C.; Park, D. H.; Choi, H.; Joo, J.; Ahn, D. J. Small 2016, 12 (9), 1154–1158.
- (224) Hien, H. T.; Giang, H. T.; Hieu Van, N.; Trung, T.; Tuan Van, C. Sens. Actuators, B 2017, 249, 348-356.
- (225) Xia, Y.; Whitesides, G. M. Angew. Chem., Int. Ed. 1998, 37 (5), 550–575.
- (226) Jiang, Y.; Tang, N.; Zhou, C.; Han, Z.; Qu, H.; Duan, X. Nanoscale 2018, 10 (44), 20578–20586.
- (227) Tang, N.; Zhou, C.; Xu, L.; Jiang, Y.; Qu, H.; Duan, X. ACS Sensors 2019, 4 (3), 726–732.
- (228) Hwang, J. K.; Cho, S.; Dang, J. M.; Kwak, E. B.; Song, K.; Moon, J.; Sung, M. M. Nat. Nanotechnol. 2010, 5 (10), 742-748.
- (229) Cho, B.; Park, K. S.; Baek, J.; Oh, H. S.; Koo Lee, Y.-E.; Sung, M. M. Nano Lett. **2014**, 14 (6), 3321–3327.
- (230) Mun, S.; Park, Y.; Lee, Y. E. K.; Sung, M. M. Langmuir 2017, 33 (47), 13554–13560.
- (231) Lim, J.-H.; Mirkin, C. A. Adv. Mater. 2002, 14 (20), 1474–1477.
- (232) Zhang, P.; Aydemir, N.; Alkaisi, M.; Williams, D. E.; Travas-Sejdic, J. ACS Appl. Mater. Interfaces 2018, 10 (14), 11888-11895.
- (233) Zips, S.; Grob, L.; Rinklin, P.; Terkan, K.; Adly, N. Y.; Weiß, L. J. K.; Mayer, D.; Wolfrum, B. ACS Appl. Mater. Interfaces 2019, 11 (36), 32778-32786.
- (234) Wajahat, M.; Lee, S.; Kim, J. H.; Chang, W. S.; Pyo, J.; Cho, S. H.; Seol, S. K. ACS Appl. Mater. Interfaces **2018**, 10 (23), 19999–20005.
- (235) Zhang, S.; Kumar, P.; Nouas, A. S.; Fontaine, L.; Tang, H.; Cicoira, F. *APL Mater.* **2015**, *3* (1), 014911.
- (236) Khodagholy, D.; Rivnay, J.; Sessolo, M.; Gurfinkel, M.; Leleux, P.; Jimison, L. H.; Stavrinidou, E.; Herve, T.; Sanaur, S.; Owens, R. M.; et al. *Nat. Commun.* **2013**, *4*, 2133.
- (237) Tang, N.; Jiang, Y.; Qu, H.; Duan, X. Nanotechnology 2017, 28 (48), 485301.
- (238) Ma, Z.; Chen, P.; Cheng, W.; Yan, K.; Pan, L.; Shi, Y.; Yu, G. Nano Lett. 2018, 18 (7), 4570-4575.
- (239) Qin, Y.; Cui, Z.; Zhang, T.; Liu, D. Sens. Actuators, B 2018, 258 (2), 246-254.
- (240) Park, S. J.; Lee, J.; Seo, S. E.; Kim, K. H.; Park, C. S.; Lee, S. H.; Ban, H. S.; Lee, B. D.; Song, H. S.; Kim, J.; et al. *Sci. Rep.* **2020**, *10* (1), 3772.
- (241) Wang, J. Analytical Electrochemistry, 3rd ed.; John Wiley & Sons, Inc, 2006.
- (242) Hui, N.; Sun, X.; Niu, S.; Luo, X. ACS Appl. Mater. Interfaces 2017, 9 (3), 2914–2923.
- (243) Teng, Y.; Liu, F.; Kan, X. Microchim. Acta 2017, 184 (8), 2515-2522.
- (244) Kwon, O. S.; Park, C. S.; Park, S. J.; Noh, S.; Kim, S.; Kong, H. J.; Bae, J.; Lee, C. S.; Yoon, H. Sci. Rep. **2016**, 6 (September), 33724.
- (245) He, M.; Croy, R. G.; Essigmann, J. M.; Swager, T. M. ACS Sensors 2019, 4 (10), 2819–2824.
- (246) Falco, A.; Loghin, F. C.; Becherer, M.; Lugli, P.; Salmerón, J. F.; Rivadeneyra, A. ACS Sensors 2019, 4 (12), 3141–3146.
- (247) Zhu, Q.; Huang, J.; Yan, M.; Ye, J.; Wang, D.; Lu, Q.; Yang, X. *Nanoscale* **2018**, *10* (31), 14847–14851.
- (248) Xie, L.; Asiri, A. M.; Sun, X. Sens. Actuators, B 2017, 244, 11-
- (249) Kim, J.; Kim, M.; Lee, M. S.; Kim, K.; Ji, S.; Kim, Y. T.; Park, J.; Na, K.; Bae, K. H.; Kim, H. K.; et al. *Nat. Commun.* **2017**, 8 (1), 14997
- (250) Ramachandran, K.; Raj Kumar, T.; Babu, K. J.; Gnana Kumar, G. Sci. Rep. **2016**, 6 (1), 36583.
- (251) Muratova, I. S.; Mikhelson, K. N.; Ermolenko, Y. E.; Offenhäusser, A.; Mourzina, Y. Sens. Actuators, B 2016, 232, 420–427.
- (252) Chuang, C. S.; Wu, C. Y.; Juan, P. H.; Hou, N. C.; Fan, Y. J.; Wei, P. K.; Sheen, H. I. *Analyst* **2020**, *145* (1), 52–60.
- (253) Yu, Y.; Zhu, Q. Y.; Xiang, F.; Hu, Y.; Zhang, L.; Xu, X.; Liu, N.; Huang, S. Carbon 2020, 157, 40–46.
- (254) Yang, D.; Cho, I.; Kim, D.; Lim, M. A.; Li, Z.; Ok, J. G.; Lee, M.; Park, I. ACS Appl. Mater. Interfaces 2019, 11 (27), 24298–24307.

- (255) Zhang, W.; Hu, M.; Liu, X.; Wei, Y.; Li, N.; Qin, Y. J. Alloys Compd. **2016**, 679, 391–399.
- (256) Yang, X.; Zhang, S.; Zhao, L.; Sun, P.; Wang, T.; Liu, F.; Yan, X.; Gao, Y.; Liang, X.; Zhang, S.; et al. Sens. Actuators, B 2019, 281, 415–423.
- (257) Jung, D.-U.-J.; Ahmad, R.; Hahn, Y.-B. J. Colloid Interface Sci. **2018**, 512, 21–28.
- (258) Ahmad, R.; Ahn, M.-S.; Hahn, Y.-B. J. Colloid Interface Sci. 2017, 498, 292–297.
- (259) Zhu, J.; Huo, X.; Liu, X.; Ju, H. ACS Appl. Mater. Interfaces **2016**, 8 (1), 341-349.
- (260) Hwang, B. Y.; Du, W. X.; Lee, H. J.; Kang, S.; Takada, M.; Kim, J. Y. Nanomaterials **2020**, 10 (4), 696.
- (261) Xue, Q.; Wang, Q.; Han, Z.; Tang, N.; Zhou, C.; Pan, W.; Wang, Y.; Duan, X. Adv. Mater. Interfaces 2019, 6 (18), 1900671.